

Numerical simulations of delamination in fibre reinforced plastic shell structures using XFEM

Von der Fakultät für Maschinenbau
der Gottfried Wilhelm Leibniz Universität Hannover

zur Erlangung des akademischen Grades
Doktor-Ingenieur

genehmigte Dissertation
von

M.Sc. Saleh Yazdani

geboren am 21.03.1987 in Bojnord, Iran

2016

Herausgeber:

Prof. Dr.-Ing. habil. Dr. h.c. mult. Dr.-Ing. E.h. Peter Wriggers

Verwaltung:

Institut für Kontinuumsmechanik
Gottfried Wilhelm Leibniz Universität Hannover
Appelstraße 11
30167 Hannover

Tel: +49 511 762 3220

Fax: +49 511 762 5496

Web: www.ikm.uni-hannover.de

Kontakt zum Autor:

E-Mail: yazdani.saleh@yahoo.com

© M.Sc. Saleh Yazdani

Institut für Kontinuumsmechanik
Gottfried Wilhelm Leibniz Universität Hannover
Appelstraße 11
30167 Hannover

Alle Rechte, insbesondere das der Übersetzung in fremde Sprachen, vorbehalten. Ohne Genehmigung des Autors ist es nicht gestattet, dieses Heft ganz oder teilweise auf photomechanischem, elektronischem oder sonstigem Wege zu vervielfältigen.

ISBN 978-3-941302-19-8

1. Referent: Prof. Dr.-Ing. habil. Dr. h.c. mult. Dr.-Ing. E.h. Peter Wriggers

2. Referent: Prof. Xiaoying Zhuang, PhD

3. Referent: Prof. Dr.-Ing. Wilhelm Rust

Tag der Promotion: 13.12.2016

To my wife Mahsa

Zusammenfassung

Ein faserverstärkter Kunststoff (FVK) ist ein Werkstoff, bestehend aus Verstärkungsfasern und einer Kunststoffmatrix. Simulationen der fortschreitenden Delamination in Bauteilen aus faserverstärkten Kunststoffen mit der Standard Finite Elemente Methode sind sehr rechenaufwändig. Die Herausforderungen liegen hauptsächlich in der Festlegung des diskontinuierlichen Verschiebungsfelds (in Dickenrichtung der Laminate), Vorhersage des Bereichs der Delamination und Verfolgen der Ausbreitungsrichtung der Delamination. Unter dem Gesichtspunkt der computergestützten Berechnung führt einerseits der nichtlineare Prozess der Bruchmechanik als auch andererseits die geometrisch nichtlineare Antwort von Schalenstrukturen zu einem vollständig nichtlinearen Gleichungssystem. Durch die gekrümmte Form von Schalenstrukturen nimmt die Komplexität der Delamination zusätzlich zu. Die Formulierung, die der Berechnung der Delamination in Schalentragswerken zu Grunde gelegt wird, sollte daher entsprechend effizient sein, um die erwähnten Schwierigkeiten abzudecken. Bekannte Standardmodelle für diese Simulationen weisen Grenzen auf und sind teilweise erheblich aufwändiger. Weiterhin wird durch die Anwendung von Kohäsivzonenmodellen an allen Zwischenschichten, die die Schädigungs- und Bruchmechanik vereint, der rechnerische Aufwand enorm angehoben, da alle Zwischenschichten als diskontinuierlich definiert werden müssen.

In dieser Dissertation wird ein effizienter numerischer Algorithmus vorgestellt, um die Delamination in mehrfach schichtweise angeordneten Faserverbund-Schalenstrukturen zu untersuchen. Das Hauptaugenmerk liegt in der praktischen Anwendbarkeit des Algorithmus und der Reduktion des numerischen Rechenaufwandes. In dieser Arbeit wird basierend auf der erweiterten Finite-Elemente-Methode (XFEM) ein „mixed-mode“ Kohäsivzonenmodell, eine entsprechende Kontaktformulierung und ebenfalls ein Schädigungskriterium in einem gemeinsamen Algorithmus zusammengeführt, um die Delamination in Zwischenschichten zu untersuchen. Die entwickelte Schalenformulierung für den geometrisch nichtlinearen Anwendungsbereich dient zur Untersuchung des Antwortverhaltens von Schalen im Bereich kleiner Verzerrungen und moderater Rotationen. Um die schichtweise angeordneten Lamine zu simulieren wird die „Equivalent Single Layer Theory“ (ESLT) angewendet. Diese Formulierung wird sowohl mit der XFEM erweitert, um diskontinuierliche Gebiete abbilden zu können, als auch mit einer „mixed-mode“ bilinearen Kohäsivformulierung, um den Rissfortschritt zu verfolgen. Zwei Kohäsivzonen-Formulierungen, die sowohl auf einem linearen als auch auf einem exponentiellen Entwicklungsgesetz für den Schädigungsparameter basieren, werden formuliert und vorgestellt. Im Gegensatz zu bereits bestehenden Finite-Elemente-Modellen wird die Notwendigkeit der Einbeziehung des Kohäsivzonenmodells an allen verfügbaren Zwischenschichten vernachlässigt vermieden. Es werden zwei Ansätze zur Vorhersage der Verteilung der interlaminaren Spannungen entwickelt, die in der Platten- und Schalentheorie nicht berücksichtigt werden. Die Spannungen werden während des „post-processing“ berechnet und daraufhin als Anfangskriterium der Delamination verwendet. Sobald das Kriterium in einer bestimmten Schicht oder einem bestimmten Bereich erfüllt ist, wird die Formulierung des dazugehörigen Elements lokal geändert, damit eine Berechnung mittels XFEM und kohäsivem Schädi-

gungsverhalten durchgeführt werden kann. Folglich wird die Möglichkeit bereitgestellt, das Wachstum der Delamination lokal zu verfolgen; und somit wird der Rechenaufwand erheblich reduziert.

Die Leistungsfähigkeit der entwickelten Methoden werden mit Literaturergebnissen aus Simulation und Versuch verglichen. Die prognostizierten Ergebnisse zeigen, dass diese sehr gut mit denen aus Experimenten und numerischen Beispielen aus der Literatur übereinstimmen.

Schlagworte: Delamination, Schale, erweiterte Finite-Elemente-Methode (XFEM), Kohäsivzonenmodell, Beulen

Abstract

Fibre Reinforced Plastic (FRP) is a composite material made of a polymer matrix reinforced with fibres. The simulation of delamination type failure in multi-layered FRP shells with the standard finite element method is numerically expensive. The challenges mainly lie on the definition of the discontinuous field through-the-thickness of laminate, predicting the location of delamination onset, and tracking the delamination propagation. From the computational point of view the non-linear fracture process in one side and the geometrically non-linear response of the shell structures on the other side lead to a fully non-linear system of equations. In addition, the curved shape of the delamination in shell structures is complex. Therefore, the formulation that is applied to simulate the delamination in shells should be efficient enough to cover the mentioned difficulties. The standard models for such simulations have limits in their application and lead to enormous computational effort. Furthermore, the cohesive zone model that combines the damage and fracture mechanics is inserted at all the available interfaces. This increases the computational cost because for which each ply should be simulated independently.

In this work an efficient numerical tool is proposed to investigate delamination type failure in multi-layered composite shells. The focus is on the practicality of the algorithm and the reduction of computational cost. In the current contribution the eXtended Finite Element Method (XFEM), the mixed-mode cohesive zone model, the contact formulation, and the damage criterion are incorporated into a new algorithm to study the interfacial delamination. A flat-shell formulation is developed in the geometrically non-linear regime to study the response of shells in small strains and moderate rotations. In order to simulate the multi-layered laminates, the Equivalent Single Layer Theory (ESLT) is applied. This formulation is enhanced through the XFEM topology to be able to model discontinuous domains and a mixed-mode cohesive formulation is applied to track the delamination growth. Two cohesive zone models that are based on the bilinear and linear-exponential traction-separation law are formulated to track the delamination growth. In this thesis, the simulation can be initiated in an intact laminate. Thus, unlike formulations in existing finite element models there is no necessity of incorporating the cohesive zone model at all available interfaces. Two approaches are developed to calculate the interlaminar stresses which are missed in plate and shell theories. The interlaminar stresses are calculated during post-processing and they are being used in the delamination onset criterion. As soon as the criterion is satisfied at a specific layer and location, the formulation of that corresponding element is locally changed to XFEM and the cohesive behaviour. Consequently, the possibility to track delamination growth is locally provided; and hence, the computational cost is reduced.

The accuracy of the proposed method is demonstrated by comparing the results of each theory developed with the ones available in literature. The predicted results are shown to correlate very well with both experimental and numerical examples in literature.

Keywords: Delamination, Shell, XFEM, Cohesive zone model, Buckling

Acknowledgements

This dissertation is the summary of my researches at the Institute of Continuum Mechanics (IKM), Leibniz Universität Hannover. This project was supported within the MARIO (Multifunctional Active and Reactive Interfaces and Surfaces) doctoral program.

I would like to sincerely thank my principle supervisor, Professor Wilhelm Rust, for introducing me into the field of non-linear finite element method, for friendship meetings and his patient and professional guidance to me throughout my doctoral program. He always takes the time to answer all of my questions, and discuss possible solutions and methodologies. In addition, I would like to express my deep sense of gratitude to my second supervisor, Professor Peter Wriggers, for his support and helpful suggestions and motivations to pursue this project during my research at his institute. His answers to my scientific questions were right to the point and shed light on the dark parts of my scientific understandings. I am grateful to his support to participate scientific conferences and summer schools.

I would like to thank the chairman of the MARIO doctoral program, Professor Udo Nackenhorst, for his wise guidance and helpful comments during this program.

I also want to thank Dr. Xiaoying Zhuang for being a referee of this thesis.

I want to thank my colleagues at the Institute of Continuum Mechanics (IKM) as well as the members of MARIO doctoral program for scientific discussions and workshops we spent together.

Finally, and most important, I am grateful to my wife, Mahsa, for her endless patience and continuous encouragement and support. I dedicate this thesis to her.

Hanover, December 2016

Saleh Yazdani

Contents

1	Introduction	1
1.1	Motivation	1
1.2	State of the art	3
1.3	Outline of the thesis	6
2	A non-linear composite shell element	7
2.1	Theory of flat-shell	7
2.2	Kinematics of shell	9
2.2.1	Displacement field	10
2.2.2	Strain field	10
2.3	Constitutive equation	12
2.4	Shear correction factor	15
2.5	Assumed transverse shear strain field	16
2.6	Equilibrium equation	18
2.7	Tangent stiffness matrix derivation	20
2.8	Transformation to the global coordinate system	22
2.9	Technique for avoiding singularity	26
2.10	Warping function for flat-shell	27
2.11	Numerical tests	29
2.12	Closing remarks	33
3	Extension of the shell element for delamination analysis	35
3.1	Introduction	35
3.2	Kinematics of shell in XFEM topology	37
3.2.1	Displacement field	38
3.2.2	Strain field	39
3.3	Constitutive equation	42
3.4	Equilibrium equation	42
3.5	Tangent stiffness matrix derivation	43
3.6	Transformation to the global coordinate system	45
3.7	Technique for avoiding singularity	45
3.8	Closing remarks	46
4	Interface formulation	47
4.1	Introduction	47

4.2	Implementation aspects	47
4.3	Mixed-mode bilinear cohesive zone model	49
4.4	Mixed-mode linear-exponential cohesive zone model	56
4.5	Contact	59
4.6	Solution procedure and numerical integration	60
4.7	Numerical tests	62
4.8	Closing remarks	70
5	Delamination onset and growth in composite shells	71
5.1	Introduction	71
5.2	Recovery of interlaminar stresses using interface model	71
5.3	Recovery of interlaminar stresses using equilibrium equation	72
5.4	Prediction of delamination onset	75
5.5	Solution procedure	75
5.6	Numerical tests	77
	5.6.1 Interface model	77
	5.6.2 Equilibrium equation model	80
5.7	Closing remarks	83
6	Buckling analysis	85
6.1	Linear buckling analysis	85
	6.1.1 Numerical tests of linear buckling analysis	86
6.2	Non-linear buckling analysis	92
	6.2.1 Numerical tests of non-linear buckling analysis	97
6.3	Closing remarks	104
7	Delamination analysis in composites of variable stiffness	105
7.1	Introduction	105
7.2	Numerical tests	107
7.3	Closing remarks	110
8	Final example	113
9	Conclusions and future work	117
	Bibliography	120
	Curriculum vitae	130

Chapter 1

Introduction

1.1 Motivation

The word composite refers to the combination of two or more materials on a macroscopic scale to form a material with better advantages. Fibrous composite structures are available in the nature. For instance, the construction of leaves of trees, the wings of birds and the fins of fish can be considered as fibrous composite systems. Fibrous composite objects were primary produced by the Egyptians as papyrus papers. The Egyptians laid up strips from the fibrous papyrus plants to produce a symmetric composite laminate. In addition, people in the ancient Near East used straw to strengthen mud bricks (Herakovich, 2012). Thanks to the development of manufacturing technologies and based on the traditional experiences of human beings nowadays multi-layered composite laminates are produced. These composites consists of fibres that are laid in the matrix to produce a composite ply, and subsequently, composite plies stack together to construct a multi-layered laminate. The schematic view of fibres and matrices in a multi-layered laminate is shown in figure 1.1.

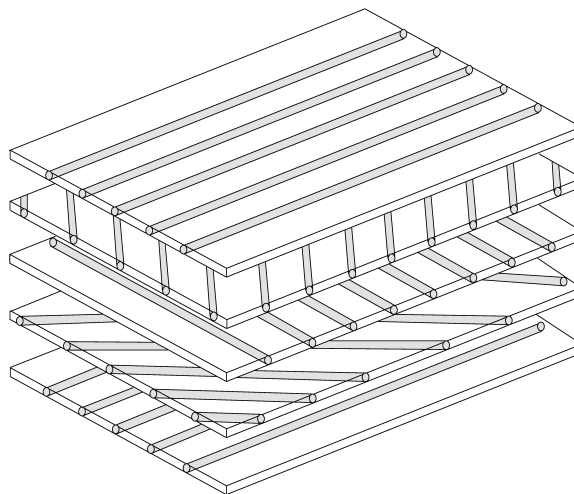


Figure 1.1: Schematic view of fibre reinforced plastic laminate.

The advantage of using a material in fibrous form is that long fibres are much stiffer

and stronger than the same material in bulk form. This is due to the fact that in fibres crystals are aligned along the fibre axis. Matrix materials are made of polymers, metals, ceramics, or carbon and they are used to bond the fibres within each ply. Furthermore, matrix can support and protect the fibres and transfer the stress between broken fibres (Jones, 1998). Fibre orientation of each ply is designed based on the type of loading or the application purpose. Thus, the directional dependence of strength and stiffness of the composite laminate matches by the loading condition. Though, like all materials, failure occurs in composite laminates. Due to the lamination the load-carrying capacity of these structures is limited in transverse direction. This issue arises once they are manufactured using orthotropic materials. That's the reason why damage in composite materials is categorised by two distinct types of failure: intralaminar and interlaminar failure. The intralaminar failure is related to the strength of components, being fibre and matrix, while interlaminar failure occurs due to interfacial damage. Furthermore, the failure in composite materials is followed at different scales. For example, micro cracks initially occur in the matrix areas that substantially have influence on the interfacial weakness of the structure at the corresponding scale. At macroscale, laminated plate and shell structures are appropriate when the structure is subjected to in-plane, bending, or combined loading conditions.

Delamination is categorized as a sort of interlaminar failure. It is considered as one major mode of failure in composite laminates. The delamination is defined as the separation of layers during the loading process. The collapse of a composite shell because of the delamination in the experimental test is shown in figure 1.2.



Figure 1.2: Collapse of a composite laminate due to the delamination (Bisagni, 2006).

The inevitable imperfections produced in the manufacturing process, the fatigue

load, the stress concentration near discontinuities, and the high interlaminar stress values are the main causes to provoke the delamination (Barbero, 2013). In addition, in the engineering applications, the delamination occurs due to three main reasons: impact loads, type of loading, and growing interlaminar stresses. The impact loads leave traction forces at the interface region, which lead to the separation of layers. In some cases, the type of loading produces intensive bending moments. These moments induce transverse normal stresses that consequently lead to the delamination. The last but important case is the growing interlaminar stresses during the loading process that is intensified close to the edges of laminate.

The sequence of damage in composite materials under compression was reported by Goyal et al. (2004) as buckling, intralaminar failure, and delamination, respectively. It was concluded that the intralaminar failure plays an important role to induce the delamination phenomenon. Since the nature of delamination primarily corresponds to the stacking sequences, type of load and growing interlaminar stresses, most of the current research is devoted to this phenomenon in particular. Delamination can be initiated by the occurrence of matrix cracking. Generally, this type of failure is observed in the laminate under bending or transverse load. Since the phenomenon is pretty complex and the fracture mode mixing at the delamination front is non-avoidable, the simulation tools using the finite element method can be exploited to precisely follow the corresponding fracture mode involved in the fracture process zone (Sridharan, 2008). In case of flat plates under tensile loading condition, the interlaminar stresses suddenly grow at the free edges, owing to the mismatch of engineering properties and Poisson's ratio or mutual effects (Robbins and Reddy, 1993). In addition, inclusion of a notch, ply drop, bolted joint, and cracked surface in laminates are other reasons of growing interlaminar stresses in a plate under tension. In contrary, local buckling induces interlaminar stresses at the buckled region in plates under compression (Garg, 1988).

1.2 State of the art

Many attempts have been made in the last decades to develop appropriate tools for the simulation of failure in composites laminates. The aim is to efficiently predict the failure phenomena at the process zone of damaged areas. The difficulty in the simulation process of these materials lies in two main aspects: the complex behaviour of composite materials itself and numerical deficiencies.

In general, due to the sophisticated nature of damage in laminated composites, each failure category has been independently investigated. Methods that are applied to detect the onset of damage are based on strength of material or fracture mechanics. It is worth noticing that the available criteria for the damage onset in composite materials were developed based on fitting curves to the experimental data; thus they lead to almost the same results (Reddy and Pandey, 1987). Despite that, looking for singularities in the stiffness matrix of the problem can also be an indicator of damage occurrence. The intralaminar failure is generally modelled based on the ply discontinuing method using knock down factors of material properties or by means of a continuum damage approach. The simulation of the interlaminar failure needs advanced tools that

combine damage and fracture mechanics, such as a cohesive zone model. The cohesive zone models apply a mixture of these approaches to follow the initiation and propagation of failure mechanisms. In both methodologies, a gradual reduction of the material properties should be assumed to satisfy gradual unloading in the experimental analysis and to avoid numerical problems. Nevertheless, instant reduction of stiffnesses can also be provided by incorporating several damage parameters for each individual mode of failure (Balzani and Wagner, 2010). Hu et al. (2007) decomposed the in-plane and out-of-plane damages: for the in-plane damage, the stiffness components of the corresponding mode were reduced whereas the out-of-plane failure was traced only at the interface that was located in the middle of thickness and cohesive elements were applied for this purpose.

Failure mode interactions is also of importance and should be taken into account (Goyal et al., 2004). For example, Reedy et al. (1997) detected the occurrence of several modes of failure during the numerical analysis of a ring subjected to transverse loading condition; nonetheless, the delamination failure was reported as an important mode in the damage analysis. Furthermore, several drops in the load-displacement diagram of composite laminates are observed that indicate the existence of numerous modes of failure. At macroscale, depending on the stacking sequence or the type of structure, primary failure is related to the first ply failure or the delamination. Next, the structure sustains further loads but can undergo several local failures as well. Therefore, the first ply failure should not be assumed as the final failure in the loading history (Gummadi and Palazotto, 1998).

Apart from the failure mechanics in composites, simulating the behaviour of multi-layered composite laminates under loading is of importance. Plate and shell theories are widely used to simulate the response of laminated composite structures. Due to the small thickness of these structures in comparison to the planar ones, the problem can be approximated by a pre-assumed displacement field that is defined with respect to the mid-plane of laminate. The through-the-thickness displacement field can vary in linear or higher-order format. Depending on the accuracy of the displacement field, the response of thicker laminates can become significant. In other words, the differences between the theories are decreased when the length-to-thickness ratio is increased. However, more sophisticated displacement fields lead to high computation cost, especially in case of non-linear analysis.

In multi-layered laminates the material properties and fibre angles may vary at each particular ply. In order to simulate the laminated structure, the equivalent single layer theory is used, whereby the laminate is approximated by only a single layer. By taking into account all of the aforementioned assumptions, the computational cost is drastically reduced and the bending performance of these structures can be accurately represented. The buckling phenomenon in shell structures affects the transverse properties and this might be followed by the nucleation of delamination. Thus, accounting the geometrically non-linear terms is important. Apart from this fact, the effect of geometrical non-linearity on the accurate prediction of failure in composite laminates was already proven in Reddy et al. (1995). By considering the geometrically non-linear terms, the maximum predicted load is being reduced.

The simulation tool should be capable of taking into account the delamination or any discontinuity through the thickness of the laminate. However, in the equivalent single layer theory the possibility to include the discontinuity in the thickness of a laminate is not available. Therefore, the delaminated interface is commonly modelled using two separate laminates, using the double-node technique. In this approach each separate laminate is simulated using the provided shell formulation and constraints are used to form the delamination front.

Interlaminar stresses are used in the delamination onset criterion. Therefore, the numerical problems that correspond to calculate of these stresses should be eliminated. Since the calculated interlaminar stresses at the free edges are singular, typically a very fine mesh should be applied within the finite element method to model the stress concentration in this region. Another method is to compute the average value of stresses over a pre-assumed distance from the edge of plate and then put them into the delamination criterion (Fenske and Vizzini, 2001). However, even by overcoming the aforementioned difficulties, the calculated normal transverse stress is not precise. Moreover, by exploiting more sophisticated three dimensional theories like the layerwise approach, errors can occur (Groh et al., 2015). Hence, the results of these stresses can only be used in the delamination onset criterion as indicator of the location of delamination in the structure (Gummadi and Palazotto, 1998).

In this thesis, the focus is on the interlaminar failure and the delamination of laminates within shells. Thus, a flat-shell formulation is developed based on a First-order Shear Deformation Theory (FSDT). In addition, the Equivalent Single Layer Theory (ESLT) is incorporated to include multi-layered composite laminates. In order to simulate the debonded region, the formulation itself is enhanced by the eXtended Finite Element Method (XFEM). Therefore, the same mesh scheme can be applied and the simulation of subdomains using double-nodes is avoided. The developed formulation can predict the response of intact or delaminated composite shells in the linear and geometrically non-linear regime. Since the XFEM can model displacement jumps at the debonded interface, the implementation of traction-separation law is also facilitated. Since the delamination can be initiated at any arbitrary interface, the simulation model should be efficient enough to monitor any potential location of delamination. Therefore, the most common approach is to simulate the multi-layered laminate in such a way that all plies are discontinuous whilst they are modelled as separate laminates. Afterwards, the cohesive elements with zero thickness but a physically negligible geometry are inserted between the interfaces to predict the damage and fracture process. This method is numerically expensive, especially when the geometrically non-linear response of the shell structure contributes to the solution process. Moreover, the negligible geometry of the cohesive elements that is used in simulation process can influence the accuracy of results. Herein, a novel algorithm is proposed to overcome the aforementioned deficiencies. In the present approach, the cohesive formulation is provided through the availability of enhanced degrees of freedom (DOFs) in the formulation of XFEM; therefore, no effort is needed to adjust the corresponding finite element meshes and the physical geometry of the cohesive elements is not modelled. Furthermore, taking into account a proper criterion for the delamination onset, the XFEM and cohesive

formulations can be activated locally at the critical interface or location within the plane of the shell. By doing so, the simulation can be carried out automatically using four-node elements and the computational cost and effort is decreased.

In this thesis all the aforementioned issues concerning the simulation of delamination in composite laminated plates and shells, and also the damage and fracture mechanics are investigated. The main focus is on developing an efficient toolkit that is itself original and it can be used to reduce the computational expenses.

1.3 Outline of the thesis

The formulations that are discussed in this thesis are divided into four particular theories namely: the theory of flat-shell formulation, the theory of XFEM, the interface formulations, and the interlaminar stress calculation. In chapter 2, the formulation of the developed shell theory is described in details. Next, techniques with regard to the reduction of numerical deficiencies of the shell formulation and the ESLT are discussed. In chapter 3, the XFEM formulation is incorporated to enhance the developed shell theory for the delamination analysis. The formulation of two types of mixed-mode cohesive zone model can be found in chapter 4. The first cohesive model developed is based on the bilinear traction-separation law whereas the second one is associated to the linear-exponential one. Both the aforementioned theories are derived in details and their implementation into the XFEM topology is described. In addition, a simple contact formulation is introduced to avoid the inward penetration of the discontinuous subdomains in the numerical analysis. At the end of this chapter, a few suggestions to overcome the numerical instabilities of the cohesive zone models are provided. In chapter 5, two principal approaches are presented to recover the interlaminar stresses. The first method takes advantage of interface model whereas in the second one the equilibrium equation of elasticity is used. Then, a novel algorithm is proposed to utilize the developed theories into an effective framework for the delamination analysis. The verification studies of each developed formulation are provided at the end of each corresponding chapter. In chapter 6, the present formulation is applied to perform the linear and non-linear buckling analysis. Several case studies are carried out to obtain the buckling and the delamination buckling response of composite laminates. In chapter 7, the delamination analysis of composite plates with curvilinear fibre format is studied and finally in chapter 8, the delamination analysis in an intact composite shell is investigated. The conclusions and possibilities for future works are given in chapter 9.

Chapter 2

A non-linear composite shell element

2.1 Theory of flat-shell

Coupling of membrane and bending response is of importance in composite laminated plates and shells. This coupling is observed in composite plates when the plies stack in an unsymmetric sequence. For this exceptional case, one might combine the stiffness matrices that are related to the mentioned coupling. However, in shell structures coupling between membrane and bending can occur, depending on the type of loading and the physical shape of the structures as well (Oñate, 2013). The different fashions of carrying load in plate and shell structures under the same transverse line load are shown in figure 2.1.

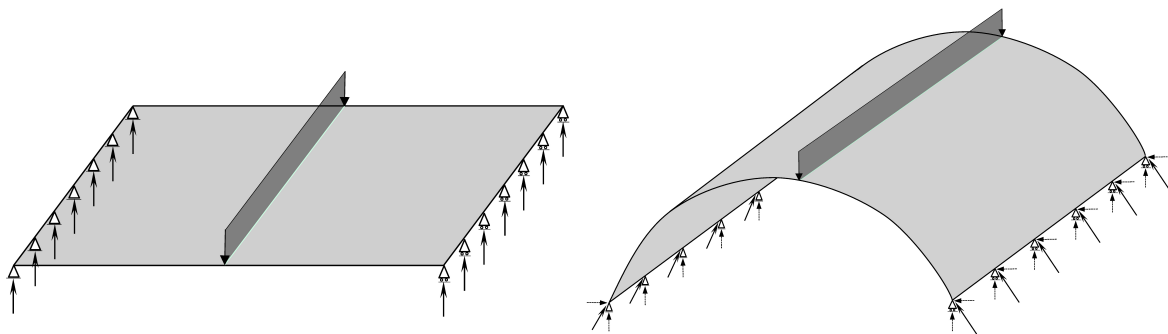


Figure 2.1: Schematic view of carrying load in plates and shells under the same line load.

In figure 2.1, although the same loading condition is applied for both structures, they are carried in different manners. This fact is more obvious on the boundary of the structures where the projections of reaction forces are coupled to the membrane and bending components. Unlike plates, a significant quantity of load is supported in normal and tangential direction by the mid-surface of shells.

Several possible formulations can be applied to describe the shell continuum and the kinematics; they can be categorized as follows (Wriggers, 2008):

- The kinematics of shells is classically represented with respect to a mid-surface. In this way the general three-dimensional governing equations are replaced by a set of equivalent equations leading to the establishment of shell theories. The deformation in thickness direction is modelled by defining an approximated displacement field. The displacement field can be represented by kinematic variables in linear or higher-order variation. Depending on the complexity of the displacement field, the response of thicker shells can be activated.
- Shell kinematics can be introduced by using the equations of a three-dimensional solid in the so-called degenerated concept. Therefore, based on the three-dimensional nature of these formulations, the assumption of stress resultants in shell theory is not applied. In this method the kinematic descriptions are used for the discretization of a shell continuum instead of a shell theory.
- Shell formulation can be directly developed from the continuum elements. In this approach, the mid-surface of shell is not introduced explicitly; instead, the nodes of the continuum elements are located at the upper and lower sides of the shell continuum for discretization using low order element.

A common assumption of the aforementioned theories is that the cross sections remain plane during deformation. In fact, this assumption represents shear deformable theories. A shell theory is called geometrically exact when no further assumption is incorporated in the development of formulation.

Shell structures can simply undergo bending loads. Therefore, the rotation of cross section should be carefully assigned in the displacement approximation. In classical Kirchhoff–Love hypothesis apart from the translational degrees of freedom, the rotation of mid-surface is defined by functions $\frac{\partial w_0}{\partial x}$ and $\frac{\partial w_0}{\partial y}$. Thus, the number of degrees of freedom per node remains the same as a solid element. However, in this formulation C^1 -continuous interpolation functions are required. The rotational degrees of freedom can be intrinsically embedded in the displacement field by defining rotational variables in x , y , and z directions. Hence, C^0 -continuous interpolation functions can be used within the finite element method.

Shell elements are categorized into three general classes:

- (a) Axisymmetric shell elements: these elements can be used for the general shells of revolution. The axisymmetric shell formulations are very efficient because they basically reduce the dimension by one.
- (b) General shell elements: in these elements a curved middle surface is defined to handle any shapes of curvature. General shell formulations are mathematically complex since one has to formulate the singly or doubly curved geometry of the shell.
- (c) Flat-shell elements: in these elements the physical geometry of curvature is approximated through using plane elements.

Here, the method that will be used is based on the assembly of flat elements. These were developed by a first-order laminate theory with respect to a global coordinate

system. By doing so, the same kinematic formulations as in the curved shell elements are used; however, the physical configuration is approximated.

The flat-shell formulation is developed by assuming that the curved surface is being composed of small plate elements. Henceforth, two Cartesian coordinate systems, named local and global coordinates, are distinguished. The local coordinate system is located on each plate element while the global one is applied at structural level. In order to assemble the governing equation of the structure, a transformation is required from the local to the global coordinate system.

It is noted that at element level, it is necessary for an isoparametric formulation to use the coordinates ξ and η . Thus, one further transformation has to be established in the local Cartesian coordinate system, by means of the Jacobian matrix.

Figure 2.2 shows the schematic view of a simple shell structure that is constructed by flat-shell elements. The local and global Cartesian coordinate systems are defined by xyz and XYZ , respectively.

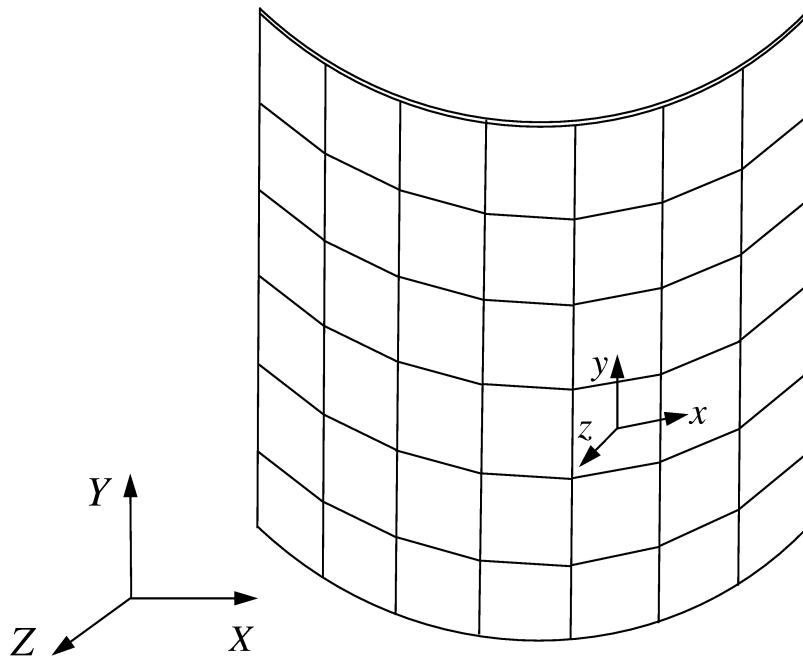


Figure 2.2: Shell structure assembled by flat elements.

2.2 Kinematics of shell

A first-order shear deformation theory is adopted. The theory follows precisely the assumption of Mindlin-Reissner plate theory (Reddy, 2004). The derivation of formulation for an element is given in the following subsections.

2.2.1 Displacement field

The model is based on a displacement-based finite element method where the mid-plane of laminate is considered as the reference. The adopted displacement field is linear and is defined with respect to the local Cartesian coordinate system that is associated with each element as

$$\begin{aligned} U(x, y, z) &= u^0(x, y) + z\theta_y^0(x, y) \\ V(x, y, z) &= v^0(x, y) - z\theta_x^0(x, y) \\ W(x, y, z) &= w^0(x, y) \end{aligned} \quad (2.1)$$

Here U , V , and W denote the displacements in x , y , and z directions, respectively; u^0 , v^0 , and w^0 present the displacement values of the mid-plane whereas θ_x^0 , θ_y^0 are the rotation of the mid-plane.

Four-node quadrilateral elements are used to discretise the domain. The nodes of elements are located on the mid-plane of the laminate and the displacement field is interpolated using the standard bilinear shape functions as

$$\begin{Bmatrix} u^0 \\ v^0 \\ w^0 \\ \theta_x^0 \\ \theta_y^0 \end{Bmatrix} = \sum_{i=1}^4 \begin{Bmatrix} N_i u_i^0 \\ N_i v_i^0 \\ N_i w_i^0 \\ N_i \theta_{x_i}^0 \\ N_i \theta_{y_i}^0 \end{Bmatrix} = \mathbf{N} \mathbf{q} \quad (2.2)$$

where \mathbf{N} is the matrix of shape functions and \mathbf{q} is the vector of unknown variables.

2.2.2 Strain field

By substituting the displacement field into the Green-Lagrange strain tensor and considering the non-linear terms related to only the membrane components, in-plane and out-of-plane strain fields are obtained as

$$\begin{Bmatrix} \varepsilon_{xx} \\ \varepsilon_{yy} \\ \gamma_{xy} \end{Bmatrix} = \begin{bmatrix} 1 & 0 & 0 & -z & 0 & 0 \\ 0 & 1 & 0 & 0 & -z & 0 \\ 0 & 0 & 1 & 0 & 0 & -z \end{bmatrix} \begin{Bmatrix} \boldsymbol{\varepsilon}_m^0 + \boldsymbol{\varepsilon}_{nl} \\ \boldsymbol{\varepsilon}_b^0 \end{Bmatrix} \quad (2.3)$$

$$\begin{Bmatrix} \gamma_{xz} \\ \gamma_{yz} \end{Bmatrix} = \begin{Bmatrix} w_{,x}^0 + \theta_y^0 \\ w_{,y}^0 - \theta_x^0 \end{Bmatrix}$$

where $\boldsymbol{\varepsilon}_m^0$, $\boldsymbol{\varepsilon}_b^0$, and $\boldsymbol{\varepsilon}_{nl}$ are respectively the membrane, bending, and non-linear strain terms. The subscript comma denotes a partial differentiation with respect to the local

Cartesian coordinate system. This yields

$$\boldsymbol{\varepsilon}_m^0 = \begin{Bmatrix} u_{,x}^0 \\ v_{,y}^0 \\ u_{,y}^0 + v_{,x}^0 \end{Bmatrix}, \quad \boldsymbol{\varepsilon}_b^0 = \begin{Bmatrix} -\theta_{y,x}^0 \\ \theta_{x,y}^0 \\ -\theta_{y,y}^0 + \theta_{x,x}^0 \end{Bmatrix} \quad (2.4)$$

and

$$\boldsymbol{\varepsilon}_{nl} = \begin{Bmatrix} \frac{1}{2}(u_{,x}^0)^2 + \frac{1}{2}(v_{,x}^0)^2 + \frac{1}{2}(w_{,x}^0)^2 \\ \frac{1}{2}(u_{,y}^0)^2 + \frac{1}{2}(v_{,y}^0)^2 + \frac{1}{2}(w_{,y}^0)^2 \\ u_{,x}^0 u_{,y}^0 + v_{,x}^0 v_{,y}^0 + w_{,x}^0 w_{,y}^0 \end{Bmatrix} \quad (2.5)$$

Substituting the discretised displacement field of equation 2.1 into the components of strain field, the discretised strain components are derived. They are presented in details in the following.

a) Membrane strain:

$$\boldsymbol{\varepsilon}_m^0 = \sum_{i=1}^4 \mathbf{B}_{m_i} \mathbf{q} \quad (2.6)$$

where \mathbf{B}_{m_i} is the membrane strain matrix. It is given by

$$\mathbf{B}_{m_i} = \begin{bmatrix} \frac{\partial N_i}{\partial x} & 0 & 0 & 0 & 0 \\ 0 & \frac{\partial N_i}{\partial y} & 0 & 0 & 0 \\ \frac{\partial N_i}{\partial y} & \frac{\partial N_i}{\partial x} & 0 & 0 & 0 \end{bmatrix} \quad (2.7)$$

b) Bending strain:

$$\boldsymbol{\varepsilon}_b^0 = \sum_{i=1}^4 \mathbf{B}_{b_i} \mathbf{q} \quad (2.8)$$

where \mathbf{B}_{b_i} is the bending strain matrix. It is written in matrix form as

$$\mathbf{B}_{b_i} = \begin{bmatrix} 0 & 0 & 0 & 0 & -\frac{\partial N_i}{\partial x} \\ 0 & 0 & 0 & \frac{\partial N_i}{\partial y} & 0 \\ 0 & 0 & 0 & \frac{\partial N_i}{\partial x} & -\frac{\partial N_i}{\partial y} \end{bmatrix} \quad (2.9)$$

c) Shear strain:

$$\boldsymbol{\gamma} = \sum_{i=1}^4 \mathbf{B}_{s_i} \mathbf{q} \quad (2.10)$$

where \mathbf{B}_{s_i} is the shear strain matrix. It is provided by

$$\mathbf{B}_{s_i} = \begin{bmatrix} 0 & 0 & \frac{\partial N_i}{\partial x} & 0 & N_i \\ 0 & 0 & \frac{\partial N_i}{\partial y} & -N_i & 0 \end{bmatrix} \quad (2.11)$$

d) Non-linear stain:

$$\boldsymbol{\varepsilon}_{nl} = \frac{1}{2} \mathbf{G}_u \sum_{i=1}^4 \mathbf{B}_{nlu_i} \mathbf{q} + \frac{1}{2} \mathbf{G}_v \sum_{i=1}^4 \mathbf{B}_{nlv_i} \mathbf{q} + \frac{1}{2} \mathbf{G}_w \sum_{i=1}^4 \mathbf{B}_{nlw_i} \mathbf{q} \quad (2.12)$$

where the above matrices are written as

$$\mathbf{G}_u = \begin{bmatrix} u_{,x}^0 & 0 & 0 \\ 0 & u_{,y}^0 & 0 \\ u_{,y}^0 & u_{,x}^0 & 0 \end{bmatrix}, \quad \mathbf{G}_v = \begin{bmatrix} v_{,x}^0 & 0 & 0 \\ 0 & v_{,y}^0 & 0 \\ v_{,y}^0 & v_{,x}^0 & 0 \end{bmatrix}, \quad \mathbf{G}_w = \begin{bmatrix} w_{,x}^0 & 0 & 0 \\ 0 & w_{,y}^0 & 0 \\ w_{,y}^0 & w_{,x}^0 & 0 \end{bmatrix} \quad (2.13)$$

and

$$\mathbf{B}_{nlu_i} = \begin{bmatrix} \frac{\partial N_i}{\partial x} & 0 & 0 & 0 & 0 \\ \frac{\partial N_i}{\partial y} & 0 & 0 & 0 & 0 \\ 0 & 0 & 0 & 0 & 0 \end{bmatrix}, \quad \mathbf{B}_{nlv_i} = \begin{bmatrix} 0 & \frac{\partial N_i}{\partial x} & 0 & 0 & 0 \\ 0 & \frac{\partial N_i}{\partial y} & 0 & 0 & 0 \\ 0 & 0 & 0 & 0 & 0 \end{bmatrix}, \quad \mathbf{B}_{nlw_i} = \begin{bmatrix} 0 & 0 & \frac{\partial N_i}{\partial x} & 0 & 0 \\ 0 & 0 & \frac{\partial N_i}{\partial y} & 0 & 0 \\ 0 & 0 & 0 & 0 & 0 \end{bmatrix} \quad (2.14)$$

2.3 Constitutive equation

A linear relation between the second Piola–Kirchhoff stress tensor and the Green strain tensor is assumed. The constitutive behaviour of laminated composites can be described using an orthotropic or transversal isotropic material law. In orthotropic materials, three orthogonal planes of material symmetry exist. Therefore, the number of elastic coefficient in the constitutive equation is reduced to nine. The strain-stress relation in the principal material coordinate system is written as

$$\boldsymbol{\varepsilon} = \mathbf{S} \boldsymbol{\sigma} \quad (2.15)$$

where

$$\boldsymbol{\varepsilon} = \begin{Bmatrix} \varepsilon_1 \\ \varepsilon_2 \\ \varepsilon_3 \\ \varepsilon_4 \\ \varepsilon_5 \\ \varepsilon_6 \end{Bmatrix}, \quad \boldsymbol{\sigma} = \begin{Bmatrix} \sigma_1 \\ \sigma_2 \\ \sigma_3 \\ \sigma_4 \\ \sigma_5 \\ \sigma_6 \end{Bmatrix}, \quad \mathbf{S} = \begin{bmatrix} \frac{1}{E_{11}} & -\frac{\nu_{21}}{E_{22}} & -\frac{\nu_{31}}{E_{33}} & 0 & 0 & 0 \\ -\frac{\nu_{12}}{E_{11}} & \frac{1}{E_{22}} & -\frac{\nu_{32}}{E_{33}} & 0 & 0 & 0 \\ -\frac{\nu_{13}}{E_{11}} & -\frac{\nu_{23}}{E_{22}} & \frac{1}{E_{33}} & 0 & 0 & 0 \\ 0 & 0 & 0 & \frac{1}{G_{23}} & 0 & 0 \\ 0 & 0 & 0 & 0 & \frac{1}{G_{13}} & 0 \\ 0 & 0 & 0 & 0 & 0 & \frac{1}{G_{12}} \end{bmatrix} \quad (2.16)$$

where E_{11} is the longitudinal modulus and E_{22} is the transverse modulus; ν_{12} and ν_{21} are Poisson's ratios; G_{12} is the in-plane shear modulus, while G_{13} and G_{23} are transverse shear moduli. ν_{21} parameter can be calculated by $\nu_{21}/E_{11} = \nu_{12}/E_{22}$. These material properties are determined independently by uniaxial tension test or pure shear tests in experiment.

In composite laminates, fibres can be placed in different angles with respect to the coordinate natural to the solution of the problem. In other words, the fibre angle may

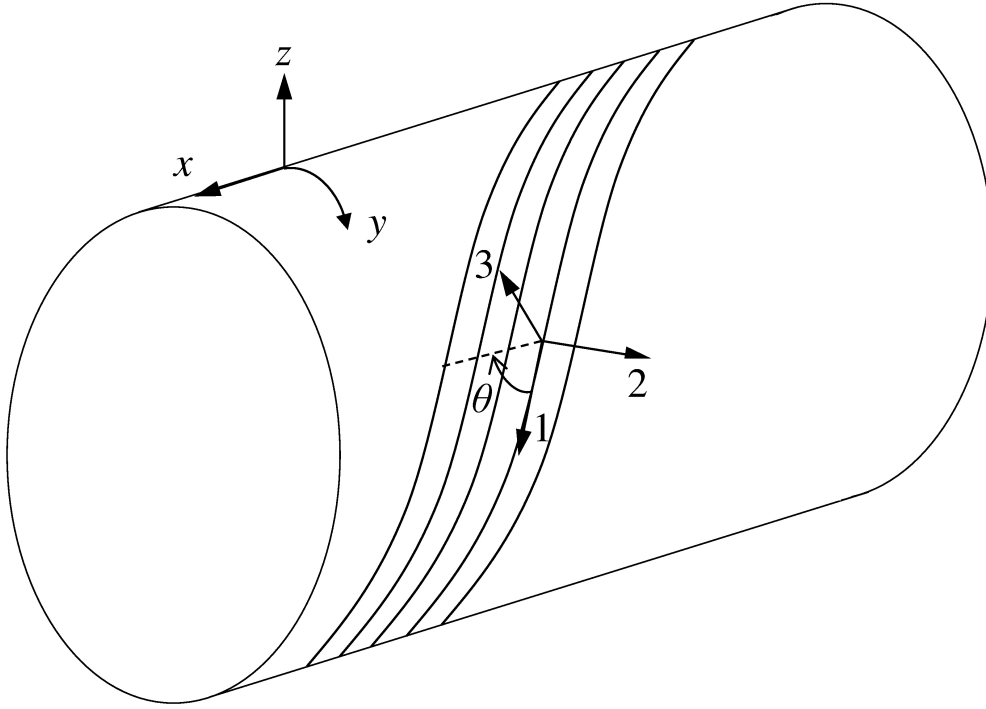


Figure 2.3: Schematic view of principal and local coordinate system.

not coincide with the local coordinate system xyz . The schematic view of the principal and local coordinate systems are shown in figure 2.3.

Since all formulations are derived with respect to the local coordinate system of element, a transformation is needed to hold the constitutive equation in this coordinate. The transformation is written as the cosine of the principal coordinate system with respect to the local coordinate system. Therefore, strain and stress components in xyz coordinate system are calculated. The stress-strain relation in the corresponding Cartesian coordinate system is defined as (Jones, 1998)

$$\boldsymbol{\sigma} = \bar{\mathbf{Q}}\boldsymbol{\varepsilon} \quad (2.17)$$

where

$$\boldsymbol{\sigma} = \begin{Bmatrix} \sigma_x(x, y, z) \\ \sigma_y(x, y, z) \\ \tau_{xy}(x, y, z) \\ \tau_{yz}(x, y, z) \\ \tau_{xz}(x, y, z) \end{Bmatrix}, \boldsymbol{\varepsilon} = \begin{Bmatrix} \varepsilon_x(x, y, z) \\ \varepsilon_y(x, y, z) \\ \gamma_{xy}(x, y, z) \\ \gamma_{yz}(x, y, z) \\ \gamma_{xz}(x, y, z) \end{Bmatrix}, \bar{\mathbf{Q}} = \begin{bmatrix} \bar{Q}_{11} & \bar{Q}_{12} & \bar{Q}_{16} & 0 & 0 \\ \bar{Q}_{12} & \bar{Q}_{22} & \bar{Q}_{26} & 0 & 0 \\ \bar{Q}_{16} & \bar{Q}_{26} & \bar{Q}_{66} & 0 & 0 \\ 0 & 0 & 0 & \bar{Q}_{44} & \bar{Q}_{45} \\ 0 & 0 & 0 & \bar{Q}_{45} & \bar{Q}_{55} \end{bmatrix} \quad (2.18)$$

where $\bar{\mathbf{Q}}$ is the constitutive matrix of orthotropic materials that is determined based

on the material properties and the fibre orientation of each ply. It is written as

$$\begin{aligned}
\bar{Q}_{11} &= U_1 + U_2 \cos(2\theta) + U_3 \cos(4\theta) \\
\bar{Q}_{12} &= U_4 - U_3 \cos(4\theta) \\
\bar{Q}_{22} &= U_1 - U_2 \cos(2\theta) + U_3 \cos(4\theta) \\
\bar{Q}_{16} &= \frac{1}{2} U_2 \sin(2\theta) + U_3 \sin(4\theta) \\
\bar{Q}_{26} &= \frac{1}{2} U_2 \sin(2\theta) - U_3 \sin(4\theta) \\
\bar{Q}_{66} &= U_5 - U_3 \cos(4\theta) \\
\bar{Q}_{44} &= U_6 + U_7 \cos(2\theta) \\
\bar{Q}_{45} &= -U_7 \sin(2\theta) \\
\bar{Q}_{55} &= U_6 - U_7 \cos(2\theta)
\end{aligned} \tag{2.19}$$

where θ is the fibre angle of each ply. The transformed stiffness parameters are written in terms of invariants U_i , $i=1$ to 7. These invariants are not affected by fibre orientations and they are particularly calculated based on the orthotropic material properties. They are defined as

$$\begin{aligned}
U_1 &= \frac{1}{8} (3Q_{11} + 3Q_{22} + 2Q_{12} + 4Q_{66}) \\
U_2 &= \frac{1}{2} (Q_{11} - Q_{22}) \\
U_3 &= \frac{1}{8} (Q_{11} + Q_{22} - 2Q_{12} - 4Q_{66}) \\
U_4 &= \frac{1}{8} (Q_{11} + Q_{22} + 6Q_{12} - 4Q_{66}) \\
U_5 &= \frac{1}{8} (Q_{11} + Q_{22} - 2Q_{12} + 4Q_{66}) \\
U_6 &= \frac{1}{2} (Q_{44} + Q_{55}) \\
U_7 &= \frac{1}{2} (Q_{44} - Q_{55})
\end{aligned} \tag{2.20}$$

where the material stiffness coefficients Q_{ij} are:

$$\begin{aligned}
Q_{11} &= \frac{E_{11}}{1 - \nu_{12}\nu_{21}} \\
Q_{22} &= \frac{E_{22}}{1 - \nu_{12}\nu_{21}} \\
Q_{12} &= \frac{\nu_{12}E_{22}}{1 - \nu_{12}\nu_{21}} = \frac{\nu_{21}E_{11}}{1 - \nu_{12}\nu_{21}} \\
Q_{44} &= G_{23} \\
Q_{55} &= G_{13} \\
Q_{66} &= G_{12}
\end{aligned} \tag{2.21}$$

2.4 Shear correction factor

Although the first-order shear deformation theory is applicable to model thin to moderately thick laminates, the transverse shear strains remain constant through the thickness of each ply. In the multi-layered composite laminates especially in sandwich structures in that the stiffness of layers is changed abruptly, the model is revised by the so-called shear correction factor. The value of this factor in homogeneous isotropic plates is set to 5/6 (Birman and Bert, 2002); however, one has to compute it in case of composite laminates. The factor is determined by discovering the ratio of acquired strain energy in elasticity to the one of the FSDT.

Due to the different material properties in the general lay-up laminates, neutral surface of the multi-layered laminates is differed from the geometrical one. Therefore, the following formula is utilized to obtain the new neutral surface of a continuous laminate

$$z_{nt} = \frac{\int_{-h/2}^{h/2} Q_{11}(z) z dz}{\int_{-h/2}^{h/2} Q_{11}(z) dz} \tag{2.22}$$

where z_{nt} is the new location of the neutral plane in the thickness direction, and $Q_{11}(z)$ is defined by

$$Q_{11}(z) = \frac{E_{11}}{1 - \nu_{12}\nu_{21}} \tag{2.23}$$

where E_{11} and ν_{12} are the Young's modulus in the fibre direction and the in-plane Poisson's ratio, respectively. Using the equilibrium equation of elasticity, and assuming the cylindrical bending condition (see Ferreira (2003)), transverse stresses are attained as

$$\tau_{xz} = - \int_{-h/2}^z \frac{\partial \sigma_x}{\partial x} dz \tag{2.24}$$

Considering M_x as the bending moment, the stress in x direction is calculated by the

following equation

$$\sigma_x = M_x \frac{Q_{11}(z)}{\int_{-h/2}^{h/2} Q_{11}(z)(z - z_{nt})^2 dz} z \quad (2.25)$$

Substituting equation 2.25 into equation 2.24, the transverse stress in x direction is derived as

$$\tau_{xz} = \frac{T_x}{\int_{-h/2}^{h/2} Q_{11}(z)(z - z_{nt})^2 dz} \left(- \int_{-h/2}^z Q_{11}(z)z dz \right) \quad (2.26)$$

where T_x is the shear force which is obtained from the variation of bending moment in x direction on the xz plane. By substituting the transverse stress obtained by the theory of elasticity into the formulation of strain energy, the following equation is achieved

$$U_{sh}^e = \int_{-h/2}^{h/2} \frac{\tau_{xz}^2}{G_{13}(z)} dz = \frac{T_x^2}{\left(\int_{-h/2}^{h/2} Q_{11}(z)(z - z_{nt})^2 dz \right)^2} \int_{-h/2}^{h/2} \frac{\left(- \int_{-h/2}^z Q_{11}(z)z dz \right)^2}{G_{13}(z)} dz \quad (2.27)$$

where U_{sh}^e is the strain energy of elasticity. In addition, the constant shear stresses of plate theory can be applied to calculate the strain energy as

$$\bar{U}_{sh} = \int_{-h/2}^{h/2} \bar{\gamma}_{xz} G_{13}(z) \bar{\gamma}_{xz} dz = \frac{T_x^2}{\int_{-h/2}^{h/2} G_{13}(z) dz} \quad (2.28)$$

Thereafter, the shear correction factor is acquired by dividing the strain energy calculated by equation 2.27 to the one of equation 2.28. By using the material properties, fibre orientation and the location of neutral surface of the laminate, the integration in the denominator of equation 2.27 can be explicitly calculated. However, the integral in the numerator is numerically integrated. For this, the integration inside leads to a fourth-order polynomial that can be integrated by means of three Gaussian integration points per layer.

2.5 Assumed transverse shear strain field

First-order shear deformation theories like any lower-order theory suffer from the locking phenomena. This issue arises when thin structures are surveyed, and as a result, less deflection is achieved under bending loads. To overcome the locking phenomena, the shear stiffness matrix is revised to a singular format, independently. To do so, one approach is to apply the reduced integration scheme. However, this fashion mostly causes the hour-glassing phenomenon in the deformed plate elements. Another approach is to modify the formulation by linearly varying the transverse strain field in one direction that is assumed constant in the FSDT formulation (Oñate, 2013). This methodology was proposed for quadrilateral plate elements in Oñate et al. (1992). Four

sampling points on the edges of the element besides the nodal points are assumed. A linear distribution of transverse strains is interpolated between the sampling points in ξ and η directions of the local coordinate system. The new strain field is presented as

$$\boldsymbol{\gamma}_{\bar{\xi}} = \begin{Bmatrix} \gamma_{\xi} \\ \gamma_{\eta} \end{Bmatrix} = \mathbf{J} \begin{Bmatrix} \gamma_{xz} \\ \gamma_{yz} \end{Bmatrix} = \begin{bmatrix} 1 & \eta & 0 & 0 \\ 0 & 0 & 1 & \xi \end{bmatrix} \begin{Bmatrix} c_1 \\ c_2 \\ c_3 \\ c_4 \end{Bmatrix} \quad (2.29)$$

where γ_{ξ} and γ_{η} are the transverse strains in ξ and η directions, respectively; c_i are the new unknown variables, and \mathbf{J} is the Jacobian matrix being evaluated at sampling points. A schematic view of the transverse shear strain distribution and the sampling points are shown in figure 2.4.

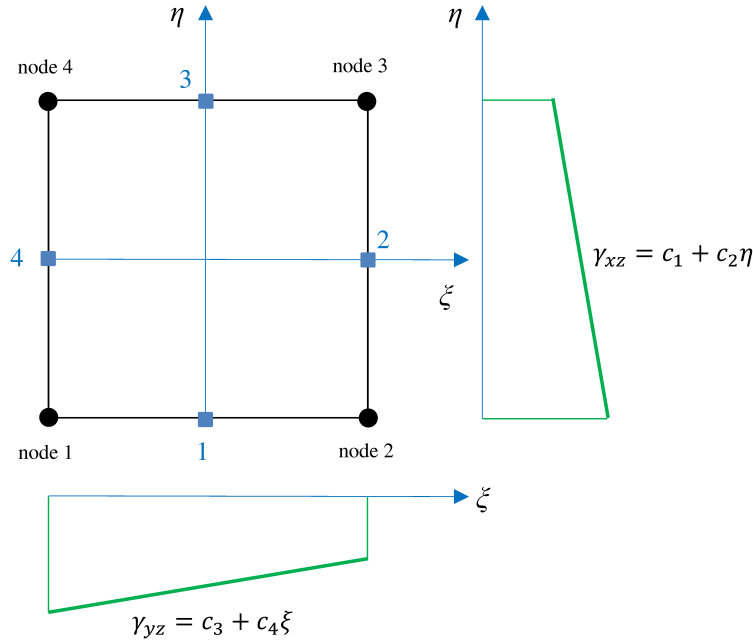


Figure 2.4: Schematic view of the assumed transverse shear strain field with sampling points.

As it is shown in figure 2.4, the transverse shear strain field linearly varies in x direction for sampling point 1 and 3 whereas it is constant in y direction. The same condition holds for sampling points 2 and 4 but in opposite direction. Thus, by evaluating the introduced transverse shear strain field (equation 2.29) at each sampling point, c_i variables are obtained in term of the transverse shear strain components. Thereafter, one can rewrite the introduced transverse shear strain field for each element

in the following format

$$\begin{Bmatrix} \gamma_\xi \\ \gamma_\eta \end{Bmatrix} = \begin{bmatrix} 1/2(1-\eta) & 0 & 0 & 0 & 1/2(1+\eta) & 0 & 0 & 0 \\ 0 & 0 & 0 & 1/2(1+\xi) & 0 & 0 & 0 & 1/2(1-\xi) \end{bmatrix} \begin{Bmatrix} \gamma_\xi^1 \\ \gamma_\eta^1 \\ \vdots \\ \gamma_\xi^4 \\ \gamma_\eta^4 \end{Bmatrix} \quad (2.30)$$

where γ_ξ^i and γ_η^i are the shear strain values from the FSDT at each sampling point i . Therefore, by substituting the corresponding formulation into equation 2.30 and transforming it to a Cartesian coordinate system, using the Jacobian matrix, the enhanced shear strain matrix is derived as follows

$$\mathbf{B}_s^{\text{enh}} = \mathbf{J}_i^{-1} \begin{bmatrix} 1/2(1-\eta) & 0 & 0 & 0 & 1/2(1+\eta) & 0 & 0 & 0 \\ 0 & 0 & 0 & 1/2(1+\xi) & 0 & 0 & 0 & 1/2(1-\xi) \end{bmatrix} \begin{Bmatrix} \mathbf{J}^1 & 0 & 0 & 0 \\ 0 & \mathbf{J}^2 & 0 & 0 \\ 0 & 0 & \mathbf{J}^3 & 0 \\ 0 & 0 & 0 & \mathbf{J}^4 \end{Bmatrix} \begin{Bmatrix} \mathbf{B}_s^1 \\ \mathbf{B}_s^2 \\ \mathbf{B}_s^3 \\ \mathbf{B}_s^4 \end{Bmatrix} \quad (2.31)$$

where \mathbf{J} is the Jacobian matrix and \mathbf{B}_s^i is the standard transverse shear strain matrix at sampling point i . By substituting the enhanced shear strain matrix $\mathbf{B}_s^{\text{enh}}$ into the governing equations locking is avoided.

2.6 Equilibrium equation

The Principle of Virtual Work (PVW) which is convenient for the displacement-based finite element is adopted to obtain the equation of equilibrium. Thus, the non-linear equilibrium equation is written in the following form

$$\mathbf{R}(\mathbf{q}) = \mathbf{f}^{\text{int}}(\mathbf{q}) - \mathbf{f}^{\text{ext}} = \int_V \mathbf{B}^T \boldsymbol{\sigma} dV - \mathbf{f}^{\text{ext}} = \mathbf{0} \quad (2.32)$$

where \mathbf{R} is the residual vector, \mathbf{f}^{int} and \mathbf{f}^{ext} are internal and external force vectors, respectively; \mathbf{B} contains linear and non-linear strain matrices, and \mathbf{q} is the vector of generalised displacements.

The governing equations are discretised using four-node elements with bilinear shape functions. It is mentioned that all the formulations developed in the present thesis are coded as an element subroutine in ANSYS version 14.5 commercial software. In order to solve the non-linear equation 2.32, the full Newton-Raphson iterative method available in ANSYS software is used (ANSYS Documentation, 2013). The solution algorithm for the full Newton-Raphson method is written in the iterative manner

as

$$\mathbf{K}_{T_i}(\mathbf{q}_i) \Delta \mathbf{q}_i = \mathbf{f}^{ext} - \mathbf{f}_i^{int}(\mathbf{q}_i) \quad (2.33)$$

where $\mathbf{K}_T(\mathbf{q})$ and $\mathbf{f}^{int}(\mathbf{q})$ are the element tangent stiffness and the internal force vector, respectively; \mathbf{f}^{ext} is the external force vector. The subscript i represents the current iteration. It is noted that the tangent stiffness and internal force vector are functions of unknown values at iteration i . The calculated $\Delta \mathbf{q}_i$ are added to \mathbf{q}_i to obtain the new unknown approximation \mathbf{q}_{i+1} and they are used to calculate the tangent stiffness and internal force vector in the next iteration. This procedure is performed until the convergence is achieved, or in other words the equilibrium is governed. According to equation 2.33 the tangent stiffness matrix is updated at each iteration. This method is called a full Newton-Raphson solution algorithm.

The tangent stiffness matrix can be derived by calculating the derivatives of equation 2.32 with respect to \mathbf{q} as follows

$$\mathbf{K}_T = \frac{\partial \mathbf{R}}{\partial \mathbf{q}} \quad (2.34)$$

In some cases, it is not likely to acquire the equilibrium solution of specific load level in one load step. In addition, the load-deflection curve of some structures is complex and cannot simply be traced. Thus, the incremental Newton-Raphson procedure is introduced. In this method the applied load is divided into a number of increments and the equilibrium solution is obtained at the corresponding load level. By doing so, the possibility to carefully following the solution path is provided. Hence, the incremental Newton-Raphson method is written as

$$\mathbf{K}_{T_{n,i}}(\mathbf{q}_i) \Delta \mathbf{q}_i = \mathbf{f}_n^{ext} - \mathbf{f}_{n,i}^{int}(\mathbf{q}_i) \quad (2.35)$$

where n represents the number of increment.

The general non-linear analysis is performed by the load incrementation. Therefore, the simulation is carried out by applying a factor of maximum load amplitude in several increments. However, this method is not applicable once a snap-through problem is encountered. After such points, the slope of tangent is negative and cannot be traced by the force control algorithm. An alternative is to conduct a displacement control analysis. Thus, a prescribed displacement value in the tangent stiffness matrix leads to a pre-defined internal force value that retrieves the amplitude of load. This method is applicable in the absence of snap-back problem. In a system which is composed by snap-back and snap-through points, one solution is to switch between the aforementioned methods to carefully following the solution path. Another solution is to control a combination of these methods that is called the arc-length method. In this method a possible solution is determined within the arc-length radius. In the arc-length method both the load parameter and displacements are unknown. Thus, a constraint condition is superimposed to solve the non-linear governing equations

$$G(\Delta \mathbf{q}_n, \Delta \lambda_n) = \mathbf{0} \quad (2.36)$$

where $\Delta \mathbf{q}_n$ and $\Delta \lambda_n$ are the incremental values of displacement and load factor, respectively.

The Newton-Raphson method has a quadratic convergence property in the vicinity of the solution. This is clarified by comparing the norm of residual vector at iterations. Taking \mathbf{R}_i as the residual vector of iteration i , the convergence order can be calculated by (see e.g. Rust (2015))

$$\chi = \frac{\log(\|R_{i-1}\| / \|R_i\|)}{\log(\|R_{i-2}\| / \|R_{i-1}\|)} \quad (2.37)$$

where χ is the convergence order and $\chi=2$ assures a quadratic convergence.

2.7 Tangent stiffness matrix derivation

In the absence of external forces, the residual equation is limited to the internal force vector. Thus, by substituting equation 2.32 into equation 2.34 the tangent matrix is rewritten as

$$\mathbf{K}_T = \int_V \frac{\partial \mathbf{B}^T}{\partial \mathbf{q}} \boldsymbol{\sigma} dV + \int_V \mathbf{B}^T \frac{\partial \boldsymbol{\sigma}}{\partial \mathbf{q}} dV \quad (2.38)$$

As it was mentioned in section 2.2.2, \mathbf{B} consists of linear and non-linear strain matrices whence the derivatives of non-linear terms should be conducted in the first integral of equation 2.38. Furthermore, the derivative of stress vector with respect to \mathbf{q} in the second integral is performed as

$$\frac{\partial \boldsymbol{\sigma}}{\partial \mathbf{q}} = \frac{\partial \boldsymbol{\sigma}}{\partial \boldsymbol{\varepsilon}} \frac{\partial \boldsymbol{\varepsilon}}{\partial \mathbf{q}} \quad (2.39)$$

where $\frac{\partial \boldsymbol{\sigma}}{\partial \boldsymbol{\varepsilon}}$ corresponds to the constitutive matrix of orthotropic material $\bar{\mathbf{Q}}$, and $\frac{\partial \boldsymbol{\varepsilon}}{\partial \mathbf{q}}$ particularly associates to the strain matrices and their derivatives. By carefully carrying out the derivatives in the previous equations, one arrives at a tangent operator that can be split into three main components as

$$\mathbf{K}_T = \mathbf{K}_L + \mathbf{K}_U + \mathbf{K}_\sigma \quad (2.40)$$

where \mathbf{K}_L and \mathbf{K}_U are related to the second term of equation 2.38 whereas \mathbf{K}_σ is obtained from the first integral of equation 2.38. This split of tangent operator is useful when the linear buckling analysis is of interest. \mathbf{K}_U contains initial deformation of the structure and \mathbf{K}_σ is the so-called geometric stiffness matrix. Both the mentioned components are non-linear. These components are introduced in details as

$$\begin{aligned} \mathbf{K}_L = & \int_V \mathbf{B}_m^T \bar{\mathbf{Q}} \mathbf{B}_m dV - \int_V \mathbf{B}_m^T z \bar{\mathbf{Q}} \mathbf{B}_b dV - \int_V \mathbf{B}_b^T z \bar{\mathbf{Q}} \mathbf{B}_m dV + \\ & \int_V \mathbf{B}_b^T z^2 \bar{\mathbf{Q}} \mathbf{B}_b dV + \int_V \mathbf{B}_s^T z^2 \bar{\mathbf{Q}}_s \mathbf{B}_s dV \end{aligned} \quad (2.41)$$

The linear components of tangent are generally related to the membrane, bending, bending-membrane couplings, and shear. Since the developed theory is a two dimensional formulation, the resultant of stresses are taken into account. Thus, the volume

integrals in the tangent operator are performed as follows

$$\begin{aligned}
\mathbf{K}_L = & \iint_A \mathbf{B}_m^T \left[\int_{-h/2}^{h/2} \bar{\mathbf{Q}} dz \right] \mathbf{B}_m dA - \iint_A \mathbf{B}_m^T \left[\int_{-h/2}^{h/2} z \bar{\mathbf{Q}} dz \right] \mathbf{B}_b dA - \\
& \iint_A \mathbf{B}_b^T \left[\int_{-h/2}^{h/2} z \bar{\mathbf{Q}} dz \right] \mathbf{B}_m dA + \iint_A \mathbf{B}_b^T \left[\int_{-h/2}^{h/2} z^2 \bar{\mathbf{Q}} dz \right] \mathbf{B}_b dA + \\
& \iint_A \mathbf{B}_s^T \left[\int_{-h/2}^{h/2} \bar{\mathbf{Q}}_s dz \right] \mathbf{B}_s dA
\end{aligned} \tag{2.42}$$

If a linear structural analysis is of interest, \mathbf{K}_L stiffness suffices to obtain the structural behaviour of shell. However, in geometrically non-linear analysis, the remaining terms should be incorporated.

The geometric stiffness matrix is written as

$$\mathbf{K}_\sigma = \iint_A \left[\frac{\partial \mathbf{G}_u}{\partial \mathbf{q}} \mathbf{B}_{nlu} + \frac{\partial \mathbf{G}_v}{\partial \mathbf{q}} \mathbf{B}_{nlv} + \frac{\partial \mathbf{G}_w}{\partial \mathbf{q}} \mathbf{B}_{nlw} \right]^T \boldsymbol{\sigma}_r dA \tag{2.43}$$

where $\boldsymbol{\sigma}_r$ is the vector of in-plane stress resultants and matrices \mathbf{G}_i ($i=u, v, w$) were already derived in equation 2.13. The resultant stresses are integrals of in-plane stress components of equation 2.17 over the thickness of element.

The part of the tangent stiffness that is a function of the initial deformation is presented as

$$\begin{aligned}
\mathbf{K}_U = & \iint_A \mathbf{B}_m^T \left[\int_{-h/2}^{h/2} \bar{\mathbf{Q}} dz \right] \frac{1}{2} [\mathbf{G}_u \mathbf{B}_{nlu} + \mathbf{G}_v \mathbf{B}_{nlv} + \mathbf{G}_w \mathbf{B}_{nlw}] dA + \\
& \iint_A \mathbf{B}_m^T \left[\int_{-h/2}^{h/2} \bar{\mathbf{Q}} dz \right] \frac{1}{2} \left[\frac{\partial \mathbf{G}_u}{\partial \mathbf{q}} \mathbf{B}_{nlu} + \frac{\partial \mathbf{G}_v}{\partial \mathbf{q}} \mathbf{B}_{nlv} + \frac{\partial \mathbf{G}_w}{\partial \mathbf{q}} \mathbf{B}_{nlw} \right] \mathbf{q} dA - \\
& \iint_A \mathbf{B}_b^T \left[\int_{-h/2}^{h/2} z \bar{\mathbf{Q}} dz \right] \frac{1}{2} [\mathbf{G}_u \mathbf{B}_{nlu} + \mathbf{G}_v \mathbf{B}_{nlv} + \mathbf{G}_w \mathbf{B}_{nlw}] dA - \\
& \iint_A \mathbf{B}_b^T \left[\int_{-h/2}^{h/2} \bar{\mathbf{Q}} dz \right] \frac{1}{2} \left[\frac{\partial \mathbf{G}_u}{\partial \mathbf{q}} \mathbf{B}_{nlu} + \frac{\partial \mathbf{G}_v}{\partial \mathbf{q}} \mathbf{B}_{nlv} + \frac{\partial \mathbf{G}_w}{\partial \mathbf{q}} \mathbf{B}_{nlw} \right] \mathbf{q} dA + \\
& \iint_A [\mathbf{G}_u \mathbf{B}_{nlu} + \mathbf{G}_v \mathbf{B}_{nlv} + \mathbf{G}_w \mathbf{B}_{nlw}]^T \left[\int_{-h/2}^{h/2} \bar{\mathbf{Q}} dz \right] \mathbf{B}_m dA - \\
& \iint_A [\mathbf{G}_u \mathbf{B}_{nlu} + \mathbf{G}_v \mathbf{B}_{nlv} + \mathbf{G}_w \mathbf{B}_{nlw}]^T \left[\int_{-h/2}^{h/2} z \bar{\mathbf{Q}} dz \right] \mathbf{B}_b dA + \\
& \iint_A [\mathbf{G}_u \mathbf{B}_{nlu} + \mathbf{G}_v \mathbf{B}_{nlv} + \mathbf{G}_w \mathbf{B}_{nlw}]^T \left[\int_{-h/2}^{h/2} \bar{\mathbf{Q}} dz \right] \\
& \frac{1}{2} [\mathbf{G}_u \mathbf{B}_{nlu} + \mathbf{G}_v \mathbf{B}_{nlv} + \mathbf{G}_w \mathbf{B}_{nlw}] dA + \\
& \iint_A [\mathbf{G}_u \mathbf{B}_{nlu} + \mathbf{G}_v \mathbf{B}_{nlv} + \mathbf{G}_w \mathbf{B}_{nlw}]^T \left[\int_{-h/2}^{h/2} \bar{\mathbf{Q}} dz \right] \frac{1}{2} \left[\frac{\partial \mathbf{G}_u}{\partial \mathbf{q}} \mathbf{B}_{nlu} + \right. \\
& \left. \frac{\partial \mathbf{G}_v}{\partial \mathbf{q}} \mathbf{B}_{nlv} + \frac{\partial \mathbf{G}_w}{\partial \mathbf{q}} \mathbf{B}_{nlw} \right] \mathbf{q} dA
\end{aligned} \tag{2.44}$$

2.8 Transformation to the global coordinate system

In the first-order shear deformation theory developed, five DOFs $u^0, v^0, w^0, \theta_x^0, \theta_y^0$ were defined at each nodal point. By transforming the components to global Cartesian coordinate system the projections of the displacements and rotations are calculated. Hence, a new rotational DOF is produced in z direction which is known by $\theta_{z_g}^0$. Therefore, the global nodal DOF would be in the order $u_g^0, v_g^0, w_g^0, \theta_{x_g}^0, \theta_{y_g}^0, \theta_{z_g}^0$. In plate structures the rotational DOF in z direction is neglected because all elements are located in the same plane. Therefore, no component of stiffness is produced for the aforementioned DOF and no force is carried in this direction accordingly.

Referring to figure 2.2, the transformation of nodal DOFs and forces is defined as

follows

$$\begin{Bmatrix} u^0 \\ v^0 \\ w^0 \\ \theta_x^0 \\ \theta_y^0 \end{Bmatrix} = \mathbf{T} \begin{Bmatrix} u_g^0 \\ v_g^0 \\ w_g^0 \\ \theta_{x_g}^0 \\ \theta_{y_g}^0 \\ \theta_{z_g}^0 \end{Bmatrix} \quad \text{and} \quad \begin{Bmatrix} f_x \\ f_y \\ f_z \\ m_x \\ m_y \end{Bmatrix} = \mathbf{T} \begin{Bmatrix} f_{x_g} \\ f_{y_g} \\ f_{z_g} \\ m_{x_g} \\ m_{y_g} \\ m_{z_g} \end{Bmatrix} \quad (2.45)$$

where \mathbf{T} is the transformation matrix. It is noted that in the context of the Total Lagrangian (TL) formulation, the transformation matrix is calculated in the reference configuration of the structure and it has the following reduced form for each nodal point

$$\mathbf{T} = \begin{bmatrix} \cos(x, X) & \cos(x, Y) & \cos(x, Z) & 0 & 0 & 0 \\ \cos(y, X) & \cos(y, Y) & \cos(y, Z) & 0 & 0 & 0 \\ \cos(z, X) & \cos(z, Y) & \cos(z, Z) & 0 & 0 & 0 \\ 0 & 0 & 0 & \cos(x, X) & \cos(x, Y) & \cos(x, Z) \\ 0 & 0 & 0 & \cos(y, X) & \cos(y, Y) & \cos(y, Z) \end{bmatrix} \quad (2.46)$$

where x , y , and z are the coordinate of the origin of the local coordinate system. A further modification is required to include the rotational DOF in z direction to the transformation matrix \mathbf{T} . Thus, the new transformation matrix is defined as

$$\mathbf{T} = \begin{bmatrix} \cos(x, X) & \cos(x, Y) & \cos(x, Z) & 0 & 0 & 0 \\ \cos(y, X) & \cos(y, Y) & \cos(y, Z) & 0 & 0 & 0 \\ \cos(z, X) & \cos(z, Y) & \cos(z, Z) & 0 & 0 & 0 \\ 0 & 0 & 0 & \cos(x, X) & \cos(x, Y) & \cos(x, Z) \\ 0 & 0 & 0 & \cos(y, X) & \cos(y, Y) & \cos(y, Z) \\ 0 & 0 & 0 & \cos(z, X) & \cos(z, Y) & \cos(z, Z) \end{bmatrix} \quad (2.47)$$

The mentioned modification is required in case the drilling DOF is incorporated to the formulation of co-planar elements. In this case, the transformation of rotational components in z direction should be calculated. The new transformation matrix of equation 2.47 has the orthogonal property. Therefore, the following equation holds

$$\mathbf{T}^T \mathbf{T} = \mathbf{I} \quad (2.48)$$

There are several approaches to find the transformation matrix. In all of these methods the location of nodes in the global coordinate system is used to find the transformation matrix. Figure 2.5 shows one flat-shell element with the local and global coordinate systems.

The nodes of each element are labelled in a counter-clockwise direction (i - j - k - m). This pattern must be followed at each element to obtain the correct rotations in the

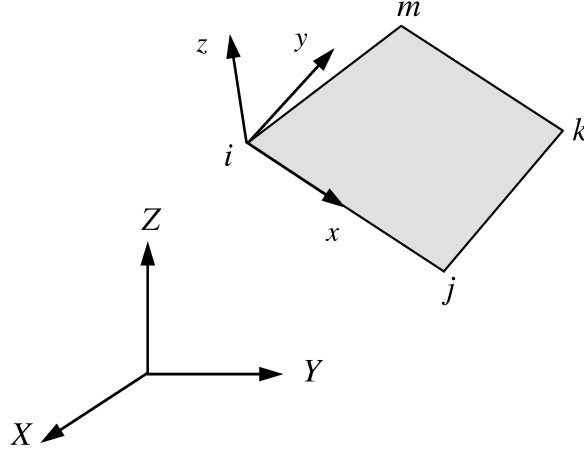


Figure 2.5: An element in the local and global coordinate system.

global coordinate system. Four transformation matrices are assigned concerning the nodes of four-node element. Since each particular element is in a plane configuration, the nodal transformation matrix is equal for each particular element. Referring to figure 2.5, node i is selected. Thus, one can compute the components of the transformation matrix through the following formulation.

The vectors along the sides of element is calculated by

$$\mathbf{V}_{ij} = \begin{Bmatrix} X_j - X_i \\ Y_j - Y_i \\ Z_j - Z_i \end{Bmatrix} \quad \text{and} \quad \mathbf{V}_{im} = \begin{Bmatrix} X_m - X_i \\ Y_m - Y_i \\ Z_m - Z_i \end{Bmatrix} \quad (2.49)$$

By assuming that the x axis of the local coordinate system is aligned along the side i - j , the corresponding unit vector can be computed as

$$\mathbf{v}_x = \frac{\mathbf{V}_{ij}}{\sqrt{X_{ij}^2 + Y_{ij}^2 + Z_{ij}^2}} \quad (2.50)$$

and the normal vector to the nodal point i is obtained by

$$\mathbf{V}_z = \mathbf{V}_{ij} \times \mathbf{V}_{im} \quad \text{and the corresponding unit vector:} \quad \mathbf{v}_z = \frac{\mathbf{V}_z}{|\mathbf{V}_{ij} \times \mathbf{V}_{im}|} \quad (2.51)$$

Next, the unit vector in y direction is simply calculated using the cross product as

$$\mathbf{v}_y = \mathbf{v}_z \times \mathbf{v}_x \quad (2.52)$$

The unit vectors achieved in equations 2.50 - 2.52 represent the direction cosines of the local coordinate system with respect to the global coordinate system. In other words, they are expressed as

$$\mathbf{v}_x = \begin{Bmatrix} \cos(x, X) \\ \cos(x, Y) \\ \cos(x, Z) \end{Bmatrix}, \quad \mathbf{v}_y = \begin{Bmatrix} \cos(y, X) \\ \cos(y, Y) \\ \cos(y, Z) \end{Bmatrix}, \quad \mathbf{v}_z = \begin{Bmatrix} \cos(z, X) \\ \cos(z, Y) \\ \cos(z, Z) \end{Bmatrix} \quad (2.53)$$

The same procedure is used for the remaining nodes. Since the element is flat, the same transformation matrix should be achieved at the nodal points of each particular element. Thus, the element transformation matrix is presented as

$$\mathbf{T}^{(e)} = \begin{bmatrix} \mathbf{T}_1 & & & \\ & \mathbf{T}_2 & & \\ & & \mathbf{T}_3 & \\ & & & \mathbf{T}_4 \end{bmatrix} \quad (2.54)$$

where \mathbf{T}_i ($i=1$ to 4) is the transformation matrix calculated for node i .

By transforming the local displacement and force vectors into the global coordinate system through the equation 2.45 and taking into account the orthogonal property of the transformation matrix (equation 2.48), the stiffness matrix in the global coordinate system is rearranged into the following form

$$\mathbf{K}_{T,g} = \mathbf{T}^T \mathbf{K}_T \mathbf{T} \quad (2.55)$$

where $\mathbf{K}_{T,g}$ is the global tangent stiffness matrix whereas \mathbf{K}_T is the tangent stiffness matrix in local coordinate system. It is mentioned that no transformation is needed for the nodal loads. Thus, they are applied directly to the global system of equations. In the context of the finite element analysis, the non-dimensional local element coordinates ξ and η are used. Therefore, one further transformation of the equation 2.55 is performed from the natural to local axes using the Jacobian matrix. By assuming x_0 as the origin of the local coordinate system and \mathbf{T}_{trans} as the part of the transformation matrix presented in equation 2.46 which contributes to the translations, the following equation holds to relate the location of the local and global coordinates.

$$\begin{Bmatrix} x \\ y \\ z \end{Bmatrix} = \mathbf{T}_{trans} \left(\begin{Bmatrix} X \\ Y \\ Z \end{Bmatrix} - \begin{Bmatrix} X_0 \\ Y_0 \\ Z_0 \end{Bmatrix} \right) \quad (2.56)$$

where (X_0, Y_0, Z_0) is the origin of the local coordinate system with respect to the origin of the global coordinate system. The equation 2.56 is established at each nodal point. The Jacobian matrix in the local coordinate system is presented as follows

$$\mathbf{J}_l = \begin{bmatrix} \frac{\partial x}{\partial \xi} & \frac{\partial x}{\partial \eta} \\ \frac{\partial y}{\partial \xi} & \frac{\partial y}{\partial \eta} \end{bmatrix} \quad (2.57)$$

Substituting equation 2.56 into equation 2.57, one can arrive at the following Jacobian matrix in the global coordinate system as

$$\mathbf{J}_g = \mathbf{T}_{trans} \begin{bmatrix} \frac{\partial X}{\partial \xi} & \frac{\partial X}{\partial \eta} \\ \frac{\partial Y}{\partial \xi} & \frac{\partial Y}{\partial \eta} \end{bmatrix} \quad (2.58)$$

Based on equation 2.58, the origin of the global coordinate system (X_0, Y_0, Z_0) does not contribute to the transformation procedure. Therefore, it is not of importance in the finite element analysis.

It is noticed that the stress calculations are performed in the local coordinate system. This is necessary when strength analysis of the structure is of concern. Once the global displacements are calculated, the transformation to the local coordinate system (using equation 2.45) is required. The local stresses are particularly used for engineering purposes.

2.9 Technique for avoiding singularity

A singularity is encountered in the assembly of the stiffness matrix in the global coordinate system. It arises when one nodal point is shared with several co-planar elements and the projection of the coordinate system has no component in the transformation matrix. Consequently, no stiffness is related to the degree of freedom $\theta_{z_g}^0$. The aforementioned problem becomes more critical when a load in z direction is applied to the node concerned. Subsequently, the force component f_{z_g} appears whereas no corresponding stiffness component is available in $K_{\theta_{z_g}^0}$. There exist several methods to avoid this singularity. The main traditional approaches are:

- (a) To constrain the sixth DOF $\theta_{z_g}^0$ for the co-planar elements. Therefore, the corresponding equations are deleted and the transformation of the bending moment is neglected.
- (b) To assign a fictitious stiffness matrix component $K_{\theta_z^0}$ for the co-planar elements. Therefore, the singularity is conquered since six unknown DOFs are achieved through solving six equations.
- (c) To transform the local rotational DOFs into a new order of $u, v, w, \theta_1, \theta_2$ in which θ_1, θ_2 represent the rotational DOFs in the principal direction. In this approach, basically, the average of the unit normal vector of a particular node surrounded by quasi co-planar elements is calculated. Accordingly, the new principal in-plane rotations are computed.
- (d) To add a drilling DOF by modifying the membrane formulation. There are many proposals and ongoing researches to include the drilling DOF based on the mentioned idea, eg. in (Allman, 1984; Cook, 1994; Hughes and Brezzi, 1989; Ibrahimbegovic et al., 1990).

In most of the mentioned approaches, one should account the location where the co-planarity is encountered. This can be detected by calculating the relative differences of the normal vectors of one specific node with respect to the nodes in neighbours. If less than relative 5 degree is detected, that particular node is located in a co-planar surface. The possibility of detecting co-planar elements is increased when finer mesh is generated.

Herein, methods (b) and (d) are implemented. They are discussed in detail in the following.

Fictitious stiffness

The fictitious stiffness can be considered for all elements. The order of magnitude of the fictitious stiffness was mentioned of $EtA(e)$ value for each element of the isotropic shells (where E is the Young's modulus, t is the thickness of shell, and $A^{(e)}$ is the area of element) (Zienkiewicz and Taylor, 2000). However, this value causes very stiff shells in case composite materials are investigated, especially when they are subjected to out of plane load. Therefore, smaller value in the order of $K_{\theta_z} = E_L t A^{(e)} / 1000$ (where E_L is the Young's modulus in 1-direction, t is the total thickness of laminate, and $A^{(e)}$ is the area of element) is proposed. Since the fictitious stiffness is added before the transformation procedure, one can consider it in advance for all elements to conquer any singularity which might encounters.

The fictitious stiffness can be applied successfully for the linear and non-linear analysis of shell. In case of non-linear analysis one should handle a proper value for the drilling stiffness that matches well in the global system of equations at each Newton-Raphson's iteration. Therefore, in order to find a proper value at each iteration, one can multiply the maximum value of the diagonal stiffnesses by a factor of 10^{-3} to 10^{-5} to this artificial stiffness. By doing so, numerical problems or ill-conditioned equations within the non-linear solution are reduced. It is again mentioned that this fictitious stiffness is applied to conquer the singularity problem and has no effect on the strain and stress calculation of shell elements.

Drilling degree of freedom

In this method, rotational stiffness coefficients are related to the membrane stiffnesses in such a manner the overall equilibrium equation is not disturbed. Therefore, the drilling potential energy containing a penalty parameter is defined as

$$\Pi_{drilling} = \frac{1}{2} \int_{\Omega} P (\omega - \theta_{z_g}^0)^2 d\Omega \quad (2.59)$$

where P is the penalty parameter, $\theta_{z_g}^0$ is the drilling DOF, and ω is the in-plane rotation of shell that is related to the membrane DOFs as

$$\omega = \frac{1}{2} \left(\frac{\partial v^0}{\partial x} - \frac{\partial u^0}{\partial y} \right) \quad (2.60)$$

The penalty parameter value can be chosen as $P = 10^{-4} E_1 t$ and can be applied for all elements whether they are co-planar or not.

It is of importance to overcome the singularity by the mentioned methods in the local Cartesian coordinate system. Therefore, the drilling stiffness coefficients are added accordingly to the local stiffness matrix before the transformation into the global coordinate system.

2.10 Warping function for flat-shell

Since the geometry of shell is approximated by flat elements, warped elements can be generated in a way that the four nodes are not located in the same plane. Therefore,

the associated stiffness should be modified before transforming to the global coordinate system (Wisniewski, 2010; Taylor, 1987). A warped four-node element is shown in figure 2.6.

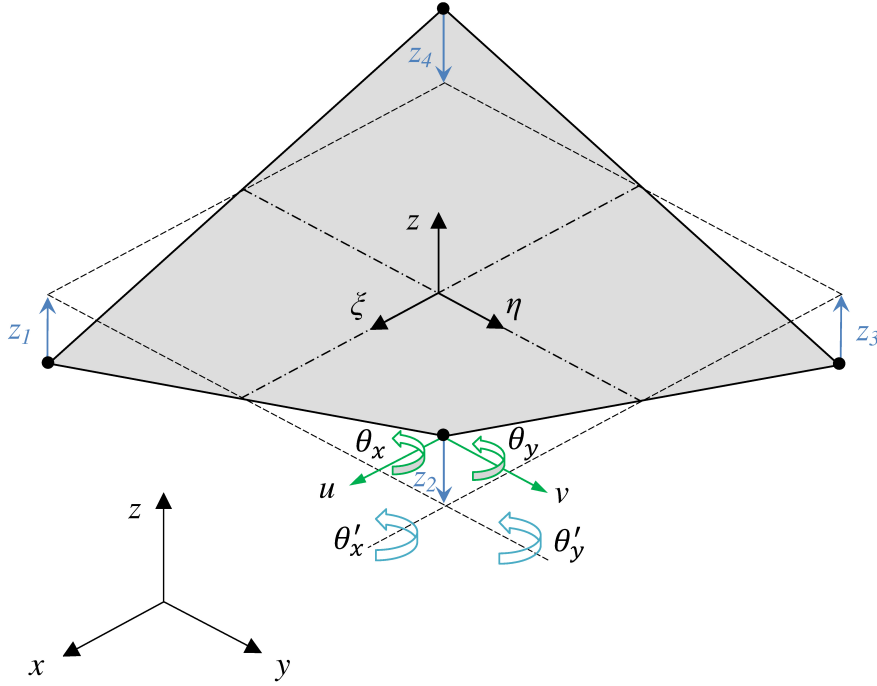


Figure 2.6: The projection of warped geometry.

The modification can be applied by either correcting the rotation or displacement field. Therefore, the nodes that are located in warped plane are connected to the unwarped ones by rigid links. By doing so, the rotation of the warped nodes in the local coordinate system θ_x^0 and θ_y^0 are modified to $\theta_x^{0'}$ and $\theta_y^{0'}$ as follows

$$\begin{aligned}\theta_x^{0'} &= \theta_x^0 + Zv^0 \\ \theta_y^{0'} &= \theta_y^0 - Zu^0\end{aligned}\tag{2.61}$$

where Z is the offset from average plane at any particular node. Due to the equation 2.61 the corrected rotations depends on the rotations of nodes in local coordinate system and the multiplication of in-plane displacement and the offset Z .

The warping modification can be used for all elements; for those are warped the offset is activated to adjust the warping rotations. The warping matrix for each particular

node is defined as

$$\begin{pmatrix} u^0 \\ v^0 \\ w^0 \\ \theta_x^{0'} \\ \theta_y^{0'} \\ \theta_z^0 \end{pmatrix} = \mathbf{W} \begin{pmatrix} u^0 \\ v^0 \\ w^0 \\ \theta_x^0 \\ \theta_y^0 \\ \theta_z^0 \end{pmatrix} = \begin{bmatrix} 1 & 0 & 0 & 0 & 0 & 0 \\ 0 & 1 & 0 & 0 & 0 & 0 \\ 0 & 0 & 1 & 0 & 0 & 0 \\ 0 & Z & 0 & 1 & 0 & 0 \\ -Z & 0 & 0 & 0 & 1 & 0 \\ 0 & 0 & 0 & 0 & 0 & 1 \end{bmatrix} \begin{pmatrix} u^0 \\ v^0 \\ w^0 \\ \theta_x^0 \\ \theta_y^0 \\ \theta_z^0 \end{pmatrix} \quad (2.62)$$

The warping matrix \mathbf{W} is applied to the tangent stiffness matrix in the local coordinate system. Then, the transformation to the global coordinate system is performed. The corrected tangent stiffness matrix in warped elements is written as

$$\mathbf{K}_{T,w} = \mathbf{W}\mathbf{K}_T\mathbf{W}^T \quad (2.63)$$

where \mathbf{K}_T and $\mathbf{K}_{T,w}$ are the local tangent stiffness matrix before and after the correction. It is noted that the tangent stiffness matrix in warped elements should be corrected before transforming it to the global coordinate system

2.11 Numerical tests

Verification studies are performed to demonstrate the applicability and the performance of the method developed in the previous sections. The efficiency of the flat-shell formulation in geometrically non-linear regime is illustrated. First, a cylindrical shell with three layers with cross-ply lay-ups $[0^\circ/90^\circ/0^\circ]$ and $[90^\circ/0^\circ/90^\circ]$ is analysed. The 0° angle denotes fibres in the longitudinal direction of the shell. The shell is modelled with two different thicknesses $h_1=12.7$ and $h_2=6.35$. It is subjected to a point loading at the centre. Only one quarter of the shell is modelled because of symmetry in geometry and boundary conditions. A schematic view of the studied shell is depicted in figure 2.7.

The geometrical dimensions and the material properties of the hinged cylinder are listed in table 2.1.

Table 2.1: Geometrical dimensions and material properties of the hinged cylinder.

L	R	ϕ	Type	E_1	E_2	$G_{12}=G_{13}=G_{23}$	ν_{12}
508	2540	0.1	Composite	3300	1100	660	0.25
			Isotropic	3102.75	3102.75	1193.37	0.3

This cylindrical shell problem is considered as a classical benchmark test for analysing shell structures in moderate rotations. Due to the hinged boundary conditions and the type of loading applied, the test is prone to snap-back and snap-through instabilities. Thus, the arc-length method has to be applied to follow the solution path. The mesh consists of ten by ten elements. The load-displacement diagram of

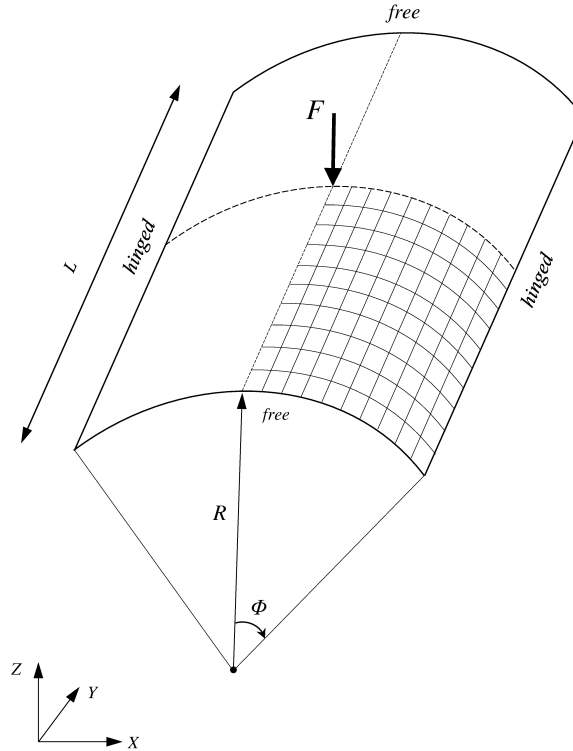


Figure 2.7: Schematic view of the hinged cylindrical shell.

the shell with the thickness of $h_1=12.7$ is compared with Sze et al. (2004) in figure 2.8. The results of shells with the same geometry but isotropic material properties are also provided in figure 2.8. As it is shown in figure 2.8, the flat shell element formulation compares well with the ones of Sze et al. (2004).

Next, the same study is carried out for isotropic and composite shells with the thickness $h_2=6.35$. The load-displacement diagram of the shell at the loading point is reported in figure 2.9.

As it is shown in figure 2.8 and 2.9, the results agree very well with the ones reported by Sze et al. (2004). In this benchmark problem the thin shell demonstrates a more complex response in the same loading condition. Such a response can only be traced by the arc-length method.

In the next study, a cylindrical isotropic shell is subjected to a uniform pressure. The schematic view of the studied shell is depicted in figure 2.10. Only one quarter of the shell is modelled because of the symmetry. The material properties and geometrical dimensions of the shell are presented in table 2.2.

Table 2.2: Geometrical dimensions and material properties of clamped cylinder.

L (m)	R (m)	ϕ (rad)	h (m)	E (Pa)	ν
20	100	0.1	0.125	450000	0.3

The distributed load is applied manually through nodal point loads. The load-

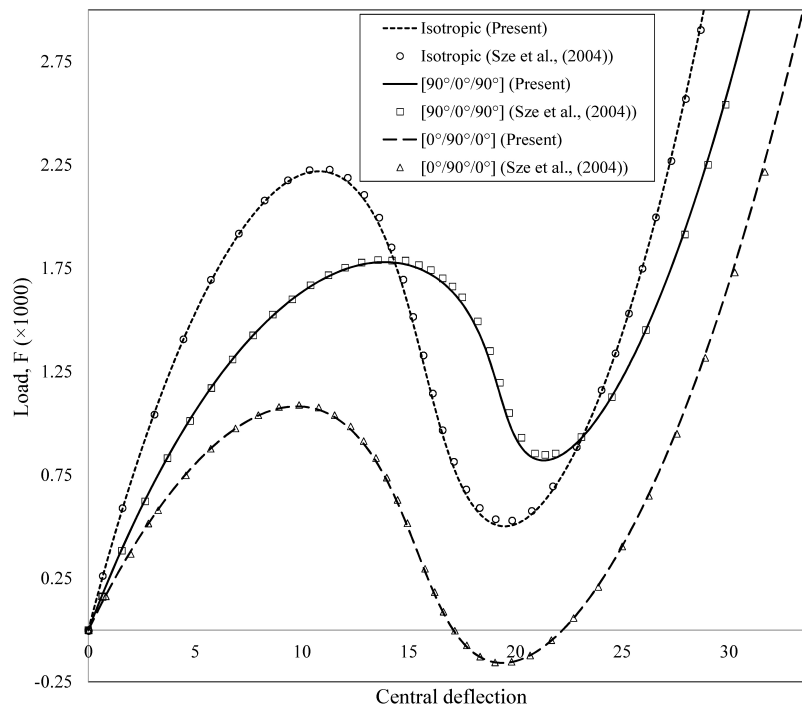


Figure 2.8: Load-deflection response of the cylindrical shell with thickness $h_1=12.7$.

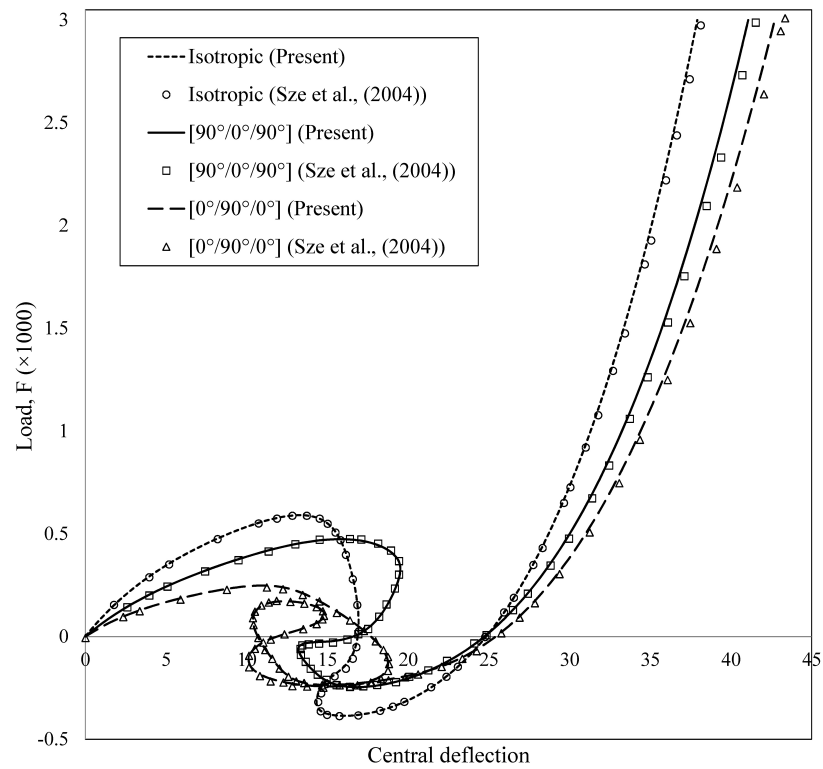


Figure 2.9: Load-deflection response of the cylindrical shell with thickness $h_2=6.35$.

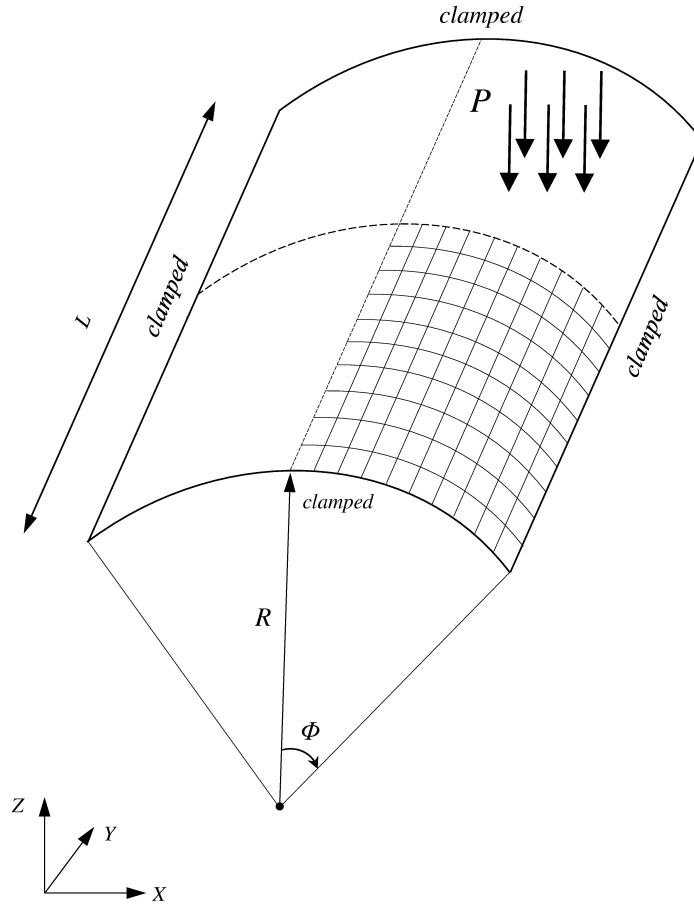


Figure 2.10: Schematic view of the clamped cylindrical shell.

displacement diagram of the shell at the point of the intersection of symmetry lines is plotted in figure 2.11.

A very good agreement is achieved in comparison to the one reported by Reddy (2014). This example can be followed by force control algorithm. In order to check the order of convergence of flat-shell formulation in the Newton-Raphson algorithm, the norm of force and moment of the current example at the loading amplitudes $P=0.135$ N and $P=0.18$ N are provided in table 2.3. The convergence orders are calculated by

Table 2.3: Order of convergence in Newton-Raphson iteration.

f_{ext}	Force convergence	Moment convergence	Maximum DOF increment	χ
0.135	3.22	0.6674×10^{-12}	-0.3866×10^{-1}	-
0.135	0.2213	0.1813×10^{-2}	-0.1042×10^{-1}	-
0.135	0.2210×10^{-2}	0.1793×10^{-3}	-0.8632×10^{-3}	1.899837
0.18	5.725	0.8380×10^{-12}	-0.5154×10^{-1}	-
0.18	1.064	0.5373×10^{-2}	-0.2221×10^{-1}	-
0.18	0.8482×10^{-1}	0.1288×10^{-2}	-0.5300×10^{-2}	1.702078
0.18	0.4097×10^{-3}	0.4418×10^{-3}	-0.3369×10^{-3}	1.923232

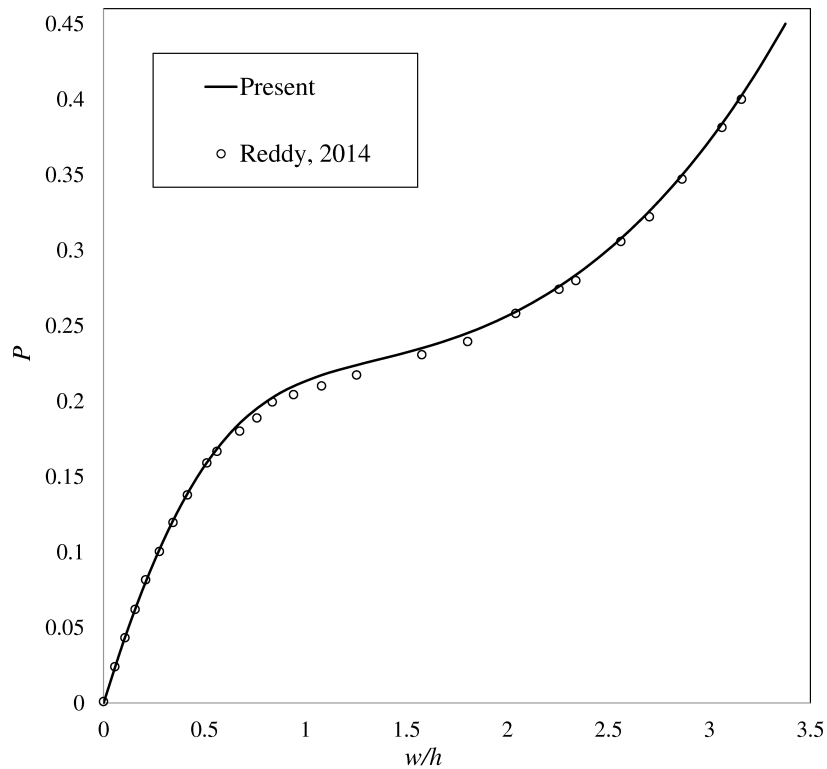


Figure 2.11: Load-deflection response of the cylindrical shell under distributed load.

the values of maximum DOF increment and they are very close to a quadratic order in Newton-Raphson method.

2.12 Closing remarks

In this chapter a flat-shell formulation was developed. The proposed formulation can be effectively used to simulate the response of composite shells and plates in large deflections but moderate rotations. It is emphasized that the developed theory is simple and robust for geometrically non-linear applications. Although the response of the region with delamination can be simulated by the present formulation using the double node technique, the implementation of XFEM is of interest. Thus, one can avoid simulating the discontinuous subdomains through independent laminates and the discontinuity can be activated in the formulation of elements. In the next chapter, the proposed formulation is enhanced for the delamination analysis of shells.

Chapter 3

Extension of the shell element for delamination analysis

3.1 Introduction

The theory of the eXtended Finite Element Method (XFEM) was firstly proposed by Belytschko and Black (1999) to model the crack propagation. This theory is established on the property of partition of unity of the shape functions. Taking this into account, one can effectively add extra DOFs and a proper discontinuity function to predict the crack propagation in any particular element. Therefore, no remeshing is required to align the elements with the crack path. The original scheme was improved by Dolbow and Belytschko (1999), who implemented a jump enrichment function for already cracked elements. Nevertheless, crack tip enrichments that are derived from the analytical solution of crack tip can also be included as extra DOFs. Later, the XFEM approach was combined by the level set method to efficiently activate the enrichments at where the discontinuity exists. For instance, Sukumar et al. (2001) applied the level set and XFEM to model holes and inclusions. There exist a few references in that XFEM is used for plates or shells. Areias and Belytschko (2005) used XFEM and the cohesive zone model to simulate the in-plane crack in shells. For the delamination analysis, the formulation should be enriched in such a way that the discontinuity is imposed through the thickness of the laminate rather than in plane. For instance, it has been applied for shell structures through solid-like shell elements by Remmers et al. (2003); Remmers and de Borst (2004). Van der Meer et al. (2012) implemented the XFEM to model the delamination and its propagation for membrane structures. Nagashima and Suemasu (2010) simulated the linear buckling response of the discontinuous composite shells by using the XFEM formulation and the isoparametric shell element. Sosa and Karapurath (2012) adopted both the jump enrichment function and the orthotropic crack tip functions of composites to analyse the delamination in fibre metal laminates. Brouzoulis and Fagerström (2015) analysed shells with multiple delaminations using the XFEM. Thus, several enhanced DOFs are dynamically added to simulate the discontinuous interfaces which lead to a three-dimensional theory, similar to the layerwise formulation.

In the standard finite element method, the displacement field is approximated as follows

$$\mathbf{u} = \sum_{i=1}^n N_i u_i \quad (3.1)$$

where \mathbf{u} is the displacement field which is continuous, N_i and u_i are the shape functions and displacement values of node i , respectively. In order to pose a discontinuity using the XFEM topology, the displacement field is modified as follows

$$\mathbf{u} = \sum_{i \in I} N_i u_i + \sum_{j \in J} H(f(\mathbf{x})) N_j a_{u_j} + \sum_{k \in K} N_k \sum_{l=1}^4 F_l(r, \theta) c_{u_k}^l \quad (3.2)$$

The first additional term includes a strong discontinuity function H and additional DOFs a_{u_j} to simulate the response of the discontinued location. The discontinuity function can be defined as

$$H(x) = \begin{cases} +1 & \text{if } x \geq 0 \\ -1 & \text{if } x < 0 \end{cases} \quad (3.3)$$

The value of this function can be determined through the signed distance function $f(\mathbf{x})$ to the crack. In other words, the sign determines whether x is on one side or other side of the crack. The second additional term in equation 3.2 involves the crack tip functions $F_l(r, \theta)$ to model the displacement field around the tip of the discontinuity using additional DOFs $c_{u_k}^l$. These functions are derived from analytical solution of displacement field at the crack tip in linear elastic fracture mechanics. For linear elastic materials they are written as

$$\{F_l(r, \theta)\} = \left\{ \sqrt{r} \sin\left(\frac{\theta}{2}\right), \sqrt{r} \cos\left(\frac{\theta}{2}\right), \sqrt{r} \sin\left(\frac{\theta}{2}\right) \sin(\theta), \sqrt{r} \cos\left(\frac{\theta}{2}\right) \sin(\theta) \right\} \quad (3.4)$$

where (r, θ) are the local polar coordinates at the crack tip.

Three set of nodes are distinguished in equation 3.2:

- I is the set of all nodes in the mesh,
- J represents the set of nodes that intersect the crack but does not cover crack tips and
- K is the set of nodes that cover a crack tip.

The schematic view of a plate containing an in-plane discontinuity is depicted in figure 3.1.

In the present formulation the crack tip functions are avoided and the delamination is inherently embedded to the required region. In the delamination analysis, the discontinuity is defined in the thickness direction. Therefore, the discontinuity function is a function of z .

In the following sections, the formulation of a discontinuous shell element using the XFEM is developed to predict the structural behaviour of delaminated composite shells.

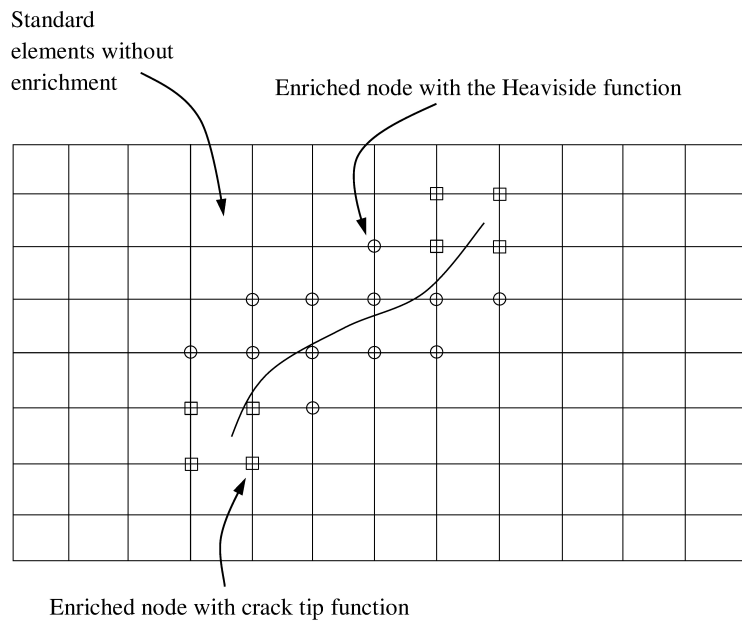


Figure 3.1: Schematic view of discontinuity on a structured mesh.

3.2 Kinematics of shell in XFEM topology

In this section the flat-shell formulation that was developed in section 2.2.1 is enriched. The studied domain in the local coordinate system is divided into three distinct zones: the discontinued laminate in that the first-order shear deformation theory is applied with the XFEM technique (zones Ω^- and Ω^+); and the interface region (zone Ω^d) that is discussed in details in chapter 4. This methodology allows us to obtain the relative motions of the interface while a two-dimensional state formulation like the first-order shear deformation theory is used. The schematic view of the plate with the distinct regions is shown in figure 3.2.

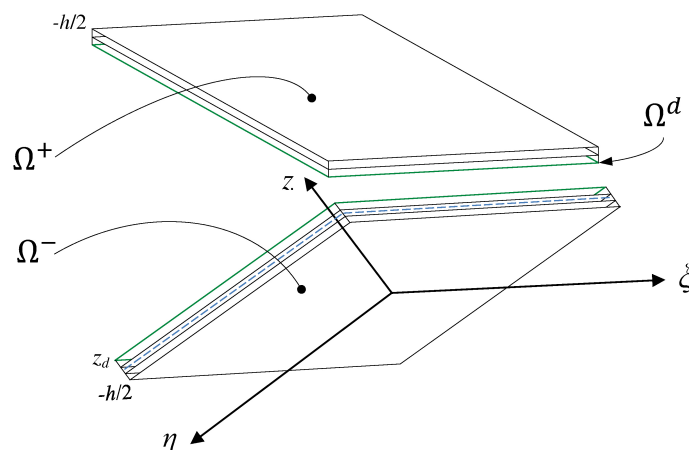


Figure 3.2: Schematic view of a discontinuous multi-layered element.

In figure 3.2, the green lines indicate the discontinuous region and z_d represents the location of the discontinuity in z direction with respect to the local coordinate system located at the centre of the element. Here, the Heaviside step function is utilized to express a displacement field that is discontinuous through-the-thickness of the laminate. By this, the first-order shear deformation theory is enhanced through adding extra DOFs in the context of the XFEM topology.

3.2.1 Displacement field

The adopted displacement components in the local coordinate system are presented as

$$\begin{aligned}
 U(x, y, z) &= u^0(x, y) + \bar{H}(z_d) a_u^0(x, y) + z \left(\theta_y^0(x, y) + \bar{H}(z_d) a_{\theta_y}^0(x, y) \right) \\
 V(x, y, z) &= v^0(x, y) + \bar{H}(z_d) a_v^0(x, y) - z \left(\theta_x^0(x, y) + \bar{H}(z_d) a_{\theta_x}^0(x, y) \right) \\
 W(x, y, z) &= w^0(x, y) + \bar{H}(z_d) a_w^0(x, y)
 \end{aligned} \tag{3.5}$$

Here U , V , and W denote the displacements in x , y , and z directions, respectively; u^0 , v^0 , and w^0 present the regular displacement values of mid-plane whereas a_u^0 , a_v^0 , and a_w^0 are the enhanced displacement values of mid-plane; the regular and enhanced rotations of mid-plane are provided by θ_x^0 , θ_y^0 , and $a_{\theta_x}^0$, $a_{\theta_y}^0$, respectively. $\bar{H}(z_d)$ is the Heaviside step function; and z_d is the location of discontinuity through the thickness of laminate. The schematic view of a multi-layered plate with regular and enhanced displacements and rotations is shown in figure 3.3.

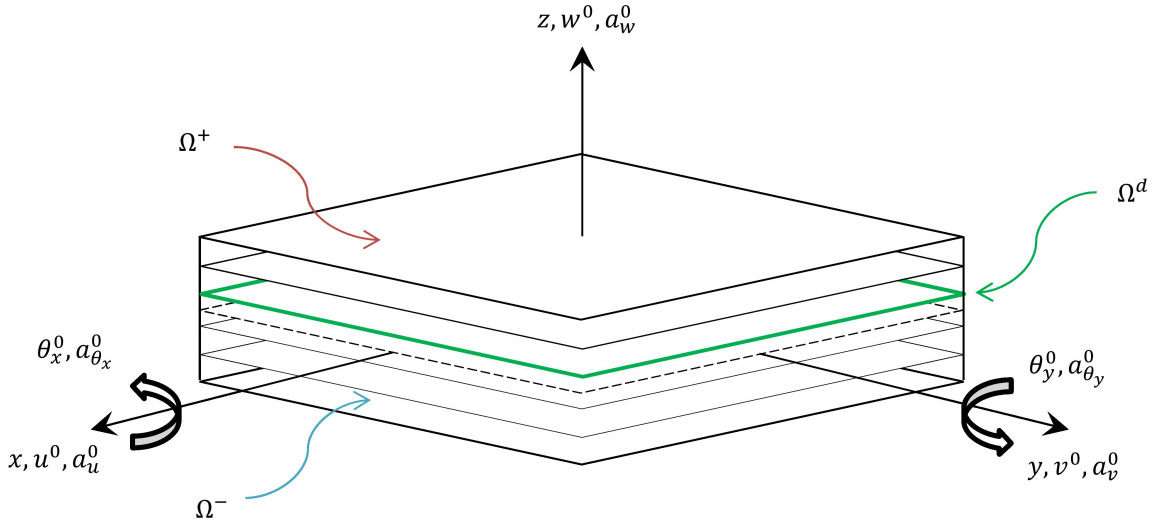


Figure 3.3: Schematic view of a multi-layered plate with regular and enhanced displacements and rotations.

Depending on the value of the Heaviside function, being zero or one, the displacement field can be represented either in a continuous or discontinuous format. In both

cases, the displacement field is measured with respect to the mid-plane of the laminate. In the continuous variation of displacement field the enhanced displacements and rotations are excluded and the remaining formulation with regular variables is applied to the part of laminate that is intact. Nevertheless, once a discontinuity has been detected the discontinuous displacement field has to be utilized. In the discontinuous displacement field, the Heaviside function assumes the value one, and consequently, the enhanced displacements and rotations are superimposed. Therefore, it is defined as

$$\bar{H}(z_d) = H(z - z_d) = \begin{cases} 0 & \text{if } z < z_d \\ 1 & \text{if } z \geq z_d \end{cases} \quad (3.6)$$

Same as the finite element formulation in chapter 2, four-node quadrilateral elements are used to discretise the domain. However, here the interpolation is performed for the standard and the enhanced DOFs. The standard and enhanced displacements and rotations are interpolated by bilinear shape functions as

$$\begin{pmatrix} u^0 \\ v^0 \\ w^0 \\ \theta_x^0 \\ \theta_y^0 \\ a_u^0 \\ a_v^0 \\ a_w^0 \\ a_{\theta_x}^0 \\ a_{\theta_y}^0 \end{pmatrix} = \sum_{i=1}^4 \begin{pmatrix} N_i u_i^0 \\ N_i v_i^0 \\ N_i w_i^0 \\ N_i \theta_{x_i}^0 \\ N_i \theta_{y_i}^0 \\ N_i a_{u_i}^0 \\ N_i a_{v_i}^0 \\ N_i a_{w_i}^0 \\ N_i a_{\theta_{x_i}}^0 \\ N_i a_{\theta_{y_i}}^0 \end{pmatrix} = \mathbf{N} \mathbf{q} \quad (3.7)$$

where \mathbf{N} is the matrix of shape functions and \mathbf{q} is the vector of unknown variables, including regular and enriched DOFs.

3.2.2 Strain field

By substituting the equation 3.5 in the general format into the Green strain tensor, the strain field $\boldsymbol{\varepsilon} = [\varepsilon_{xx} \ \varepsilon_{yy} \ \gamma_{xy} \ \gamma_{xz} \ \gamma_{yz}]^T$ is obtained as follows

$$\begin{pmatrix} \varepsilon_{xx} \\ \varepsilon_{yy} \\ \gamma_{xy} \end{pmatrix} = \begin{bmatrix} 1 & 0 & 0 & -z & 0 & 0 \\ 0 & 1 & 0 & 0 & -z & 0 \\ 0 & 0 & 1 & 0 & 0 & -z \end{bmatrix} \begin{pmatrix} \boldsymbol{\varepsilon}_m^0 + \boldsymbol{\varepsilon}_{nl} \\ \boldsymbol{\varepsilon}_b^0 \end{pmatrix} \quad (3.8)$$

$$\begin{pmatrix} \gamma_{xz} \\ \gamma_{yz} \end{pmatrix} = \begin{pmatrix} w_{,x}^0 + \theta_y^0 + \bar{H}(z_d) (a_{w,x}^0 + a_{\theta_y}^0) \\ w_{,y}^0 - \theta_x^0 + \bar{H}(z_d) (a_{w,y}^0 - a_{\theta_x}^0) \end{pmatrix}$$

where $\boldsymbol{\varepsilon}_m^0$, $\boldsymbol{\varepsilon}_b^0$, and $\boldsymbol{\varepsilon}_{nl}$ are respectively the membrane, bending, and non-linear strain term. The subscript comma denotes a partial differentiation with respect to the local Cartesian coordinate system, located at the centre of each element. These components are defined in the general format as

$$\boldsymbol{\varepsilon}_m^0 = \left\{ \begin{array}{c} u_{,x}^0 + \bar{H}(z_d) a_{u,x}^0 \\ v_{,y}^0 + \bar{H}(z_d) a_{v,y}^0 \\ u_{,y}^0 + v_{,x}^0 + \bar{H}(z_d) (a_{u,y}^0 + a_{v,x}^0) \end{array} \right\} \quad (3.9)$$

and

$$\boldsymbol{\varepsilon}_b^0 = \left\{ \begin{array}{c} -\theta_{y,x}^0 - \bar{H}(z_d) a_{\theta_{y,x}}^0 \\ \theta_{x,y}^0 + \bar{H}(z_d) a_{\theta_{x,y}}^0 \\ -\theta_{y,y}^0 + \theta_{x,x}^0 + \bar{H}(z_d) (-a_{\theta_{y,y}}^0 + a_{\theta_{x,x}}^0) \end{array} \right\} \quad (3.10)$$

and

$$\boldsymbol{\varepsilon}_{nl} = \left\{ \begin{array}{c} \frac{1}{2}(u_{,x}^0 + \bar{H}(z_d) a_{u,x}^0)^2 + \frac{1}{2}(v_{,x}^0 + \bar{H}(z_d) a_{v,x}^0)^2 + \frac{1}{2}(w_{,x}^0 + \bar{H}(z_d) a_{w,x}^0)^2 \\ \frac{1}{2}(u_{,y}^0 + \bar{H}(z_d) a_{u,y}^0)^2 + \frac{1}{2}(v_{,y}^0 + \bar{H}(z_d) a_{v,y}^0)^2 + \frac{1}{2}(w_{,y}^0 + \bar{H}(z_d) a_{w,y}^0)^2 \\ (u_{,x}^0 + \bar{H}(z_d) a_{u,x}^0)(u_{,y}^0 + \bar{H}(z_d) a_{u,y}^0) + (v_{,x}^0 + \bar{H}(z_d) a_{v,x}^0)(v_{,y}^0 + \bar{H}(z_d) a_{v,y}^0) + (w_{,x}^0 + \bar{H}(z_d) a_{w,x}^0)(w_{,y}^0 + \bar{H}(z_d) a_{w,y}^0) \end{array} \right\} \quad (3.11)$$

The non-linear components of the in-plane strain vector in equation 3.11 correspond to the non-linear response of the structure. Based on the different assumption for the in-plane and transverse displacements, the present formulation is appropriate for small strains, large deflections and moderate rotations (Fafard et al., 1989). Since the interlaminar failure plays a critical role in the response of laminated structures manufactured by composite materials, the adopted assumption is adequate when these materials are investigated.

The discretised strain components are derived by substituting the discretised displacement field of equation 3.7 into the corresponding components. They are provided in general format in the following.

a) Membrane strain:

$$\boldsymbol{\varepsilon}_m^0 = \sum_{i=1}^4 \mathbf{B}_{m_i} \mathbf{q} \quad (3.12)$$

where \mathbf{B}_{m_i} is the matrix of membrane strain. It is given by

$$\mathbf{B}_{m_i} = \begin{bmatrix} \frac{\partial N_i}{\partial x} & 0 & 0 & 0 & 0 & \frac{\partial N_i}{\partial x} & 0 & 0 & 0 & 0 \\ 0 & \frac{\partial N_i}{\partial y} & 0 & 0 & 0 & 0 & \frac{\partial N_i}{\partial y} & 0 & 0 & 0 \\ \frac{\partial N_i}{\partial y} & \frac{\partial N_i}{\partial x} & 0 & 0 & 0 & \frac{\partial N_i}{\partial y} & \frac{\partial N_i}{\partial x} & 0 & 0 & 0 \end{bmatrix} \quad (3.13)$$

b) Bending stain:

$$\boldsymbol{\varepsilon}_b^0 = \sum_{i=1}^4 \mathbf{B}_{b_i} \mathbf{q} \quad (3.14)$$

where \mathbf{B}_{b_i} is the matrix of bending strain. It is provided by

$$\mathbf{B}_{b_i} = \begin{bmatrix} 0 & 0 & 0 & 0 & -\frac{\partial N_i}{\partial x} & 0 & 0 & 0 & 0 & -\frac{\partial N_i}{\partial x} \\ 0 & 0 & 0 & \frac{\partial N_i}{\partial y} & 0 & 0 & 0 & 0 & \frac{\partial N_i}{\partial y} & 0 \\ 0 & 0 & 0 & \frac{\partial N_i}{\partial x} & -\frac{\partial N_i}{\partial y} & 0 & 0 & 0 & \frac{\partial N_i}{\partial x} & -\frac{\partial N_i}{\partial y} \end{bmatrix} \quad (3.15)$$

c) Shear stain:

$$\boldsymbol{\gamma} = \sum_{i=1}^4 \mathbf{B}_{s_i} \mathbf{q} \quad (3.16)$$

where \mathbf{B}_{s_i} is the shear strain matrix. It is written as

$$\mathbf{B}_{s_i} = \begin{bmatrix} 0 & 0 & \frac{\partial N_i}{\partial x} & 0 & N_i & 0 & 0 & \frac{\partial N_i}{\partial x} & 0 & N_i \\ 0 & 0 & \frac{\partial N_i}{\partial y} & -N_i & 0 & 0 & 0 & \frac{\partial N_i}{\partial y} & -N_i & 0 \end{bmatrix} \quad (3.17)$$

d) Non-linear stain:

$$\begin{aligned} \boldsymbol{\varepsilon}_{nl} = & \frac{1}{2} (\mathbf{G}_u + \mathbf{G}_{a_u}) \sum_{i=1}^4 \mathbf{B}_{nlu_i} \mathbf{q} + \frac{1}{2} (\mathbf{G}_v + \mathbf{G}_{a_v}) \sum_{i=1}^4 \mathbf{B}_{nlv_i} \mathbf{q} + \\ & \frac{1}{2} (\mathbf{G}_w + \mathbf{G}_{a_w}) \sum_{i=1}^4 \mathbf{B}_{nlw_i} \mathbf{q} \end{aligned} \quad (3.18)$$

where the above matrices are defined as

$$\begin{aligned} \mathbf{G}_u = \begin{bmatrix} u_{,x}^0 & 0 & 0 \\ 0 & u_{,y}^0 & 0 \\ u_{,y}^0 & u_{,x}^0 & 0 \end{bmatrix}, \quad \mathbf{G}_v = \begin{bmatrix} v_{,x}^0 & 0 & 0 \\ 0 & v_{,y}^0 & 0 \\ v_{,y}^0 & v_{,x}^0 & 0 \end{bmatrix}, \quad \mathbf{G}_w = \begin{bmatrix} w_{,x}^0 & 0 & 0 \\ 0 & w_{,y}^0 & 0 \\ w_{,y}^0 & w_{,x}^0 & 0 \end{bmatrix}, \\ \mathbf{G}_{a_u} = \begin{bmatrix} a_{u,x}^0 & 0 & 0 \\ 0 & a_{u,y}^0 & 0 \\ a_{u,y}^0 & a_{u,x}^0 & 0 \end{bmatrix}, \quad \mathbf{G}_{a_v} = \begin{bmatrix} a_{v,x}^0 & 0 & 0 \\ 0 & a_{v,y}^0 & 0 \\ a_{v,y}^0 & a_{v,x}^0 & 0 \end{bmatrix}, \quad \mathbf{G}_{a_w} = \begin{bmatrix} a_{w,x}^0 & 0 & 0 \\ 0 & a_{w,y}^0 & 0 \\ a_{w,y}^0 & a_{w,x}^0 & 0 \end{bmatrix} \end{aligned} \quad (3.19)$$

and

$$\begin{aligned} \mathbf{B}_{nlu_i} = & \begin{bmatrix} \frac{\partial N_i}{\partial x} & 0 & 0 & 0 & 0 & \frac{\partial N_i}{\partial x} & 0 & 0 & 0 & 0 \\ \frac{\partial N_i}{\partial y} & 0 & 0 & 0 & 0 & \frac{\partial N_i}{\partial y} & 0 & 0 & 0 & 0 \\ 0 & 0 & 0 & 0 & 0 & 0 & 0 & 0 & 0 & 0 \end{bmatrix}, \\ \mathbf{B}_{nlv_i} = & \begin{bmatrix} 0 & \frac{\partial N_i}{\partial x} & 0 & 0 & 0 & 0 & \frac{\partial N_i}{\partial x} & 0 & 0 & 0 \\ 0 & \frac{\partial N_i}{\partial y} & 0 & 0 & 0 & 0 & \frac{\partial N_i}{\partial y} & 0 & 0 & 0 \\ 0 & 0 & 0 & 0 & 0 & 0 & 0 & 0 & 0 & 0 \end{bmatrix}, \\ \mathbf{B}_{nlw_i} = & \begin{bmatrix} 0 & 0 & \frac{\partial N_i}{\partial x} & 0 & 0 & 0 & 0 & \frac{\partial N_i}{\partial x} & 0 & 0 \\ 0 & 0 & \frac{\partial N_i}{\partial y} & 0 & 0 & 0 & 0 & \frac{\partial N_i}{\partial y} & 0 & 0 \\ 0 & 0 & 0 & 0 & 0 & 0 & 0 & 0 & 0 & 0 \end{bmatrix} \end{aligned} \quad (3.20)$$

3.3 Constitutive equation

The stress field $\boldsymbol{\sigma} = \begin{bmatrix} \sigma_x & \sigma_y & \tau_{xy} & \tau_{yz} & \tau_{xz} \end{bmatrix}^T$ is computed using the constitutive equation of orthotropic laminates

$$\begin{Bmatrix} \sigma_x(x, y, z) \\ \sigma_y(x, y, z) \\ \tau_{xy}(x, y, z) \\ \tau_{yz}(x, y, z) \\ \tau_{xz}(x, y, z) \end{Bmatrix} = \begin{bmatrix} \bar{Q}_{11} & \bar{Q}_{12} & \bar{Q}_{16} & 0 & 0 \\ \bar{Q}_{12} & \bar{Q}_{22} & \bar{Q}_{26} & 0 & 0 \\ \bar{Q}_{16} & \bar{Q}_{26} & \bar{Q}_{66} & 0 & 0 \\ 0 & 0 & 0 & \bar{Q}_{44} & \bar{Q}_{45} \\ 0 & 0 & 0 & \bar{Q}_{45} & \bar{Q}_{55} \end{bmatrix} \begin{Bmatrix} \varepsilon_x(x, y, z) \\ \varepsilon_y(x, y, z) \\ \gamma_{xy}(x, y, z) \\ \gamma_{yz}(x, y, z) \\ \gamma_{xz}(x, y, z) \end{Bmatrix} = \bar{\mathbf{Q}}\boldsymbol{\varepsilon} \quad (3.21)$$

where $\bar{\mathbf{Q}}$ is the constitutive matrix of multi-layered laminate. The constitutive equation is defined based on the equivalent single layer theory that yields an approximation of a single layer by summing up the material properties of all plies, see section 2.3 for details.

Although the lower order nature of the theory leads a robust non-linear analysis, shear locking phenomena may arise. This means that the formulation locks for thin laminates, especially in a bending state. Here, the method of assumed transverse shear strains is used to avoid shear locking. By doing so, four sampling points are defined at each element edge and a linear variation of the shear strain field is formulated. The proposed method was introduced in section 2.5; however, here the shear strain matrix \mathbf{B}_s^i of XFEM is substituted into equation 2.31.

In laminated structures the variation of transverse shear stresses is piecewise parabolic. In addition, in the absence of surface loads, these stresses vanish on the lower and upper surface of the laminate. However, based on the first-order shear deformation theory these stresses are constant at each ply level and no physical stresses at the free surfaces occur. When the difference between the material properties of plies is noticeable, like in sandwich structures, the prediction of theory leads to significant errors. A typical method to overcome this problem is to multiply the shear strain field by the so-called shear correction factor. This factor is measured by dividing the strain energy from the theory of elasticity to the laminate theory. Here, a shear correction factor is calculated for intact laminate whereas two factors are dedicated to the discontinuous subdomains, see section 2.4 for details.

3.4 Equilibrium equation

In order to obtain the equilibrium equation, the principle of virtual work is applied. It is written in general format as

$$\mathbf{R}(\mathbf{q}) = \mathbf{f}^{int}(\mathbf{q}) - \mathbf{f}^{ext} = \int_V \mathbf{B}^T \boldsymbol{\sigma} dV - \mathbf{f}^{ext} = \mathbf{0} \quad (3.22)$$

where \mathbf{R} is the residual vector, \mathbf{f}^{int} is the vector of internal force, and \mathbf{f}^{ext} is the external force vector. \mathbf{B} represents the linear and non-linear components of the strains that

includes shape functions and the derivatives of them. To solve the non-linear equilibrium equation, the Newton-Raphson algorithm is adopted. The tangential matrix in this case is obtained as

$$\mathbf{K}_T = \frac{\partial \mathbf{R}}{\partial \mathbf{q}} = \int_V \frac{\partial \mathbf{B}^T}{\partial \mathbf{q}} \boldsymbol{\sigma} dV + \int_V \mathbf{B}^T \frac{\partial \boldsymbol{\sigma}}{\partial \mathbf{q}} dV \quad (3.23)$$

The developed formulation has been applied to a four-node quadrilateral element. Herein, the four-node element developed is able to capture a discontinuity through-the-thickness, at any arbitrary interface of interest. The vector of all degrees of freedom - represented as terms of unknown variables in the solution procedure - at each nodal point i is $q_i = [u^0, v^0, w^0, \theta_x^0, \theta_y^0, a_u^0, a_v^0, a_w^0, a_{\theta_x}^0, a_{\theta_y}^0]^T$. When intact laminates are investigated this vector is reduced to the first five DOFs.

3.5 Tangent stiffness matrix derivation

The tangent stiffness matrix is derived for each subdomain separately and the structural behaviour of shell with delamination is predicted by both operators. Two particular differences exist in the formulation of the lower subdomain in comparison to the upper one. The standard finite element formulation is applied to the formulation of lower subdomain and the stress resultants are calculated up to the location of discontinuity $-h/2 < z < z_d$. Therefore, the developed tangent stiffness formulation in the last chapter can be used by performing the mentioned modification in the integration domain of z direction.

In the upper subdomain, the standard and enhanced DOFs are used and the resultant stresses are computed from the location of discontinuity to the upper surface of the shell $z_d < z < h/2$. All formulations are developed with respect to the mid-plane of laminate that is located at the geometric centre of shell. In what follows the tangent stiffness matrix is derived for the upper subdomain.

Similar to chapter 2, the tangent stiffness can be split into three components: the linear stiffness matrix \mathbf{K}_L , the part of the matrix related to the initial deformations \mathbf{K}_U , and the geometric or initial stress matrix \mathbf{K}_σ as

$$\mathbf{K}_T = \mathbf{K}_L + \mathbf{K}_U + \mathbf{K}_\sigma \quad (3.24)$$

The linear stiffness is expressed as

$$\begin{aligned} \mathbf{K}_L = & \iint_A \mathbf{B}_m^T \left[\int_{z_d}^{h/2} \bar{\mathbf{Q}} dz \right] \mathbf{B}_m dA - \iint_A \mathbf{B}_m^T \left[\int_{z_d}^{h/2} z \bar{\mathbf{Q}} dz \right] \mathbf{B}_b dA - \\ & \iint_A \mathbf{B}_b^T \left[\int_{z_d}^{h/2} z \bar{\mathbf{Q}} dz \right] \mathbf{B}_m dA + \iint_A \mathbf{B}_b^T \left[\int_{z_d}^{h/2} z^2 \bar{\mathbf{Q}} dz \right] \mathbf{B}_b dA + \\ & \iint_A \mathbf{B}_s^T \left[\int_{z_d}^{h/2} \bar{\mathbf{Q}}_s dz \right] \mathbf{B}_s dA \end{aligned} \quad (3.25)$$

where \mathbf{B} consists of the derivative of shape functions and does not include the initial deformation of the structure. The strain matrices were provided in equation 3.12 to 3.20.

The part of tangent stiffness matrix related to the initial deformations \mathbf{K}_U is presented as

$$\begin{aligned}
\mathbf{K}_U = & \iint_A \mathbf{B}_m^T \left[\int_{z_d}^{h/2} \bar{\mathbf{Q}} dz \right] \frac{1}{2} [(\mathbf{G}_u + \mathbf{G}_{a_u}) \mathbf{B}_{nlu} + (\mathbf{G}_v + \mathbf{G}_{a_v}) \mathbf{B}_{nlv} + (\mathbf{G}_w + \mathbf{G}_{a_w}) \mathbf{B}_{nlw}] dA + \\
& \iint_A \mathbf{B}_m^T \left[\int_{z_d}^{h/2} \bar{\mathbf{Q}} dz \right] \frac{1}{2} \left[\left(\frac{\partial \mathbf{G}_u}{\partial \mathbf{q}} + \frac{\partial \mathbf{G}_{a_u}}{\partial \mathbf{q}} \right) \mathbf{B}_{nlu} + \left(\frac{\partial \mathbf{G}_v}{\partial \mathbf{q}} + \frac{\partial \mathbf{G}_{a_v}}{\partial \mathbf{q}} \right) \mathbf{B}_{nlv} + \right. \\
& \left. \left(\frac{\partial \mathbf{G}_w}{\partial \mathbf{q}} + \frac{\partial \mathbf{G}_{a_w}}{\partial \mathbf{q}} \right) \mathbf{B}_{nlw} \right] \mathbf{q} dA - \\
& \iint_A \mathbf{B}_b^T \left[\int_{z_d}^{h/2} \bar{\mathbf{Q}} dz \right] \frac{1}{2} [(\mathbf{G}_u + \mathbf{G}_{a_u}) \mathbf{B}_{nlu} + (\mathbf{G}_v + \mathbf{G}_{a_v}) \mathbf{B}_{nlv} + (\mathbf{G}_w + \mathbf{G}_{a_w}) \mathbf{B}_{nlw}] dA + \\
& \iint_A \mathbf{B}_b^T \left[\int_{z_d}^{h/2} \bar{\mathbf{Q}} dz \right] \frac{1}{2} \left[\left(\frac{\partial \mathbf{G}_u}{\partial \mathbf{q}} + \frac{\partial \mathbf{G}_{a_u}}{\partial \mathbf{q}} \right) \mathbf{B}_{nlu} + \left(\frac{\partial \mathbf{G}_v}{\partial \mathbf{q}} + \frac{\partial \mathbf{G}_{a_v}}{\partial \mathbf{q}} \right) \mathbf{B}_{nlv} + \right. \\
& \left. \left(\frac{\partial \mathbf{G}_w}{\partial \mathbf{q}} + \frac{\partial \mathbf{G}_{a_w}}{\partial \mathbf{q}} \right) \mathbf{B}_{nlw} \right] \mathbf{q} dA - \\
& \iint_A [(\mathbf{G}_u + \mathbf{G}_{a_u}) \mathbf{B}_{nlu} + (\mathbf{G}_v + \mathbf{G}_{a_v}) \mathbf{B}_{nlv} + (\mathbf{G}_w + \mathbf{G}_{a_w}) \mathbf{B}_{nlw}]^T \left[\int_{z_d}^{h/2} \bar{\mathbf{Q}} dz \right] \mathbf{B}_m dA - \\
& \iint_A [(\mathbf{G}_u + \mathbf{G}_{a_u}) \mathbf{B}_{nlu} + (\mathbf{G}_v + \mathbf{G}_{a_v}) \mathbf{B}_{nlv} + (\mathbf{G}_w + \mathbf{G}_{a_w}) \mathbf{B}_{nlw}]^T \left[\int_{z_d}^{h/2} z \bar{\mathbf{Q}} dz \right] \mathbf{B}_b dA + \\
& \iint_A [(\mathbf{G}_u + \mathbf{G}_{a_u}) \mathbf{B}_{nlu} + (\mathbf{G}_v + \mathbf{G}_{a_v}) \mathbf{B}_{nlv} + (\mathbf{G}_w + \mathbf{G}_{a_w}) \mathbf{B}_{nlw}]^T \left[\int_{z_d}^{h/2} \bar{\mathbf{Q}} dz \right] \\
& \frac{1}{2} [(\mathbf{G}_u + \mathbf{G}_{a_u}) \mathbf{B}_{nlu} + (\mathbf{G}_v + \mathbf{G}_{a_v}) \mathbf{B}_{nlv} + (\mathbf{G}_w + \mathbf{G}_{a_w}) \mathbf{B}_{nlw}] dA + \\
& \iint_A [(\mathbf{G}_u + \mathbf{G}_{a_u}) \mathbf{B}_{nlu} + (\mathbf{G}_v + \mathbf{G}_{a_v}) \mathbf{B}_{nlv} + (\mathbf{G}_w + \mathbf{G}_{a_w}) \mathbf{B}_{nlw}]^T \left[\int_{z_d}^{h/2} \bar{\mathbf{Q}} dz \right] \\
& \frac{1}{2} \left[\left(\frac{\partial \mathbf{G}_u}{\partial \mathbf{q}} + \frac{\partial \mathbf{G}_{a_u}}{\partial \mathbf{q}} \right) \mathbf{B}_{nlu} + \left(\frac{\partial \mathbf{G}_v}{\partial \mathbf{q}} + \frac{\partial \mathbf{G}_{a_v}}{\partial \mathbf{q}} \right) \mathbf{B}_{nlv} + \left(\frac{\partial \mathbf{G}_w}{\partial \mathbf{q}} + \frac{\partial \mathbf{G}_{a_w}}{\partial \mathbf{q}} \right) \mathbf{B}_{nlw} \right] \mathbf{q} dA
\end{aligned} \tag{3.26}$$

The geometric stiffness matrix is derived from the first integral of equation 3.23 as

$$\begin{aligned}
\mathbf{K}_\sigma = & \iint_A \left[\left(\frac{\partial \mathbf{G}_u}{\partial \mathbf{q}} + \frac{\partial \mathbf{G}_{a_u}}{\partial \mathbf{q}} \right) \mathbf{B}_{nlu} + \right. \\
& \left. \left(\frac{\partial \mathbf{G}_v}{\partial \mathbf{q}} + \frac{\partial \mathbf{G}_{a_v}}{\partial \mathbf{q}} \right) \mathbf{B}_{nlv} + \left(\frac{\partial \mathbf{G}_w}{\partial \mathbf{q}} + \frac{\partial \mathbf{G}_{a_w}}{\partial \mathbf{q}} \right) \mathbf{B}_{nlw} \right]^T \boldsymbol{\sigma}_r dA
\end{aligned} \tag{3.27}$$

where $\boldsymbol{\sigma}_r$ is the vector of in-plane stress resultants. These resultants are calculated in $z_d < z < h/2$ domain, particularly.

3.6 Transformation to the global coordinate system

In order to establish the equilibrium state of shell, nodal displacements and forces are transformed into the global Cartesian coordinate system. Therefore, the projection of these quantities in z direction produces a new rotational DOF that is known by $\theta_{z_g}^0$. Due to the enhancement of DOFs by XFEM, one more rotational DOF in z direction has to be added. Hence, the nodal DOFs in the global coordinate system are described by $q_{g_i} = [u_g^0, v_g^0, w_g^0, \theta_{x_g}^0, \theta_{y_g}^0, \theta_{z_g}^0, a_{u_g}^0, a_{v_g}^0, a_{w_g}^0, a_{\theta_{x_g}}^0, a_{\theta_{y_g}}^0, a_{\theta_{z_g}}^0]^T$.

The transformation matrix is orthogonal. It is presented for each nodal point i ($i=1$ to 4) by

$$\mathbf{T}_i = \begin{bmatrix} \mathbf{T}_{6 \times 6}^{FEM} & 0 \\ 0 & \mathbf{T}_{6 \times 6}^{XFEM} \end{bmatrix} \quad (3.28)$$

where \mathbf{T}^{FEM} and \mathbf{T}^{XFEM} are the transformation matrix of the regular and the enhanced components, respectively. The transformation matrix is formed by calculating the cosine of the local axes x , y , and z with respect to the global ones X , Y , and Z (see equations 2.49 - 2.53 for details). Since all formulations are derived in the reference configuration, the transformation matrix for the enhanced DOFs (\mathbf{T}^{XFEM}) is the same as for the regular DOFs (\mathbf{T}^{FEM}). Henceforth, the stiffness matrix in the global coordinate system is written as

$$\mathbf{K}_{T,g} = \mathbf{T}^T \mathbf{K}_T \mathbf{T} \quad (3.29)$$

where $\mathbf{K}_{T,g}$ and \mathbf{K}_T are the global and local tangent stiffness matrix, respectively. Similarly, the vector of internal force is transformed by

$$\mathbf{f}_g^{\text{int}} = \mathbf{T}^T \mathbf{f}^{\text{int}} \quad (3.30)$$

where $\mathbf{f}_g^{\text{int}}$ and \mathbf{f}^{int} are the global and local internal forces, respectively.

The rotation field in warped elements has been modified before performing the transformation. By doing so, the nodes located in warped plane are connected to the un-warped ones by rigid links, see section 2.10 for details.

3.7 Technique for avoiding singularity

Similar to what was proposed in section 2.9, the singularity has to be removed in the discontinuous co-planar elements. However, the contribution of extra DOFs needs a small modification to the approaches that was discussed in section 2.9. Here the fictitious stiffness matrix is assigned to both $K_{\theta_{z_g}^0}$ and $K_{a_{\theta_{z_g}^0}^0}$ component. Furthermore, the drilling potential energy, containing a penalty parameter, can be reformulated as

$$\Pi_{drilling} = \frac{1}{2} \int_{\Omega} P \left(\omega^0 - \left(\theta_{z_g}^0 + \bar{H}(z_d) a_{\theta_{z_g}^0}^0 \right) \right)^2 d\Omega \quad (3.31)$$

where P is the penalty parameter, $\theta_{z_g}^0$ and $a_{\theta_{z_g}}^0$ are the drilling DOFs, and ω^0 is the in-plane rotation of shell that is related to the membrane DOFs as

$$\omega^0 = \frac{1}{2} \left(\left(v_{,x}^0 + \overline{H}(z_d) a_{v,x}^0 \right) - \left(u_{,y}^0 + \overline{H}(z_d) a_{u,y}^0 \right) \right) \quad (3.32)$$

The penalty parameter in equation 3.31 can be chosen of the same order as the transverse modulus. It is of importance to overcome the singularity within the local Cartesian coordinate system. Therefore, the drilling stiffness coefficients are appended to the local stiffness matrix before transforming it into the global coordinate system.

3.8 Closing remarks

In this chapter, a novel discontinuous shell formulation was developed. The derived element has four nodes whilst it can predict the response of shell with delamination. The tangent operator of the discontinuous shell element can be called locally and the geometrical simulation of subdomains is neglected. In the present formulation no further constraint is needed to connect the nodal points at the delamination front and this can be formed by excluding the extra DOFs in the corresponding nodes. The availability of the enhanced displacements and rotations can be of help to superimpose a traction-separation law for tracking the delamination onset and growth. Since in XFEM the discontinuous domain is simulated by adding extra DOFs, a post-processing is required to visualize the results. In the present formulation, the response of the upper subdomain is detected by appending the values of enhanced DOFs to the standard ones. Thus, new elements are generated in post-processing in ANSYS and the corresponding displacements and rotations are assigned to them. In this chapter the verification studies were avoided and the formulation of discontinuous shell is examined in combination with the interface formulation in the subsequent chapters. In the next chapter the formulation of two cohesive zone models and a contact formulation are described in details.

Chapter 4

Interface formulation

4.1 Introduction

Failure in composite materials is divided into three general categories: fibre breakage, matrix cracking, and delamination between plies. The inevitable imperfections that are produced in manufacturing, the cracks that are generated by fatigue, the stress concentration near discontinuities, and the high interlaminar stresses are the main causes to provoke delamination (Barbero, 2013). The delamination can be simulated similar to any failure mechanism by defining a damage initiation criterion, a damage evaluation law, and the element removal process after completely damaged condition (Barenblatt, 1959). The cohesive zone model is commonly used to model the failure at interfaces (see e.g. (Camanho and Dávila, 2002; Alfano and Crisfield, 2001; Yazdani et al., 2016b; Balzani and Wagner, 2008; Yazdani et al., 2016a)). It is based on the relative structural motion of the bonded surfaces. The cohesive zone model is defined by a traction-separation law that is inherently embedded into the discontinued domain. Cohesive zone models eliminate the stress singularity at the delamination front. In a finite element procedure, meshes are aligned at the plane of discontinuity and the cohesive element is introduced between the associated nodes at each surface. However, in this thesis the discontinuous domain is not introduced instead the XFEM formulation is being utilized. The detailed procedure is provided in the following sections.

4.2 Implementation aspects

In order to take into account the discontinuity, the shell element is split into two domains. These domains are shown in figure 4.1.

There exist two approaches to model the delamination in composite laminates: modelling two subdomains in the delaminated zone and one laminate in the intact region; and modelling two subdomains in the entire domain and applying kinematic constraints to bond it in the intact region. In both aforementioned methods, the same mesh scheme should be applied at the debonded surface to accurately calculate the projection of nodes, and consequently the relative displacements at the interface region. However, taking advantages of XFEM one can apply the discontinuity in the formula-

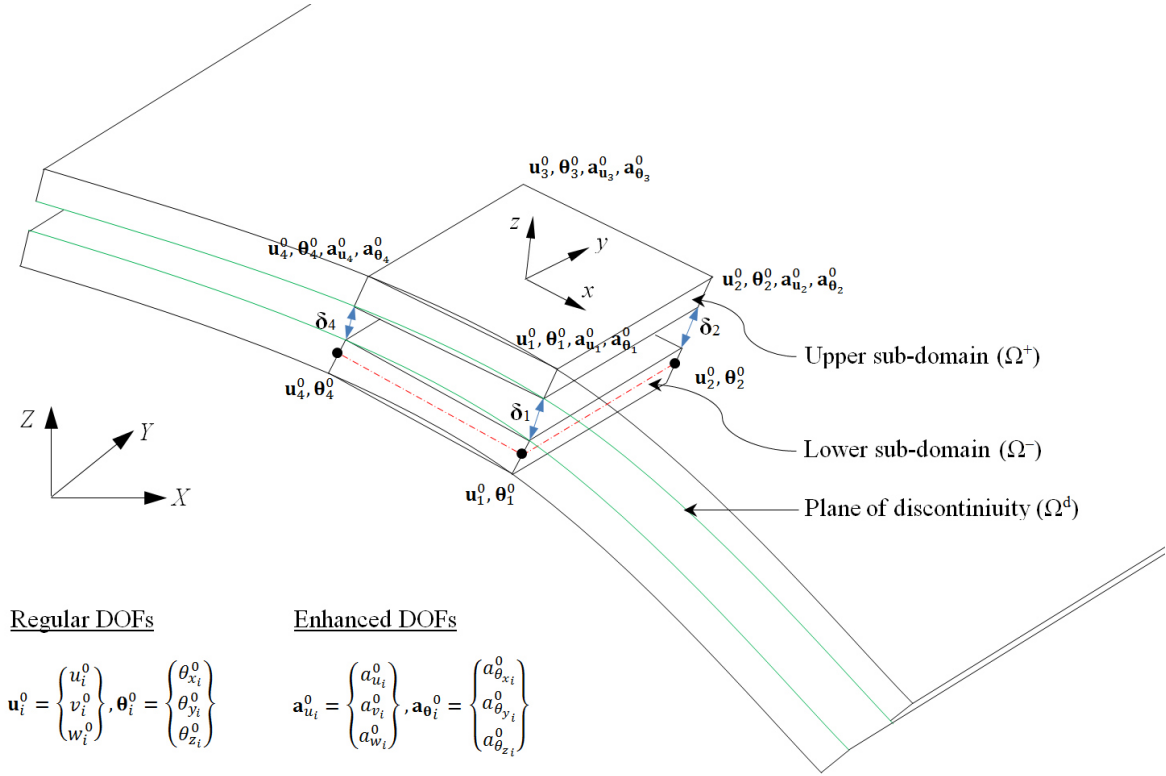


Figure 4.1: Schematic view of a shell element in a delaminated domain.

tion of a four-node element itself; thus, no effort is required to align the mesh schemes and the displacement jump is calculated precisely. Taking into account the first-order shear deformation theory and the XFEM formulation, one may write the relative displacements at the discontinuous subdomains through the enhanced displacements and rotations in the following form

$$\boldsymbol{\delta} = \begin{Bmatrix} U \\ V \\ W \end{Bmatrix}_{\Omega^+} - \begin{Bmatrix} U \\ V \\ W \end{Bmatrix}_{\Omega^-} = \begin{Bmatrix} a_u^0 + z_d a_{\theta_y}^0 \\ a_v^0 - z_d a_{\theta_x}^0 \\ a_w^0 \end{Bmatrix} \quad (4.1)$$

Here $\boldsymbol{\delta}$ is the nodal relative motion of the interface and z_d is the location of the discontinuity in z direction (see figure 4.1). The generalized form of the relative motion is presented in terms of unknown values as

$$\boldsymbol{\delta} = \sum_{i=1}^4 \mathbf{B}_{c_i} \mathbf{q}_i \quad (4.2)$$

where

$$\mathbf{B}_{c_i} = \begin{bmatrix} 0 & 0 & 0 & 0 & 0 & N_i & 0 & 0 & 0 & z_d N_i \\ 0 & 0 & 0 & 0 & 0 & 0 & N_i & 0 & -z_d N_i & 0 \\ 0 & 0 & 0 & 0 & 0 & 0 & 0 & N_i & 0 & 0 \end{bmatrix} \quad (4.3)$$

It is noted that the x and y components of δ_i contribute to fracture Mode II and III whereas z component represents Mode I. The aforementioned order of the components is followed in the subsequent equations. The subscript c denotes the components associate with the cohesive formulation. Two general approaches are used in order to apply the displacement continuity at the interfaces: modelling the interface stiffness by a large penalty stiffness or the Lagrange multiplier. In this thesis, the penalty method is employed and the stress components are obtained directly through the traction-separation relation as follows

$$\boldsymbol{\sigma}_c = \mathbf{P}\boldsymbol{\delta} \quad (4.4)$$

where \mathbf{P} is the penalty stiffness matrix and $\boldsymbol{\sigma}_c$ is the vector of stresses. The penalty stiffness must be chosen large enough to bond the subdomains and to prevent the inward interpenetration of them. It is noted that although adopting very large values leads to more precised results, the presence of large stiffness values causes computational deficiency.

In the isotropic and homogeneous material, the crack tip can grow in the same direction as the applied load. However, in composite laminates delamination grows at the interface direction within any arbitrary path and because of the weak toughness of interface it is rarely entered into the adjacent plies (Barbero, 2013). Therefore, a mixed-mode cohesive formulation is required to accurately simulate the delamination. The available cohesive formulations are categorized into two main groups:

- The formulations based on using a surface potential in which an exponential form of cohesive zone model is developed, e.g. in (Xu and Needleman, 1994; Ortiz and Pandolfi, 1999) and
- The formulations based on bilinear traction-separation law, e.g. in (Alfano and Crisfield, 2001; Camanho and Dávila, 2002).

4.3 Mixed-mode bilinear cohesive zone model

The bilinear traction-displacement relation consists of two parts namely linear and softening. An appropriate damage criterion is utilized to identify the damage initiation and subsequently to contribute the softening behaviour at the interface. The traction-separation diagram for the fracture Mode i is depicted in figure 4.2.

As soon as the traction reaches the strength of the interface σ^0 damage is initiated and the stored energy in the linear regime is released. In other words, it can be stated that, as soon as the opening distance of the interfaces reaches $\delta^0 = \sigma^0/P$, the damage is initiated. Therefore, a gradual reduction of stiffness is traced.

When the damage is nucleated, the cohesive formulation experiences the softening behaviour. Therefore, a new traction-separation law is held and the constitutive equation is recalculated within an iterative procedure and based on the damage evolution parameter that is updated. This degradation process is continued until an energy equals to the fracture toughness of the interface is attained or in other words the displacement jump approaches the final displacement of the interface δ^f . Thereafter, the formulation of cohesive zone is removed and the regular structural response of sub-

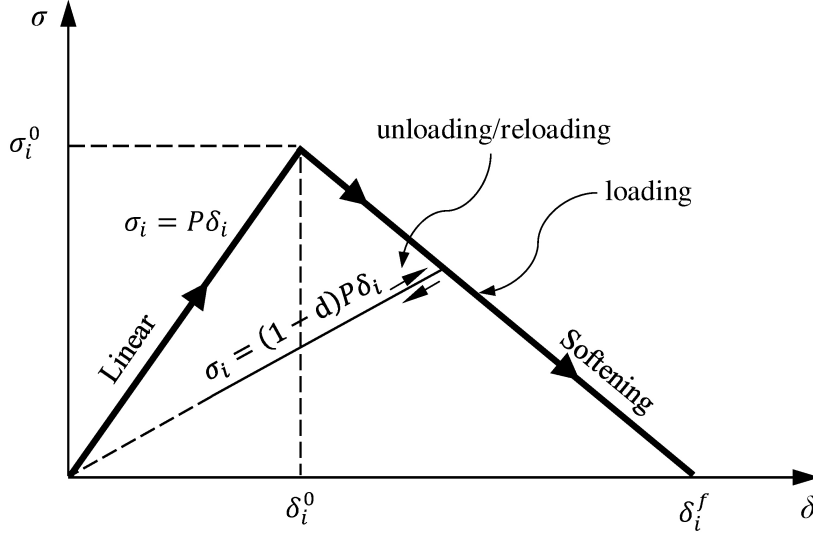


Figure 4.2: Traction-separation diagram of the cohesive zone model in the fracture Mode i .

domains is accomplished. The stress-displacement relation in the softening region is written as

$$\sigma_c = \mathbf{P}(1 - d)\delta \quad (4.5)$$

The cohesive formulation is incorporated during the fracture process until the energy release rate reaches its critical value G^{cr} . The area below the traction-separation diagram represents the critical energy release rate. This can be formulated for each mode as follows

$$G^{cr} = \int_0^{\delta^f} \sigma_c d\delta \quad (4.6)$$

Thus, the maximum displacement of the cohesive effect with linear softening is obtained by $\delta^f = 2G^{cr}/\sigma^0$. The displacement parameters δ^0 and δ^f are accounted for activating the softening behaviour and for eliminating the cohesive formulation, respectively.

The above diagram is changed when the ductile adhesive is used. It is more adequate to employ trapezoidal softening law including the plastic behaviour of adhesive (Campilho et al., 2008). Therefore, the bilinear diagram is modified as figure 4.3. The subscript i indicates the fracture Mode i and the subscript m specifies the interaction of modes in the mixed-mode case. However, in this thesis the ductile adhesive is not of interest and the mixed-mode will be considered through an applicable technique.

A novel mixed-mode formulation was proposed by Camanho and Dávila (2002) for the delamination analysis. This formulation is based on a bilinear traction-separation law and it was successfully employed for shell elements in (Dávila et al., 2007). The traction-separation diagram is presented in figure 4.4.

As it is shown in figure 4.4, the normal and shear modes are depicted individually whilst their contribution into a mixed-mode framework is also provided. Therefore, one can explore a mixture of the fracture modes through measuring the resultant of the displacements at the damage onset δ_m^0 and the maximum resultant of displacements

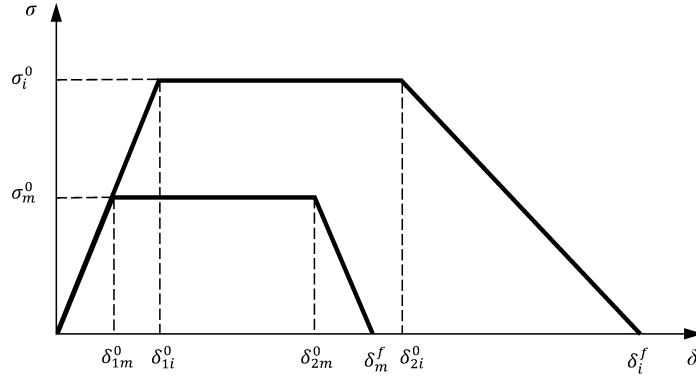


Figure 4.3: Traction-separation diagram of ductile adhesive.

that can be achieved by the interface formulation δ_m^f . According to the type of loading, and consequently the ratio of fracture modes, damage can be initiated at any point on the dotted line. The mixed-mode displacement jump can be obtained through the

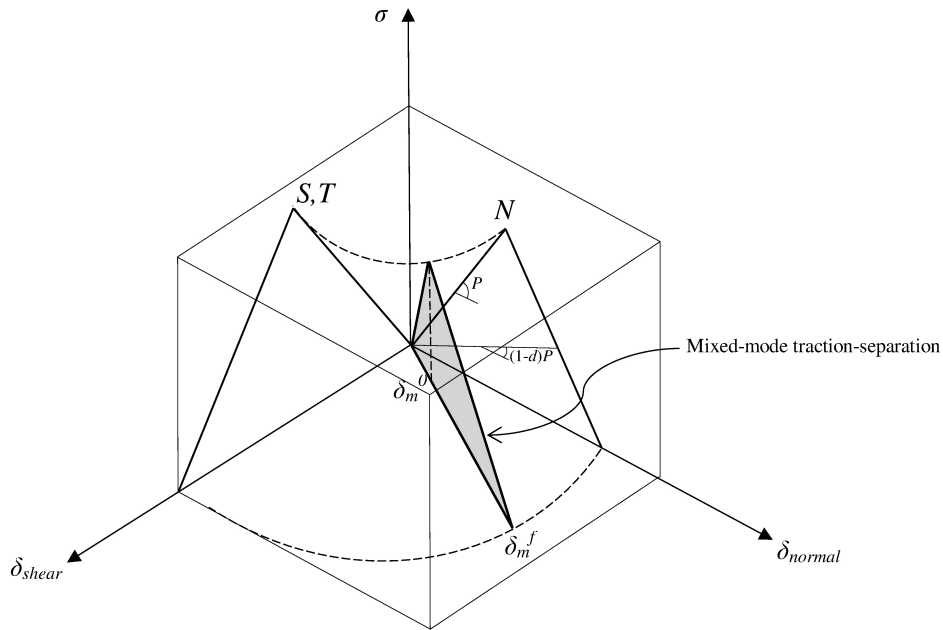


Figure 4.4: Mixed-mode traction-separation law.

calculation of displacement resultant as

$$\delta_m = \sqrt{\langle \delta_I \rangle^2 + \delta_{II}^2 + \delta_{III}^2} \quad (4.7)$$

where δ_I , δ_{II} , and δ_{III} are the principal relative displacements of the delaminated region. The ratio of the acquired shear to the normal displacement jump during the loading process is expressed by (Camanho and Dávila, 2002)

$$\kappa = \delta_{shear} / \delta_I \quad (4.8)$$

where $\delta_{II}^0 = \delta_{III}^0 = \delta_{shear}^0$ and the above equation holds if $\delta_I \geq 0$.

The damage onset criterion of the cohesive formulation in the mixed-mode condition is presented through one of the following widely used criterion:

- Maximum nominal strain criterion,
- Maximum nominal stress criterion,
- Quadratic nominal strain criterion and
- Quadratic nominal stress criterion.

The quadratic nominal stress criterion is depicted here. It is written as

$$\left(\frac{\langle \sigma_{cI} \rangle}{N}\right)^2 + \left(\frac{\sigma_{cII}}{S}\right)^2 + \left(\frac{\sigma_{cIII}}{T}\right)^2 = 1 \quad (4.9)$$

where N , T , and S are the strength of interface in normal and shear directions, respectively. The Macaulay bracket is used to suppress the negative stresses in the normal direction.

In order to simulate the delamination growth in mixed-mode loading, the interaction relationship of energies is required. For this, two main criteria are generally employed:

- Benzeggagh-Kenane fracture criterion and
- Power law fracture criterion.

Both approaches are applied frequently in the fracture analysis. They are used to simulate the limit of fracture process or in other words the degradation process at the interface. Herein, a power law criterion is depicted. By employing the Linear Elastic Fracture Mechanics (LEFM) mode ratio of energy release rates is obtained and is expressed as

$$\left(\frac{G_I}{G_I^{cr}}\right)^\beta + \left(\frac{G_{shear}}{G_{shear}^{cr}}\right)^\beta = 1 \quad (4.10)$$

where $G^{cr} = G_I + G_{shear}$; and β is chosen based on the material properties of the composite materials and experiments. If Mode III does not occur, the term G_{shear} in the power law criterion attributes to shear mode G_{II} . In this thesis, the power law criterion in the quadratic format is used; therefore, β is set to 2.

The stress-displacement relation of the mixed-mode cohesive zone model in its general format is written as

$$\boldsymbol{\sigma}_c = \mathbf{D}\boldsymbol{\delta} \quad (4.11)$$

where \mathbf{D} is the constitutive matrix that is differed in the linear and softening regime; and based on the following behaviour the traction vector is retrieved. The constitutive

matrix is formulated as

$$\mathbf{D} = \begin{cases} \bar{\delta}_{ij}P & \delta_m^{max} \leq \delta_m^0 \\ \bar{\delta}_{ij}P \left[(1-d) + d\bar{\delta}_{iI} \frac{\langle -\delta_I \rangle}{-\delta_I} \right] & \delta_m^0 < \delta_m^{max} < \delta_m^f \\ \bar{\delta}_{iI}\bar{\delta}_{Ij} \frac{\langle -\delta_I \rangle}{-\delta_I} P & \delta_m^{max} \geq \delta_m^f \end{cases} \quad (4.12)$$

where $\bar{\delta}$ is the Kronecker delta, δ_m^{max} is the maximum mixed-mode displacement that is achieved during the loading steps, and $\langle \bullet \rangle$ is the Macaulay bracket which is used to avoid the penetration of subdomains in the Mode I of delamination.

The damage evolution function in the softening zone is calculated as

$$d = \frac{\delta_m^f (\delta_m^{max} - \delta_m^0)}{\delta_m^{max} (\delta_m^f - \delta_m^0)} \quad (4.13)$$

The value of the damage evolution function alters from 0 to 1. It gets value of 0 in the damage onset and it reaches, consequently, to value of 1 during the damage propagation process. At this level of loading, the traction is reduced to zero; thus the cohesive formulation is removed and the new delamination surfaces are generated. The parameters δ_m^0 and δ_m^f are calculated after each converged load step to set the proper constitutive equation for the subsequent analysis. The detail procedure of calculating these parameters is provided in the following.

Considering N , T , and S as the strength of interface, the delamination onset in terms of displacement is obtained using the linear constitutive equation of interface

$$\delta_I^0 = \frac{N}{P}, \quad \delta_{II}^0 = \delta_{III}^0 = \delta_{shear}^0 = \frac{S}{P} \quad (4.14)$$

By substituting the equation 4.8 into equation 4.7, the mixed-mode relative displacement can be written as

$$\delta_m = \delta_I \sqrt{1 + \kappa^2} \quad (4.15)$$

By substituting the traction vector of equation 4.11 into equation 4.9 the delamination onset criterion in terms of displacements is derived as

$$\delta_I = \delta_I^0 \delta_{shear}^0 \sqrt{\frac{1}{(\delta_{shear}^0)^2 + \kappa^2 (\delta_I^0)^2}} \quad (4.16)$$

Equation 4.16 is rewritten in term of the mixed-mode displacement at delamination onset using equation 4.15 as follows

$$\delta_m^0 = \delta_I^0 \delta_{shear}^0 \sqrt{\frac{1 + \kappa^2}{(\delta_{shear}^0)^2 + \kappa^2 (\delta_I^0)^2}} \quad (4.17)$$

Next, the mixed-mode displacement at ultimate failure is determined. Taking into account the equation 4.6, the energy release rate for each particular mode at the ultimate failure is obtained by

$$G_i = \int_0^{\delta_i^f} \sigma_{c_i} d\delta_i \quad \text{where } i=\text{I, II, and III} \quad (4.18)$$

Substituting the traction vector of an individual mode i into the equation 4.18, the strain energy is obtained as

$$G_i = \frac{1}{2} P \delta_i^0 \delta_i^f \quad (4.19)$$

Using equations 4.19, 4.15, and 4.17 in the power law, the ultimate mixed-mode displacement is achieved as

$$\delta_m^f = \frac{(1 + \kappa^2)}{P \delta_m^0} \left(\left(\frac{1}{G_I^{cr}} \right)^\beta + \left(\frac{\kappa^2}{G_{shear}^{cr}} \right)^\beta \right)^{-1/\beta} \quad (4.20)$$

The tangent stiffness matrix in bilinear interface formulation is derived by linearizing the residual vector as follows. The internal force of the interface region is written as

$$\mathbf{f}_c^{int} = \int \mathbf{B}_c^T \boldsymbol{\sigma}_c d\Omega^d \quad (4.21)$$

In the above equation, the matrix \mathbf{B}_c consists of shape functions that are constant. However, the traction vector is a function of unknown variables. Therefore, the tangent stiffness operator is determined by carrying out the partial derivative of the traction vector with respect to the variables as follows

$$\mathbf{K}_{T,c} = \frac{\partial \mathbf{f}_c^{int}}{\partial \mathbf{q}} = \int \mathbf{B}_c^T \mathbf{D}(d(\mathbf{q})) \mathbf{B}_c d\Omega^d + \int \mathbf{B}_c^T \frac{\partial \mathbf{D}(d(\mathbf{q}))}{\partial \mathbf{q}} \mathbf{B}_c d\Omega^d \mathbf{q} \quad (4.22)$$

The first integral gives the secant stiffness matrix that is determined straightforward. However, the second integral has to be derived thoroughly. The derivations are given in details as follows

$$\frac{\partial \mathbf{D}(d(\mathbf{q}))}{\partial \mathbf{q}} = \frac{\partial \mathbf{D}}{\partial d} \frac{\partial d}{\partial \mathbf{q}} \quad (4.23)$$

where the term $\frac{\partial \mathbf{D}}{\partial d}$ is calculated directly by taking the derivative of \mathbf{D} in equation 4.12 with respect to the damage parameter

$$\frac{\partial \mathbf{D}}{\partial d} = \begin{cases} \begin{bmatrix} -P & 0 & 0 \\ 0 & -P & 0 \\ 0 & 0 & -P \end{bmatrix} & \text{if } \delta_I > 0 \\ \begin{bmatrix} -P & 0 & 0 \\ 0 & -P & 0 \\ 0 & 0 & 0 \end{bmatrix} & \text{if } \delta_I < 0 \end{cases} \quad (4.24)$$

The second part of equation 4.23 is written as

$$\frac{\partial d}{\partial \mathbf{q}} = \frac{\partial d}{\partial \delta} \frac{\partial \delta}{\partial \mathbf{q}} \quad (4.25)$$

where $\frac{\partial \delta}{\partial \mathbf{q}}$ represents the interface \mathbf{B}_c matrix and δ is the mixed-mode relative displacement of the interface zone. In order to have a progressive and irreversible damage while the load is being increased, the maximum resultant of the mixed-mode displacement jump δ_{max} is stored as a history variable. This variable represents the maximum displacement jump within the last converged steps. Based on the aforementioned parameter, a loading function is introduced as

$$F(\delta - \delta_{max}) = \frac{\frac{1}{2} [(\delta - \delta_{max}) + |\delta - \delta_{max}|]}{\delta - \delta_{max}} \quad (4.26)$$

The loading function gets the value of one in case the loading is continued and is set to zero when the unloading appears. Subsequently, the first derivative of equation 4.25 is calculated as

$$\frac{\partial d}{\partial \delta} = \frac{\partial d}{\partial \delta_{max}} \frac{\partial \delta_{max}}{\partial \delta} \quad (4.27)$$

where the introduced loading function of equation 4.26 is involved in the derivation of partial differential equation of the above formula as

$$\frac{\partial \delta_{max}}{\partial \delta} = F(\delta - \delta_{max}) \frac{\delta^T}{\delta} \left[\mathbf{1} - \bar{\delta}_{s1} + \frac{\langle \delta_I \rangle}{\delta_I} \bar{\delta}_{s1} \right] \quad (4.28)$$

In addition, taking into account the bilinear damage parameter, the first term of equation 4.27 is determined as

$$\frac{\partial d}{\partial \delta_{max}} = \frac{\delta_m^f \delta_m^0}{(\delta_m^{max})^2 (\delta_m^f - \delta_m^0)} \quad (4.29)$$

By substituting the detailed derivatives into the equation 4.22, the tangent stiffness matrix reads as

a) if $\delta_I > 0$

$$\mathbf{K}_{T,c} = \iint \mathbf{B}_c^T \mathbf{D}(d(\mathbf{q})) \mathbf{B}_c d\Omega^d + \iint \mathbf{B}_c^T \begin{bmatrix} -P & 0 & 0 \\ 0 & -P & 0 \\ 0 & 0 & -P \end{bmatrix} \frac{\delta_m^f \delta_m^0}{(\delta_m^{max})^2 (\delta_m^f - \delta_m^0)} F(\delta - \delta_{max}) \frac{\delta^T}{\delta} \delta \begin{bmatrix} 1 & 0 & 0 \\ 0 & 1 & 0 \\ 0 & 0 & 1 \end{bmatrix} \mathbf{B}_c d\Omega^d \quad (4.30)$$

b) if $\delta_I < 0$

$$\mathbf{K}_{T,c} = \iint \mathbf{B}_c^T \mathbf{D}(d(\mathbf{q})) \mathbf{B}_c d\Omega^d + \iint \mathbf{B}_c^T \begin{bmatrix} -P & 0 & 0 \\ 0 & -P & 0 \\ 0 & 0 & 0 \end{bmatrix} \frac{\delta_m^f \delta_m^0}{(\delta_m^{max})^2 (\delta_m^f - \delta_m^0)} F(\delta - \delta_{max}) \frac{\delta^T}{\delta} \delta \begin{bmatrix} 1 & 0 & 0 \\ 0 & 1 & 0 \\ 0 & 0 & 0 \end{bmatrix} \mathbf{B}_c d\Omega^d \quad (4.31)$$

4.4 Mixed-mode linear-exponential cohesive zone model

Convergence difficulties are encountered when the cohesive formulation is implemented in order to trace the delamination propagation. The tangent stiffness matrix has different signs in the linear and softening regimes. Therefore, once the damage is initiated, the governing equation of the system is updated abruptly in the softening regime. Subsequently, more number of iterations is needed in order to acquire the converged results. Another fact that can influence the convergence of the model is related to the length of the softening regime. A better convergence can be attained when the softening region is elongated. A traditional method to do so is to reduce the strength of interface. Therefore, taking into account the critical energy release rate as constant, the softening region is enlarged. This lets the element behind the crack front to experience the softening behaviour before removing the cohesive behaviour at the crack front. Due to the aforementioned fact, the exponential damage evaluation can be of help and the formulation of this subsection is provided with regards to this aim. Since in the typical cohesive formulation - in that the bilinear traction-separation law is inserted - the traction of the softening regime is reduced by a constant slope, the exponential degradation of it can be of help to maintain the cohesive formulation of the crack front in each load step.

An exponential damage evaluation law is selected. Therefore, the cohesive formulation is represented with a new damage parameter as (Abaqus Documentation, 2008)

$$d = 1 - \frac{\delta_m^0}{\delta_m^{max}} \left\{ 1 - \frac{1 - e^{-\alpha \left(\frac{\delta_m^{max} - \delta_m^0}{\delta_m^f - \delta_m^0} \right)}}{1 - e^{-\alpha}} \right\} \quad (4.32)$$

where α is a non-dimensional material parameter that influences the softening regime and δ_m^{max} is the maximum mixed-mode relative displacement that has been achieved throughout the loading process. Again, the value of damage evolution parameter is altered from zero to one for which zero corresponds to the perfectly bonded interface whereas the value one represents the fully debonded region. The effect of α on the exponential damage parameter and the prolongation of the softening behaviour is depicted in figure 4.5.

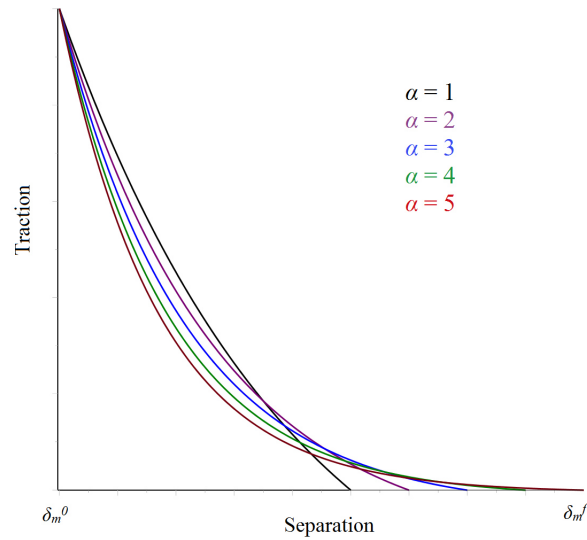


Figure 4.5: The effect of parameter α on the length of exponential softening regime.

Apart from the advantage of exponential softening behaviour that elongates the softening process, due to the non-differentiable peak of the traction-separation law, the sign of tangent operator is changed abruptly in the global non-linear equations that leads to convergence difficulties; see Gustafson and Waas (2008) for a detailed discussion on the computational efficiency and robustness of cohesive zone models. In order to better clarify the depicted exponential damage evaluation law, a schematic view of the mixed-mode cohesive effect is presented in figure 4.6.

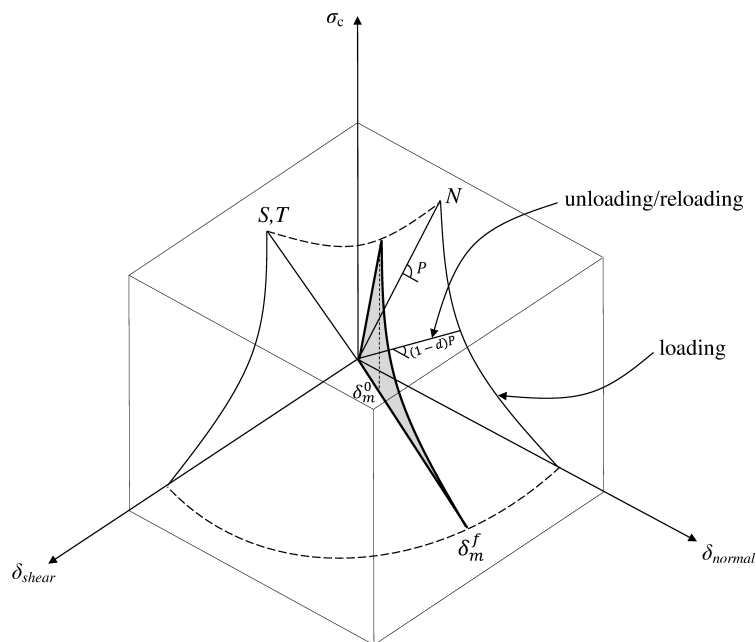


Figure 4.6: Mixed-mode traction-separation law with the exponential damage parameter.

By substituting the new damage parameter in the constitutive equation of interface, a new traction-separation law is generated. In order to assign the appropriate constitutive equation during the loading procedure, the mixed-mode displacement at the delamination onset and the final failure should be derived. Since the exponential damage parameter contributes exclusively to the softening behaviour, the same δ_m^0 as of equation 4.17 is exploited. However, the mixed-mode displacement at the final failure has to be calculated thoroughly. Therefore, by substituting the traction vector of exponential softening into equation 4.18, the strain energy is achieved as

$$G_i = P\delta_i^0\delta_i^f \left(\frac{1 - e^{-\alpha}(\alpha + 1)}{\alpha(1 - e^{-\alpha})} \right) + P(\delta_i^0)^2 \left(\frac{e^{-\alpha}(\alpha + 2) + \alpha - 2}{2\alpha(1 - e^{-\alpha})} \right) \quad (4.33)$$

Using equations 4.33, 4.15, and 4.17 and using the power law criterion lead to the ultimate mixed-mode displacement as

$$\delta_m^f = \frac{(1 + \kappa^2)}{P\delta_m^0} \left(\frac{\alpha(1 - e^{-\alpha})}{1 - e^{-\alpha}(\alpha + 1)} \right) \left(\left(\left(\frac{1}{G_I^{cr}} \right)^\beta + \left(\frac{\kappa^2}{G_{shear}^{cr}} \right)^\beta \right)^{-1/\beta} - \frac{P\delta_m^0{}^2}{(1 + \kappa^2)} \left(\frac{e^{-\alpha}(\alpha + 2) + \alpha - 2}{2\alpha(1 - e^{-\alpha})} \right) \right) \quad (4.34)$$

The tangent stiffness is derived by using equation 4.22 and the same derivations that was explained for the bilinear cohesive formulation equations 4.23 - 4.29 should be followed. However, here the exponential damage evolution law is inserted. Therefore, the first term of equation 4.27 is derived as

$$\frac{\partial d}{\partial \delta_{max}} = \frac{\delta_m^0}{(\delta_m^{max})^2} + \left(\frac{1}{1 - e^{-\alpha}} \right) \left(\frac{\delta_m^0}{(\delta_m^{max})^2} \right) \left\{ -1 + e^{-\alpha \left(\frac{\delta_m^{max} - \delta_m^0}{\delta_f^0 - \delta_m^0} \right)} \left(1 + \frac{\delta_m^{max} \alpha}{\delta_f^0 - \delta_m^0} \right) \right\} \quad (4.35)$$

By substituting this equation into the remaining equations mentioned, the tangent stiffness matrix is achieved as follows

a) if $\delta_I > 0$

$$\mathbf{K}_{T,c} = \int \mathbf{B}_c^T \mathbf{D}(d(\mathbf{q})) \mathbf{B}_c d\Omega^d + \int \mathbf{B}_c^T \begin{bmatrix} -P & 0 & 0 \\ 0 & -P & 0 \\ 0 & 0 & -P \end{bmatrix} \left(\frac{\delta_m^0}{(\delta_m^{max})^2} + \left(\frac{1}{1 - e^{-\alpha}} \right) \left(\frac{\delta_m^0}{(\delta_m^{max})^2} \right) \left\{ -1 + e^{-\alpha \left(\frac{\delta_m^{max} - \delta_m^0}{\delta_f^0 - \delta_m^0} \right)} \left(1 + \frac{\delta_m^{max} \alpha}{\delta_f^0 - \delta_m^0} \right) \right\} \right) F(\delta - \delta_{max}) \frac{\delta^T}{\delta} \delta \begin{bmatrix} 1 & 0 & 0 \\ 0 & 1 & 0 \\ 0 & 0 & 1 \end{bmatrix} \mathbf{B}_c d\Omega^d \quad (4.36)$$

b) if $\delta_I < 0$

$$\mathbf{K}_{T,c} = \int \mathbf{B}_c^T \mathbf{D}(d(\mathbf{q})) \mathbf{B}_c d\Omega^d + \int \mathbf{B}_c^T \begin{bmatrix} -P & 0 & 0 \\ 0 & -P & 0 \\ 0 & 0 & 0 \end{bmatrix} \left(\frac{\delta_m^0}{(\delta_m^{max})^2} + \left(\frac{1}{1 - e^{-\alpha}} \right) \left(\frac{\delta_m^0}{(\delta_m^{max})^2} \right) \left\{ -1 + e^{-\alpha \left(\frac{\delta_m^{max} - \delta_m^0}{\delta_f^0 - \delta_m^0} \right)} \left(1 + \frac{\delta_m^{max} \alpha}{\delta_f^0 - \delta_m^0} \right) \right\} \right) F(\delta - \delta_{max}) \frac{\delta^T}{\delta} \begin{bmatrix} 1 & 0 & 0 \\ 0 & 1 & 0 \\ 0 & 0 & 0 \end{bmatrix} \mathbf{B}_c d\Omega^d \quad (4.37)$$

4.5 Contact

In the absence of proper contact constraints penetration of subdomains can occur. This issue arises particularly in non-linear buckling analyses. Hence, a simple frictionless contact formulation is developed within the XFEM formulation. In order to do so, the relative displacement of the debonded region is monitored during subsequent loading steps in the non-linear analysis. This can be performed by checking the value of the enhanced translational DOF in z direction a_w^0 . This parameter actually corresponds to the displacement jump in transverse direction. As soon as a negative value is reported, a penalty stiffness is included to bond the subdomains at the corresponding nodes. The contact force is given by

$$F_c = P a_w^0 \quad (4.38)$$

where F_c is the contact force and P is the contact penalty stiffness value. Note that the contact force is already included in the cohesive zone models.

In order to highlight the effect of the contact formulation in the post-buckling analysis, the deformed shape of the delaminated region is depicted in the last load step in presence and absence of the contact formulation in figure 4.7.

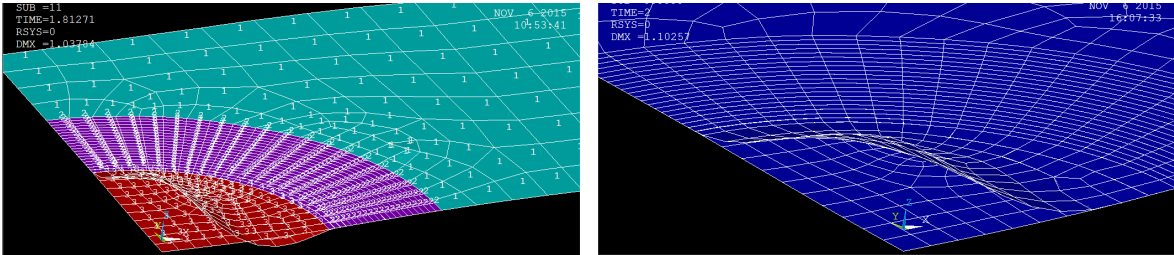


Figure 4.7: The importance of the contact formulation in the delamination buckling analysis.

When the contact constraint in this particular example is not active, the elliptical shape of the delamination surface in the pocket-like delamination is never traced. This is in conflict with the experimental reports and observations (see e.g. Bolotin (1996)).

4.6 Solution procedure and numerical integration

As it was mentioned earlier, a special non-linear technique should be utilized to solve the non-linear equation of cohesive formulation. Herein, the arc-length method with full Newton-Raphson algorithm that is available in ANSYS software is exploited (ANSYS Documentation, 2013). Therefore, one can smoothly control the solution and precisely follow the load-displacement path. However, the cohesive formulation suffers from instability problems. The instability can occur when the cohesive formulation of the delamination front is deleted and the structural displacement dramatically increases. As a result, the elements locating after the crack front experience the relative displacements that are larger than the final relative displacement of the cohesive zone model. Consequently, they are deleted without undergoing the softening behaviour. This problem is faced during the solution process and it was addressed by several authors so far (Hu et al., 2007; Elmarakbi et al., 2009; Hu et al., 2008). There are two commonly used approaches to control this issue: reducing the strength of interface while keeping the critical energy release rate constant or using a very fine mesh. Both methods are employed to increase the softening zone at the interface regions. This lets other elements to undergo the softening behaviour. It is noted that by employing the reduced strength, a drop in the maximum structural load-displacement appears for Mode I, e.g. DCB test. Turon et al. (2007) investigated the effect of cohesive parameters on the simulation outcomes. In the mentioned paper, the influences of penalty parameter, the mesh size, and the strength of interface are taken into account. It was proven that all the employed parameters in the constitutive equation must be chosen properly to achieve a fast convergence rate.

Apart from the aforementioned approaches that are considered as the general solutions to control the instability, there exist couples of modifications to acquire the stable solution by modifying the formulation of the cohesive zone model itself. These methods mostly deal with Mode I. For instance, Elmarakbi et al. (2009) suggested to add a pre-softening zone behind the delamination front to let them undergo softening behaviour during the loading process. Hu et al. (2007) defined a rigid wall to restrict the displacement of the separated layers and to avoid the large relative displacements. A viscous regulation firstly applied by Lapczyk and Hurtado (2007) to the damage parameter of cohesive formulation. The idea is to increase the time steps during the separation, especially at the tip of load-displacement diagram, to consequently get the converged results within a quasi-static simulation. Later, Hamitouche et al. (2008) applied a novel viscous regularization for the damage parameter to avoid instability problems. The idea was imposed for the cohesive element in shell theories by Dávila et al. (2008) as well.

Schellekens and de Borst (1992) studied the effect of the type of integration scheme on the stress prediction of interface elements by eigenmode analyses and showed the

superiority of the Newton-Cotes and Lobatto quadrature integration schemes. In the present work different integration schemes are investigated by relating their performance with the corresponding interface element. It is noted that the same bilinear shape functions are used as they are compatible with the first-order shear deformation theory. Therefore, the chosen integration schemes are introduced in the following subsections.

Gaussian quadrature

Gaussian quadrature is a well-known method with four integration points that are located at the so-called Gaussian points. This method has been used to calculate the tangent operator of the shell and the XFEM formulation in the previous sections. The Gaussian points are shown in figure 4.8 (a).

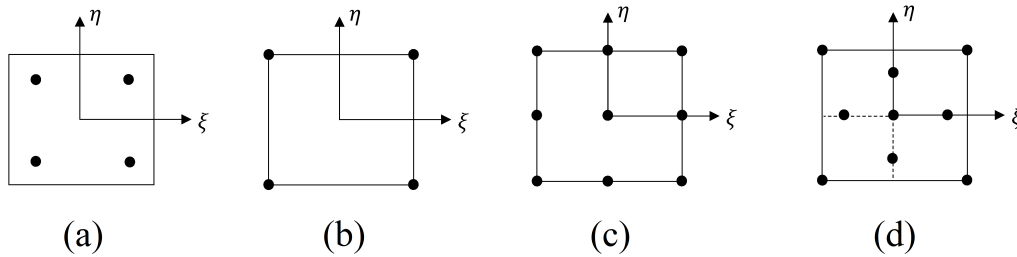


Figure 4.8: Schematic view of the integration schemes.

The number of integration points, the location of the integration points, and their weights are shown in table 4.1

Table 4.1: Location of the integration points and their weights in the Gaussian quadrature rule.

Number of integration points	Integration points (ξ_i, η_i)	Weights $\{w_i\}$
2×2	$(\pm\sqrt{3}/3, \pm\sqrt{3}/3)$	1

Newton-Cotes

This method contains four integration points which are located at the corners of an element. The schematic view of the integration points is shown in figure 4.8 (b). Table 4.2 shows the number of integration points, the location of the integration points, and their weights.

Table 4.2: Location of the integration points and their weights in the Newton-Cotes rule.

Number of integration points	Integration points (ξ_i, η_i)	Weights $\{w_i\}$
2×2	$(\pm 1, \pm 1)$	1

Lobatto quadrature (I)

This method contains nine integration points. The order of integration is three and it has been recommended in several publications for calculating the tangent stiffness in the interface elements (see e.g. Schellekens and de Borst (1992)). The schematic view of the integration points is shown in figure 4.8 (c). The number of integration points, the location of the integration points, and the corresponding weights were taken from Zwillinger (2012). They are provided in table 4.3.

Table 4.3: Location of the integration points and their weights in Lobatto quadrature (I) rule.

Number of integration points	Integration points (ξ_i, η_i)	Weights $\{w_i\}$
3×3	(0,0)	4/3
	(0,±1)	1/3
	(±1,0)	
	(±1,±1)	

Lobatto quadrature (II)

This method contains nine integration points and the order of this method is three. The schematic view of the integration points is shown in figure 4.8 (d). The number of integration points, the location of the integration points, and their weights are provided in table 4.4.

Table 4.4: Location of the integration points and their weights in Lobatto quadrature (II) rule.

Number of integration points	Integration points (ξ_i, η_i)	Weights $\{w_i\}$
3×3	(0,0)	- 8/9
	(0,±0.632455532)	10/9
	(±0.632455532,0)	
	(±1,±1)	1/9

4.7 Numerical tests

The formulations of mixed-mode cohesive zone models developed are verified by comparing the results obtained by the present model with available ones in literature. In the following, first, the bilinear cohesive formulation is verified; next, the linear-exponential one is examined. The geometry and material properties of the simulated laminates are presented in table 4.5.

Table 4.5: Geometrical dimensions and material properties of the studied plates.

	a (m)	b (m)	h (m)	t (m)	E_{11} (GPa)	E_{22} (GPa)	G_{12} (GPa)	ν_{12}	G_I^{cr} (J/m ²)	G_{II}^{cr} (J/m ²)	N (MPa)	S (MPa)	α
Plate 1	0.1	0.02	0.003	0.03	135.3	9.0	5.2	0.24	280	-	57	57	2
Plate 2	0.102	0.0254	0.00312	0.0393	122.7	10.1	5.5	0.25	-	1719	100	100	2
Plate 3	0.1	0.02	0.003	-	135.3	9.0	5.2	0.24	330	800	3.3	7	2

Bilinear cohesive zone model

First, a Double Cantilever Beam (DCB) test that is widely used for the analysis of pure Mode I is selected. The results are compared with the Virtual Crack Closure Technique (VCCT) of Alfano and Crisfield (2001). Plate 1 is depicted and the schematic view of the DCB test is shown in figure 4.9.

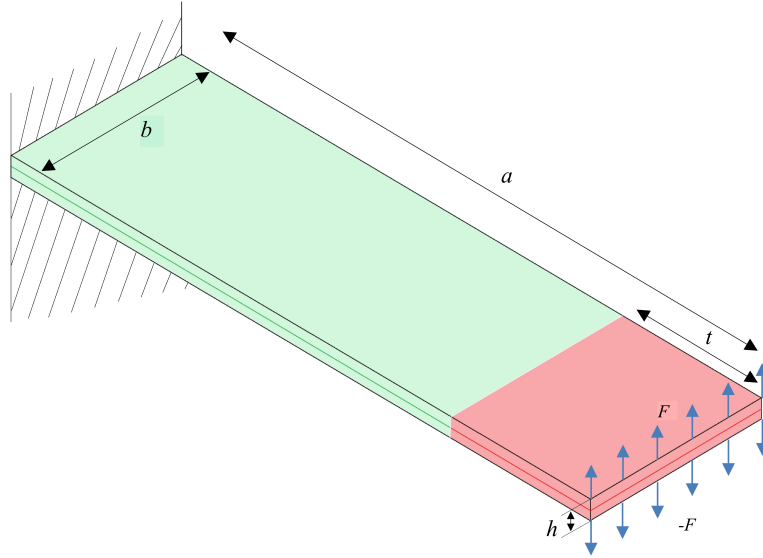


Figure 4.9: Schematic view of DCB test for pure Mode I.

The plate is clamped in one of the small edges whereas it is supposed to be free in the other ones. The fully debonded region at the edge - which is shown in red colour - is subjected to two equal loadings but in opposite directions. Classically, this test is performed through simulating two individual plates and the cohesive elements are inserted at the interface area. However, herein, the model consists of one plate and it has been discretised by four-node elements that are enriched by XFEM. In addition, the possibility to incorporate the cohesive formulation is given. Therefore, the displacement jumps at the interface are characterized by the enhanced DOFs. Hereupon, no simulation effort is demanded to model the debonded region. In the delaminated area with length t , the XFEM formulation is particularly inserted. However, in the initially bonded region of the same plane the XFEM and the interface formulation are combined. Therefore, the simulation of delamination propagation can be provided. Owing to the large penalty stiffness that is used in the linear regime of the cohesive formulation, the continuity of displacement field in the initially bonded region is supplied.

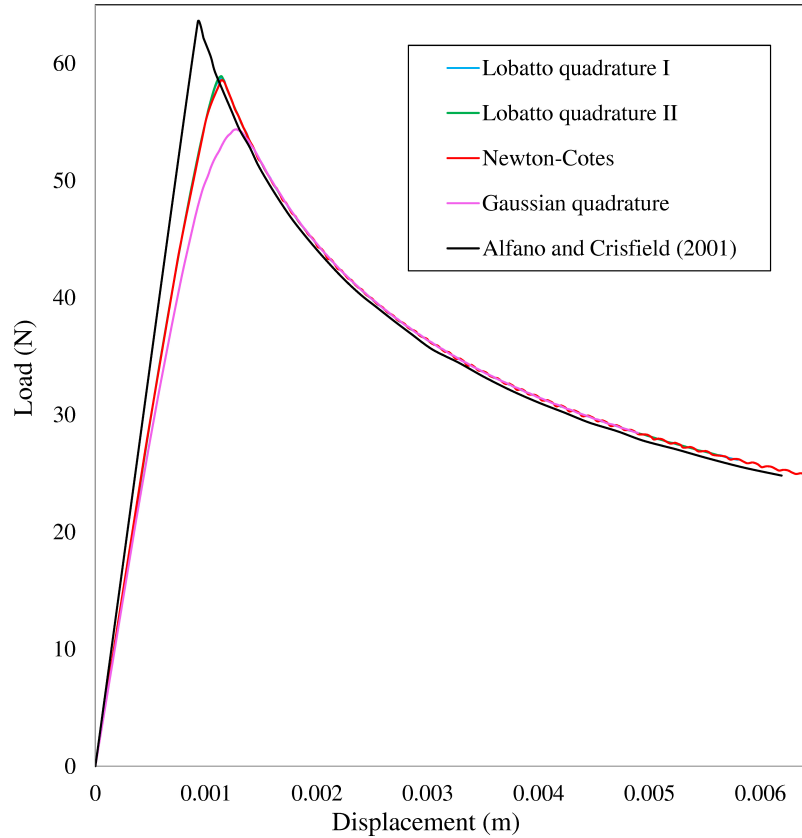


Figure 4.10: Load-displacement diagram of DCB test.

The elements with a length of 1 mm are used and the penalty parameter is assumed $P=5 \times 10^2 N/mm^3$. It is mentioned that the strength of interface for this particular study is reduced to 7 MPa to improve the instability problem that might encounter. The structural load-displacement diagram has been compared with the result of VCCT method in figure 4.10.

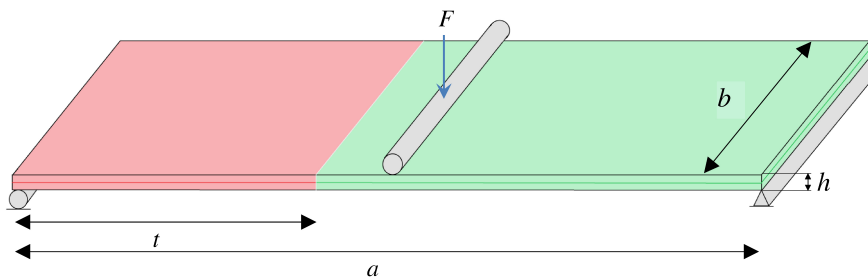


Figure 4.11: Schematic view of ENF test for pure Mode II.

There is a close agreement between the predicted results by the present model and the ones of Alfano and Crisfield (2001) in Mode I fracture test. When Lobatto quadrature rules are used to calculate the tangent stiffness in the cohesive zone model there is

an observable decrease in the computational time. Moreover, there is a better coordination in the predicted load-displacement diagrams and the reference. The predicted results by Newton-Cotes integration rule is close to the ones of Lobatto quadrature rules but efforts to obtain the converged solution resulted in an oscillatory response. It is noted that no significant performance difference is observed between Lobatto quadrature rules.

Second, End Notched Flexure (ENF) test that is used for pure Mode II is carried out. The results are compared with the meshfree penalty-based method of Barbieri and Meo (2009) and the experimental one of Camanho and Dávila (2002). The schematic view of the simulated test of Plate 2 is shown in figure 4.11.

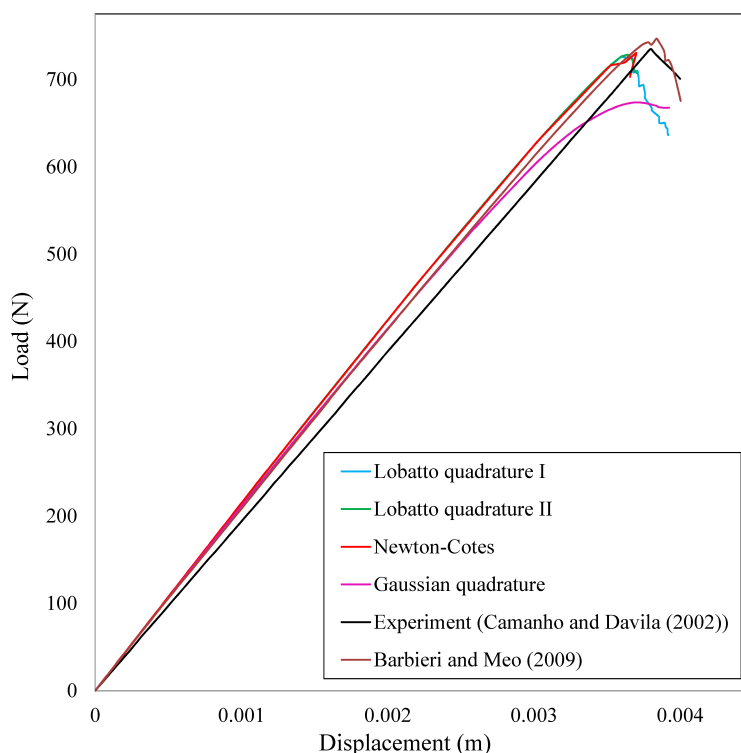


Figure 4.12: Load-displacement diagram of ENF test.

The boundary condition is supposed to be simply-supported at the two small edges at $x=-a/2$ and $x=a/2$ whilst the plate has movable edge at $x=-a/2$. The plate is subjected to a line load at the middle. A penalty parameter of $5 \times 10^3 N/mm^3$ is adopted. Different integration schemes are employed and the structural load-displacement diagrams are depicted in figure 4.12. In this particular case study, the length of arc in the non-linear solution is adopted sufficiently small to achieve the converged results.

A good performance is achieved for predicting the delamination growth behaviour of pure Mode II. The Lobatto quadrature rules perform better in comparison to the other integration topologies.

Next, the intact Plate 3 with lay-up orientation $[\theta/\theta/\theta/\theta]$ has been analysed. The plate is fully clamped at one of the small edges whereas it is subjected to two equal loads

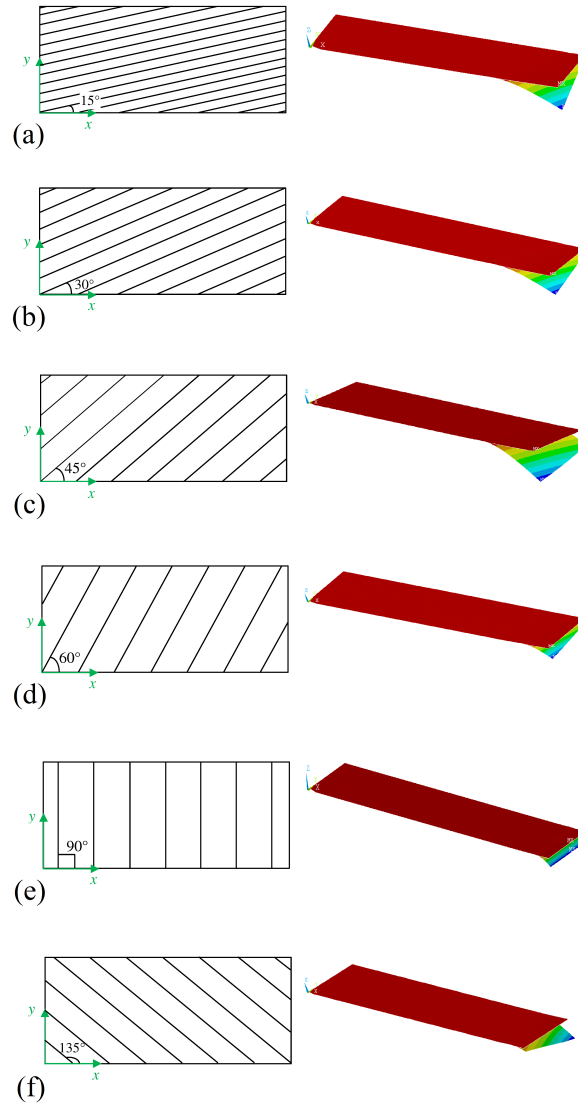


Figure 4.13: Deformed shape of Plate 3 with lay-ups: a) $[15^\circ/15^\circ/15^\circ/15^\circ]$; b) $[30^\circ/30^\circ/30^\circ/30^\circ]$; c) $[45^\circ/45^\circ/45^\circ/45^\circ]$; d) $[60^\circ/60^\circ/60^\circ/60^\circ]$; e) $[90^\circ/90^\circ/90^\circ/90^\circ]$; f) $[135^\circ/135^\circ/135^\circ/135^\circ]$.

but in opposite directions at the first interface of the edge in contrary location. The amplitude of load is increased to onset and to propagate the delamination. Henceforth, in the simulation process XFEM and cohesive formulations are inserted at the plane of the first interface. The fibre angle is altered as $\theta=15^\circ, 30^\circ, 45^\circ, 60^\circ, 90^\circ$, and 135° . The Lobatto quadrature rule for the integration of interface stiffness with element size of 1 mm has been adopted. The material properties of interface are taken from Alfano and Crisfield (2001) and a penalty parameter of $1 \times 10^2 N/mm^3$ is utilized. The deformed shapes of the composite plates in the last loading step are shown in figure 4.13.

As it is shown in figure 4.13, depending on the fibre orientation and consequently the local stiffness of plates, the delamination is initiated at different locations. This fact is

more obvious when one compares the cases (c) and (f). The aforementioned tests have similar lay-up orientations but in opposite directions. Accordingly, the delamination is initiated in the contrary locations. Apart from the plate with fibre angle $\theta=90^\circ$, the damage is initiated at one corner of the laminates.

In order to illustrate the effect of the fibre angle on the interlaminar strength of the laminate, the maximum response of delaminated region under the maximum applied load is reported in figure 4.14.

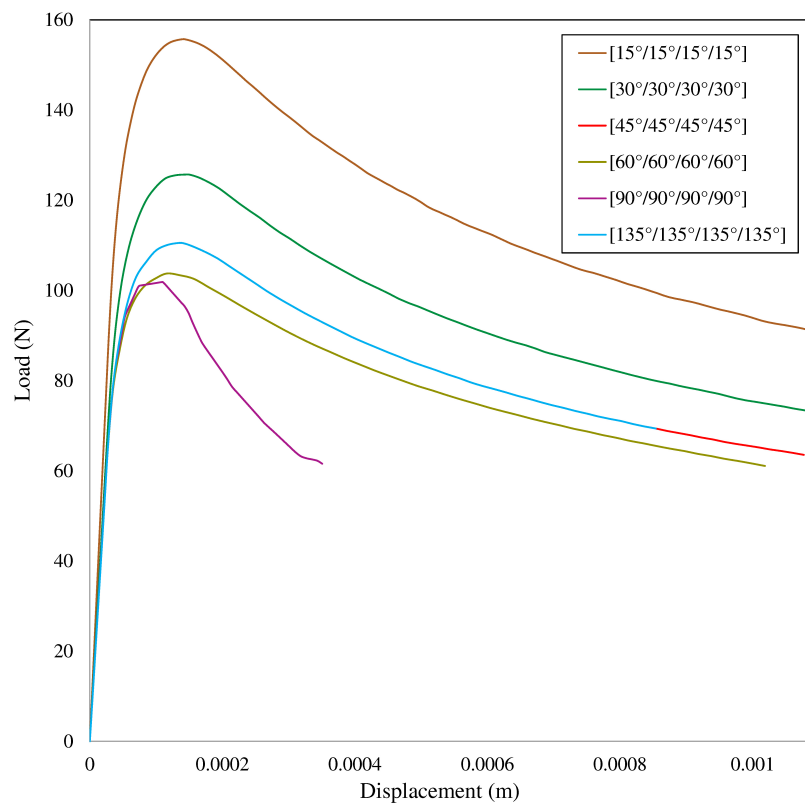


Figure 4.14: Load-displacement diagram of composite Plate 3 with various fibre orientations.

The load carrying capacity in a structure is reduced dramatically by increasing the fibre angle. In addition, less deflection is observed under the certain loading amplitude of laminates with tilted fibres. Therefore, one can conclude that based on the fibre angle of plies in composite laminates, the delamination is initiated at the corner where interlaminar stresses suddenly grow.

Linear-exponential cohesive zone model

The ability of the linear-exponential cohesive zone model to predict the delamination growth is examined. Therefore, the DCB test is chosen again; however, here the simulation is performed in the geometrically non-linear regime. This allows us to examine whether the subdomains undergo a non-linear behaviour or the non-linearity is solely associated to the fracture process. The material properties and geometrical

dimensions of the studied model are the ones of Plate 1 in table 4.5. The strength of interface is reduced to 7 MPa to facilitate obtaining converged results and the parameter α sets to value one. Furthermore, the integration scheme of the interface formulation is altered and the load-displacement diagrams of DCB are compared to the ones of Alfano and Crisfield (2001) in figure 4.15.

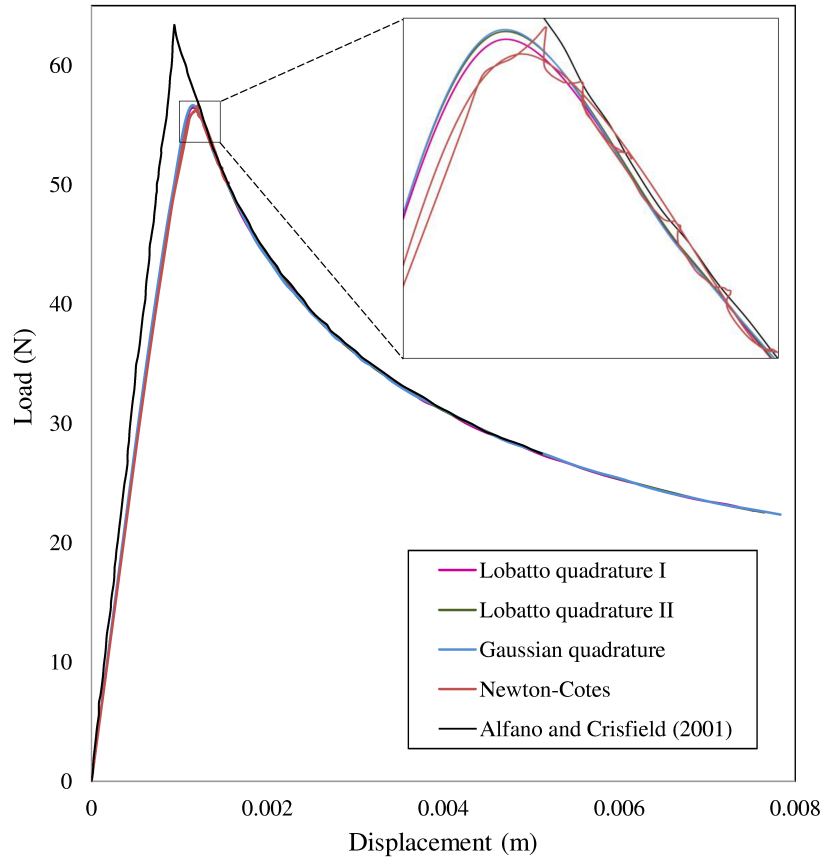


Figure 4.15: Load-displacement diagram of DCB test in geometrically non-linear regime.

The linear-exponential cohesive zone model illustrates excellent performance in the prediction of the delamination growth for a DCB problem. No significant difference is observed in the comparison of the predicted results in geometrically non-linear regime with those in linear regime that were discussed in the previous subsection. Thus, the non-linear response of the DCB test contributes to the fracture process. The oscillatory response of Newton-Cotes integration at the peak of the load-displacement diagram has been zoomed out. The computation time is reduced through the use of Lobatto quadrature rules. In the next example, Lobatto quadrature rule (I) is utilized for the numerical integration.

Next, the Mixed-Mode Bending (MMB) test is performed. Plate 2 is selected with G_{II}/G_T ratio equal to 0.8. The schematic view of MMB test is depicted in figure 4.16.

Finite elements with the length of 1 mm are used to discretise the domain. The

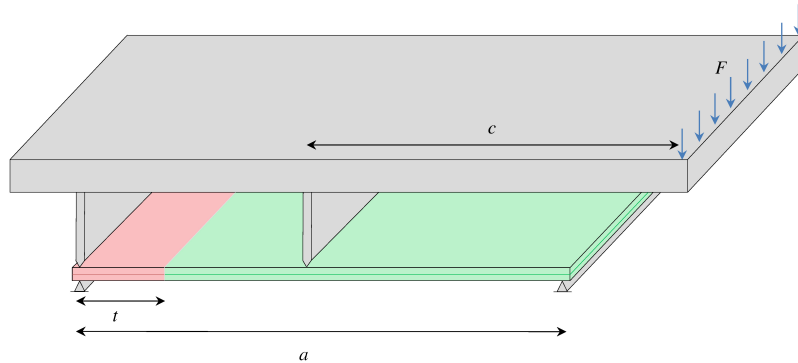


Figure 4.16: Schematic view of MMB test.

analysis is carried out in the geometrically linear regime and the reaction force versus the displacement at the loading point is shown in figure 4.17.

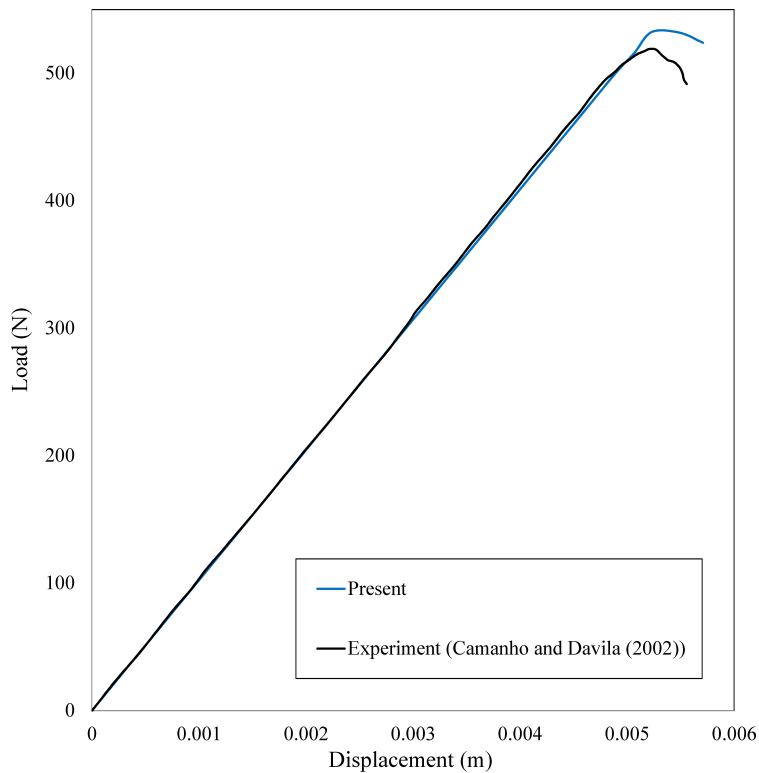


Figure 4.17: Load-displacement diagram of MMB test ($G_{II}/G_T=0.8$).

A good agreement is obtained for the delamination analysis of MMB test by comparing the predicted results with experimental ones of Camanho and Dávila (2002).

4.8 Closing remarks

Two cohesive zone models and a contact formulation have been developed in this chapter. The implementation aspects of the aforementioned theories to the XFEM topology were discussed. In addition, some numerical issues were discussed in order to increase the performance of these formulations in the non-linear analysis. For instance, different integration rules were applied to calculate the tangent stiffness matrix of cohesive zone model. In the verification studies of mode I and II fracture, the computation time was reduced by using Lobatto integration rule (I). Thus, this integration scheme is applied for the delamination analysis in the subsequent chapters. Furthermore, it is concluded that the geometrically non-linear behaviour has less influence on the delamination analysis of DCB test and the non-linearity is related to the fracture process particularity. However, one should not consider this fact as a general conclusion since the buckling phenomenon widely contributes to the response of the shell structures and for such analysis the geometrically non-linear terms have to be included. In the next chapter, all the formulations that have been developed so far are combined into a new algorithm for analysing the delamination in intact composite shells.

Chapter 5

Delamination onset and growth in composite shells

5.1 Introduction

The growing interlaminar stresses in the static loading test or the remaining traction forces in the impact test directly deal with delamination. In composite laminates with general lay-up the response of each individual ply to the loading is not unique; and thus, in-plane shear stresses are produced at the interfaces. Subsequently, interlaminar stresses occur at the bonded surfaces to hold the equilibrium in transverse direction (Gay et al., 2002). Thus, the delamination onset criterion is written based on the interlaminar stress distributions (Gruttmann and Wagner, 1996). At macroscale, strength-based criteria are widely used to detect the nucleation of delamination (Brewer and Lagace, 1988). They are established based on comparing the interlaminar stresses with the strength of interface that can be measured in experiment. Therefore, an important step in the delamination analysis is to accurately calculate the interlaminar stresses. However, the out-of-plane information in the plate and shell theories is nearly missed. Using the three-dimensional shell theories like solid-like shell or solid elements is also not successful since the dissimilar response of the shell at each ply sequence is not captured. Recently the composite laminates are simulated by a ply basis method which is called the layerwise theory. In this theory the displacement field is assigned for each ply independently and the transverse shear stresses can be calculated precisely. However, the transverse normal stress in the mentioned theory is missed. Here, two methods are proposed to recover these stresses: the interface model and the equilibrium equation. In both techniques the interlaminar stresses are retrieved in post-processing.

5.2 Recovery of interlaminar stresses using interface model

In order to achieve accurate information at the interface regions, one can develop an interface model and recover the stresses during post-processing. Therefore, the

frictionless adhesive contact formulation is applied at an arbitrary location where the relative displacements at interfaces are available. The adhesive contact can be enforced in the three-dimensional models such as the layerwise theories among individual layers of interest by the penalty method (Moorthy and Reddy, 1999). Another possibility is to formulate adhesive contact by means of the Lagrange multiplier method using e.g. domain decomposition methods (Fagianio et al., 2010). According to the XFEM formulation implemented to discretise the first-order shear deformation theory, the adhesive is formulated using extra DOFs. The model can be employed for both the linear and the geometrically non-linear application and can be efficiently used to recover the interlaminar stress distributions. The implementation aspect is the same as the one of cohesive zone model but here the softening behaviour is excluded. Therefore, the constitutive equation of interface model reads as

$$\begin{Bmatrix} \tau_{xz} \\ \tau_{yz} \\ \sigma_{zz} \end{Bmatrix} = \mathbf{P}\boldsymbol{\delta} = \begin{bmatrix} P & 0 & 0 \\ 0 & P & 0 \\ 0 & 0 & P \end{bmatrix} \begin{Bmatrix} \delta_x \\ \delta_y \\ \delta_z \end{Bmatrix} \quad (5.1)$$

Since the equation is linear, the stiffness matrix can be derived as

$$\mathbf{K}_{int} = \int \mathbf{B}_c^T \mathbf{P} \mathbf{B}_c d\Omega^d \quad (5.2)$$

This formulation can be inserted at any location through the thickness of laminate; and based on the small values of penetration or sliding of the subdomains, the interlaminar stresses can be retrieved at the corresponding interface. The calculated normal and transverse stresses by this method are precise. Since the simulation is performed several times by inserting the aforementioned formulation at each particular interface, the computational cost is relatively high. The verification studies of the present formulation are carried out in section 5.6.

5.3 Recovery of interlaminar stresses using equilibrium equation

As it was mentioned earlier, the piecewise parabolic distribution of transverse stresses in the first-order shear deformation theory is not modelled. However, the interlaminar shear stresses can be calculated precisely by using the constitutive equation of first-order shear deformation theory and the derivatives of some warping functions (Schürg et al., 2009). In addition, these stresses can be recovered in post-processing using the equilibrium equation of elasticity. Therefore, transverse shear stresses can be calculated from

$$\begin{aligned} \tau_{xz} &= - \int_{z_0}^z \left(\frac{\partial \sigma_x}{\partial x} + \frac{\partial \tau_{xy}}{\partial y} \right) dz + \psi(x, y) \\ \tau_{yz} &= - \int_{z_0}^z \left(\frac{\partial \sigma_y}{\partial y} + \frac{\partial \tau_{yx}}{\partial x} \right) dz + \psi(x, y) \end{aligned} \quad (5.3)$$

where $\psi(x, y)$ is defined according to the boundary conditions or the stress values at the reference point. In equation 5.3 the first derivatives of in-plane stresses are calculated and to do so the second derivatives of displacement field are required. Since the displacement field of each element is interpolated by bilinear shape functions and the second derivatives of them is almost zero, these functions fail to compute the partial derivatives of in-plane stresses. Thus, a simple method is to compute the stresses by using a numerical differentiation of the computed in-plane stresses in x and y directions with respect to the adjacent elements. An alternative method is to utilize a hierarchic interpolation of displacements (Kuhlmann and Rolfes, 2004). Here another technique is proposed to compute the derivatives by using the interpolation function itself. The detailed procedure is explained in the following. Then, having the interlaminar shear stresses computed, one can calculate the interlaminar stress in the normal direction using the equilibrium equation in z direction

$$\sigma_{zz} = - \int_{z_0}^z \left(\frac{\partial \sigma_{xz}}{\partial x} + \frac{\partial \tau_{yz}}{\partial y} \right) dz + \psi(x, y) \quad (5.4)$$

In this thesis, a technique to smooth the stress values and to recover the interlaminar stresses in the post-processing analysis is discussed.

The continuity of displacement field is imposed by using the bilinear interpolation functions that have C_0 continuous property. However, this leads to a discontinuous stress field. In order to avoid this discontinuity and to obtain acceptable results for stresses, several methods exist that are mostly based on post-processing techniques. Zienkiewicz and Zhu (1987) proposed to approximate the stress values by the same interpolation functions as the displacements. Thus, stress projections are calculated that are one order higher than the linear approximation and they are more accurate. Similarly Simo (1988) applied the row sum lumping technique to diagonalize the projection matrix for obtaining the smoothed nodal stress values.

One principal technique is to compute averaged stress values of the elements sharing one node among each other. By doing so, the jumps of stress values are smoothed. This enhancement procedure results in the reduction of errors between the real values of stress and the ones that are approximated by finite element analysis, especially on the boundaries of laminates that is of importance for the delamination analysis. The schematic view of discontinuous and smoothed stress distribution is shown in figure 5.1.

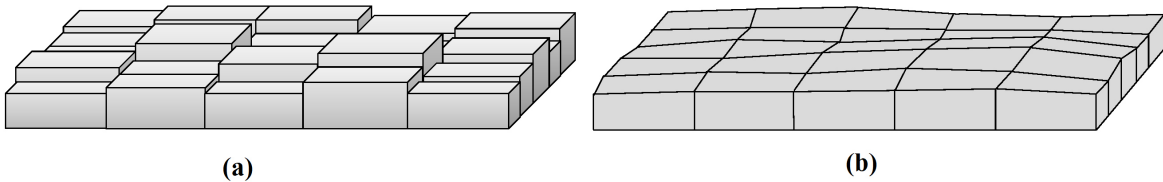


Figure 5.1: Stress distribution in elements: (a) discontinuous distribution; (b) smoothed distribution.

In order to calculate the stresses at nodal points, one extrapolation of the results of

the integration points to the nodal points is required. The extrapolation can be done by using the following transformation relation in the local non-dimensional coordinate system of each element

$$\xi = \frac{\xi'}{\sqrt{3}}, \eta = \frac{\eta'}{\sqrt{3}} \quad (5.5)$$

where ξ' and η' should be replaced by ξ and η in the interpolation functions to calculate the nodal values of stresses. Therefore, the typical bilinear interpolations that are used in the extrapolation process are presented as

$$\begin{aligned} N_1^e &= \frac{1}{4} (1 - \sqrt{3}\xi) (1 - \sqrt{3}\eta) \\ N_2^e &= \frac{1}{4} (1 + \sqrt{3}\xi) (1 - \sqrt{3}\eta) \\ N_3^e &= \frac{1}{4} (1 + \sqrt{3}\xi) (1 + \sqrt{3}\eta) \\ N_4^e &= \frac{1}{4} (1 - \sqrt{3}\xi) (1 + \sqrt{3}\eta) \end{aligned} \quad (5.6)$$

The in-plane stress values of integration points are extrapolated using the new functions that are defined in equation 5.6. It is noted that the position of each specific nodal point in the local coordinate system (± 1 for ξ and η) should be substituted into equation 5.6. Thus, any quantity, including the in-plane stresses, can be extrapolated using the following equation

$$\begin{Bmatrix} w_1 \\ w_2 \\ w_3 \\ w_4 \end{Bmatrix} = \begin{bmatrix} 1 + \sqrt{3}/2 & -1/2 & 1 - \sqrt{3}/2 & -1/2 \\ -1/2 & 1 + \sqrt{3}/2 & -1/2 & 1 - \sqrt{3}/2 \\ 1 - \sqrt{3}/2 & -1/2 & 1 + \sqrt{3}/2 & -1/2 \\ -1/2 & 1 - \sqrt{3}/2 & -1/2 & 1 + \sqrt{3}/2 \end{bmatrix} \begin{Bmatrix} w'_1 \\ w'_2 \\ w'_3 \\ w'_4 \end{Bmatrix} \quad (5.7)$$

where w_i ($i=1$ to number of nodes) and w'_j ($j=1$ to number of integration points) are values of the quantity w at nodes and integration points, respectively. Taking the advantage of the smoothing technique that is used to calculate the nodal stress values, one can compute the transverse stresses at the integration points. Therefore, a further interpolation of the averaged stresses from the nodal points to the integration points is required. By doing so, the derivatives of equation 5.3 can be performed and the transverse stresses at the integration points are calculated.

The same process can be carried out to calculate the normal stress, using the smoothed interlaminar shear stresses. Since the smoothed transverse shear stresses are used in equation 5.4, the obtained transverse normal stresses are not precise. However, they can be applied in the delamination onset criterion to reliably predict the location of delamination onset at a corresponding load level. The verification study of this method is available in section 5.6.

5.4 Prediction of delamination onset

The criterion, proposed by Gruttmann and Wagner (1996), is chosen for the delamination onset. It is defined as

$$\begin{cases} \frac{\tau_{xz}^2 + \tau_{yz}^2}{S^2} + \frac{\sigma_{zz}^2}{N^2} = 1 & \sigma_{zz} > 0 \\ \frac{\tau_{xz}^2 + \tau_{yz}^2}{S^2} = 1 & \sigma_{zz} < 0 \end{cases} \quad (5.8)$$

where N and S are the strength of interface in the normal and shear direction, respectively. In the non-linear analysis, the calculation of interlaminar stresses is performed at the end of each converged load step, using the procedure that was explained in the previous section. Then, the delamination onset criterion can be evaluated at each integration point throughout the thickness of the multi-layered laminate. As soon as any potential point is detected, the formulation of the associated element and the neighbouring ones are immediately altered by the XFEM and cohesive formulations. Therefore, the location of delamination in thickness direction z_d is fixed for those element in the subsequent analysis. By doing so, the delamination growth at that particular location and interface can be traced.

5.5 Solution procedure

Within the solution procedure, the Newton-Raphson's method is used. By performing the linearization of the contributed formulations one arrives at three distinct tangent operators related to the shell, the cohesive model, and the contact formulation. These operators can be combined within the analysis. The tangent stiffness matrix of the shell is applied to simulate intact and delaminated shell structures in the linear and geometrically non-linear regime. The most challenging part of the simulation of delamination in multi-layered laminates is related to the location of delamination onset. Here the simulation is started using an intact laminated shell. During that part of analysis the extra DOFs do not contribute to the shell formulation. After each converged sub-step during the non-linear analysis the interlaminar stresses are computed using post-processing and the delamination criterion is surveyed at the interfaces and all integration points. Whenever the delamination criterion monitors an onset of delamination at a particular load level, the entire formulation of the related element and the surrounding ones are replaced by the discontinuous shell and cohesive formulation for the next loading steps. In addition, to track the delamination growth in the adjacent elements the aforementioned updating for surrounding elements is performed when the softening behaviour of already delaminated element is traced. Therefore, the simulation of delamination growth can be triggered locally within the non-linear solution. The delamination onset criterion identifies critical locations as well as a specific interface at which the delamination might occur (x, y, z_d) . Thus, z_d is set and the Heaviside function activates the enhanced DOFs for the upper subdomain. Consequently, the

possibility of the contribution of cohesive formulation is provided. The present model is compared with the standard simulation of delamination using finite element method in figure 5.2.

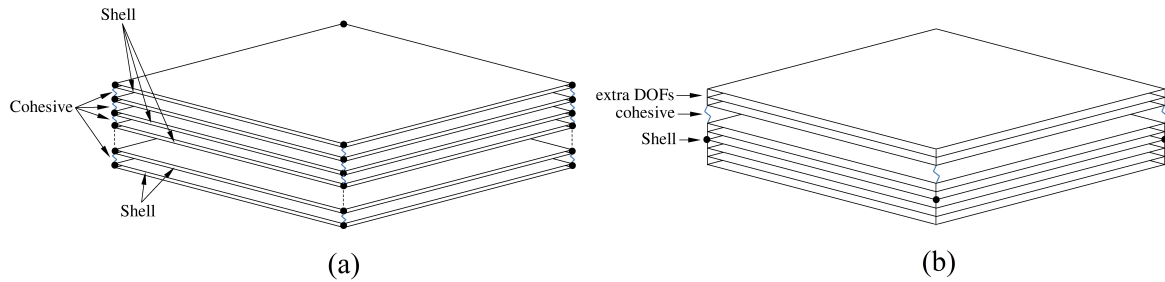


Figure 5.2: Simulation of delamination: (a) standard finite element analysis, (b) present model.

All developed formulations and the algorithm were coded as an element routine in ANSYS version 14.5. In order to trace snap-back and snap-through in the non-linear analysis of shell and cohesive formulation, the arc-length method available in ANSYS is employed.

Owing to the lower order finite element that is used in the developed flat-shell formulation and taking into account the four-node elements that are used to discretise the domain, the formulation is robust in the non-linear analysis (Wriggers, 2008). During the non-linear analysis the delamination front is formed without remeshing. The computational cost is low because the cohesive formulation and the discontinuity are inserted in the vicinity of the local defect to simulate the delamination propagation under increasing load. In the present contribution the possibility of modelling multiple delaminations is restricted to different regions, see figure 5.3.

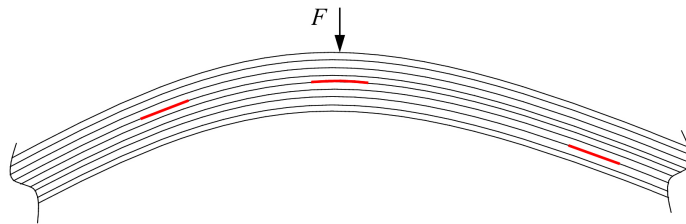


Figure 5.3: The application of proposed theory for local delamination analysis.

Therefore, the crack front is artificially formed once the coalescence of delamination in different interfaces is detected. It is worth pointing out that the perturbation load that is used in the analysis of buckling-driven delamination is replaced by applying forces related to extra DOFs that produce a deformation proportional to the delamination buckling mode. In chapter 8, a few general case studies are performed to examine the present algorithm for intact shells.

5.6 Numerical tests

In what follows, the precision and accuracy of the described approaches for calculating the interlaminar stresses are demonstrated. The model is verified for various loading and boundary conditions in the linear and the geometrically non-linear regime. The material properties and the geometrical dimensions of the studied plates with their names are shown in table 5.1.

Table 5.1: Geometrical dimensions and material properties of plates in the interlaminar stress analysis.

	a	b	h	E_{11}	E_{22}	G_{12}	G_{13}	G_{23}	ν_{12}
Plate 1	1 m	1 m	0.02 m	25 GPa	1 GPa	0.5 GPa	0.5 GPa	0.2 GPa	0.25
Plate 2	1 m	Infinite	0.0012 m	155 GPa	12.1 GPa	4.4 GPa	4.4 GPa	3.2 GPa	0.248
Plate 3	$20h$	$2h$	$4h_k$	20 Mpsi	2.1 Mpsi	0.86 Mpsi	0.86 Mpsi	0.86 Mpsi	0.21

5.6.1 Interface model

Plate 1 with fibre angle $[0^\circ]$ is chosen. The plate is considered to be fully clamped at its edges while it is subjected to the uniform transverse distributed load. The amplitude of load is altered within several tests and the interlaminar stresses are obtained in the geometrically non-linear regime. Different convergence patterns are selected in order to determine the precision of model. Furthermore, the results are compared with the layerwise theory of Yazdani and Ribeiro (2014) and FSDT of Turvey and Osman (1991). Equation 5.9 is used to present the results in the non-dimensional form and they are reported in table 5.2.

$$\bar{q} = \frac{q_0 a^4}{E_{22} h^4} \quad \bar{\sigma}_i = \frac{\sigma_i a^3}{E_{22} h^3} \quad i = xz, yz, zz \quad (5.9)$$

A very good convergence order is demonstrated with the present formulation in the non-linear regime. Taking into account the results of the finest mesh as reference, the relative errors are calculated with respect to them in percentage in brackets. The relative difference, at most, is equal to 0.2% between the element size 2.5 cm and 0.625 cm. As a result, one might attain the precised results from the present formulation with a normal element size; and consequently, less computational effort is needed. A better correlation in the tabulated results is observed with the layerwise theory in the lower pressure amplitudes. However, by increasing the load, the differences between the aforementioned methods get noticeable. In the next example, the present approach is compared with an analytical formulation.

In the second example, an infinite cross-ply plate is assumed with fibre orientations $[0^\circ/90^\circ]_{2s}$. The laminate is partially subjected to the uniformly distributed pressure load $q_0=2.5$ Pa on the top surface while it is pinned at the edges. Henceforth, in the XFEM scheme, both normal and extra DOFs are constrained in y and z directions along the edges. The uniform pressure is applied partially at the centre of the laminate

Table 5.2: Convergence study on the non-linear interlaminar stresses of Plate 1.

\bar{q}	Theory	Element number	$\bar{\tau}_{xz} (-a/2,0,0)$	$\bar{\tau}_{yz} (0,-b/2,0)$	$\bar{\sigma}_{zz} (0,0,0)$
1	Present	40×40	0.7427 (0.054%)	0.2119 (0.19%)	-0.01003 (0.1%)
		80×80	0.7424 (0.013%)	0.2116 (0.047%)	-0.01003 (0.1%)
		120×120	0.7423	0.2115	-0.01003 (0.1%)
		160×160	0.7423	0.2115	-0.01002
	Layerwise	-	0.7282	0.2664	-
	FSDT	-	0.6100	0.2350	-
10	Present	40×40	7.4269 (0.057%)	2.1191 (0.2%)	-0.1029 (0.097%)
		80×80	7.4236 (0.012%)	2.1161 (0.057%)	-0.1029 (0.097%)
		120×120	7.4229 (0.002%)	2.1152 (0.014%)	-0.1029 (0.097%)
		160×160	7.4227	2.1149	-0.1028
	Layerwise	-	7.2211	2.6639	-
	FSDT	-	6.1250	2.3550	-
20	Present	40×40	14.8523 (0.057%)	4.2381 (0.2%)	-0.2116 (0.095%)
		80×80	14.8456 (0.011%)	4.2321 (0.057%)	-0.2116 (0.095%)
		120×120	14.8443 (0.003%)	4.2303 (0.014%)	-0.2116 (0.095%)
		160×160	14.8439	4.2297	-0.2114
	Layerwise	-	14.312	5.3343	-
	FSDT	-	12.260	4.7150	-
30	Present	40×40	22.2746 (0.057%)	6.3571 (0.2%)	-0.3261 (0.092%)
		80×80	22.2644 (0.011%)	6.3479 (0.057%)	-0.3261 (0.092%)
		120×120	22.2625 (0.003%)	6.3452 (0.014%)	-0.3261 (0.092%)
		160×160	22.2619	6.3443	-0.3258
	Layerwise	-	21.2797	8.0207	-
	FSDT	-	18.400	7.0700	-
40	Present	40×40	29.6924 (0.057%)	8.4758 (0.2%)	-0.4463 (0.045%)
		80×80	29.6787 (0.011%)	8.4636 (0.058%)	-0.4463 (0.045%)
		120×120	29.6762 (0.003%)	8.4600 (0.015%)	-0.4463 (0.045%)
		160×160	29.6753	8.4587	-0.4461
	Layerwise	-	28.134	10.733	-
	FSDT	-	24.555	9.4300	-
50	Present	40×40	37.1044 (0.059%)	10.5944 (0.2%)	-0.5721 (0.052%)
		80×80	37.0870 (0.012%)	10.5790 (0.058%)	-0.5721 (0.052%)
		120×120	37.0838 (0.003%)	10.5744 (0.014%)	-0.5721 (0.052%)
		160×160	37.0826	10.5729	-0.5718
	Layerwise	-	34.885	13.479	-
	FSDT	-	30.735	11.795	-
60	Present	40×40	44.5092 (0.06%)	12.7127 (0.2%)	-0.7036 (0.042%)
		80×80	44.4881 (0.012%)	12.6941 (0.058%)	-0.7036 (0.042%)
		120×120	44.4841 (0.003%)	12.6886 (0.015%)	-0.7036 (0.042%)
		160×160	44.4827	12.6867	-0.7033
	Layerwise	-	41.544	16.270	-
	FSDT	-	36.930	14.160	-

with the span equal to 0.2 m. The schematic view of the studied laminate is shown in figure 5.4.

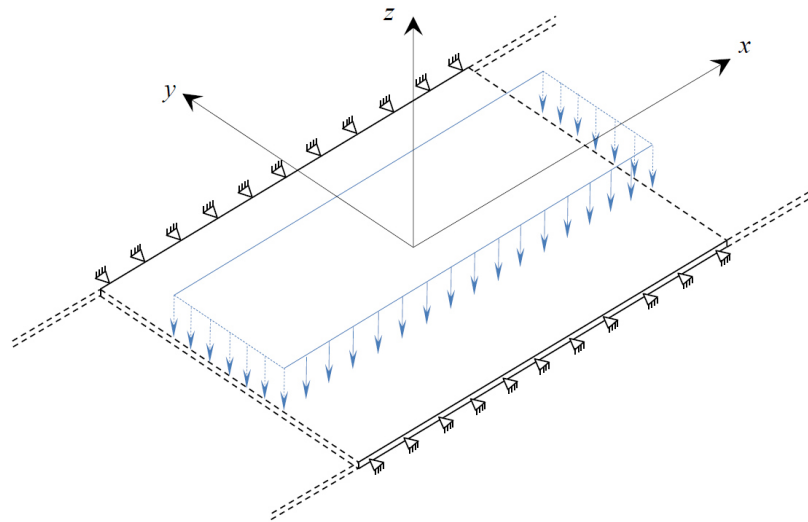


Figure 5.4: Schematic view of the Plate 2.

It is noted that the infinity length of the plate along x direction is simulated through a finite length in which the displacement and rotational DOFs in x and y directions, respectively, were taken for both the normal and enhanced DOFs. The element size is considered to be 0.05 m. The interlaminar stresses in the geometrically non-linear regime are compared with the analytical results of Hartman et al. (2011) in figure 5.5.

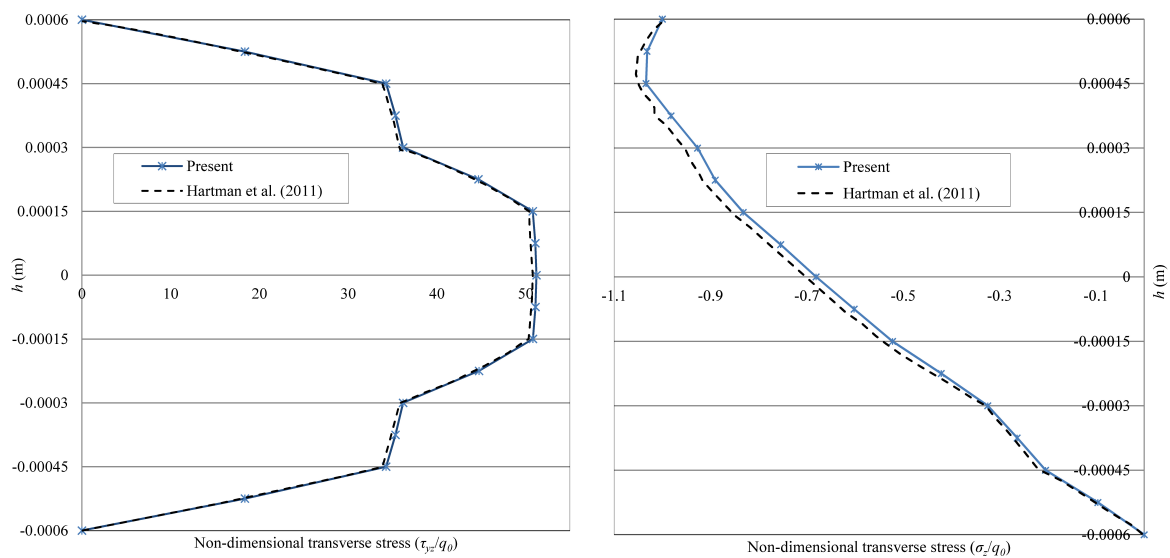


Figure 5.5: Non-dimensional non-linear interlaminar stresses of Plate 2 at $y=0.05$ m.

Excellent agreement is observed between the present approach and the analytical

solution reported in Hartman et al. (2011). In the next example, interlaminar stresses are verified for a plate under in-plane tensional load.

The recovery of interlaminar stresses using post-processing provokes oscillations in their distributions. Hence, smoothing technique is required to reduce the oscillations (Moorthy and Reddy, 1999). However, in the present formulation within the XFEM framework, a smooth stress distribution is achieved. This case study is performed to compare the present method with the layerwise theory of Robbins and Reddy (1993) in the linear regime. Plate 3 with stacking sequence $[45^\circ / -45^\circ]_s$ is subjected to the axial displacement. It is assumed that each layer is of equal thickness h_k . The boundary conditions are defined as

$$u(-a/2, y, z)=0, a_u(-a/2, y, z)=0, v(-a/2, y, z)=0, a_v(-a/2, y, z)=0,$$

$$v(a/2, y, z)=0, a_v(a/2, y, z)=0, w(x, y, z)=0, u(a/2, y, z)=u_0$$

The linear interlaminar stress τ_{xz} is obtained at the location $z=0.0025$ m and is compared with the one of layerwise theory at $z=0.00314$ m. The stresses are non-dimensionalized by equation 5.10 and they are depicted in figure 5.6.

$$\bar{\tau}_{xz} = 20 \frac{\tau_{xz}}{\epsilon_0} \frac{1}{E_{11}} \quad (5.10)$$

As it is shown, based on our XFEM formulation a smooth stress distribution is achieved within the plane of the laminate. The difference between the stress distributions corresponds to the location where the stresses are achieved.

5.6.2 Equilibrium equation model

The interlaminar stresses of the infinite cross-ply Plate 2 is analysed in this subsection. The equilibrium equation is used to calculate the interlaminar stresses in the post-processing. The calculation is carried out after achieving the converged solution. Thus, as what explained in section 5.3 the in-plane stresses at the Gaussian integration points and each individual ply are calculated. It is noted that because of different fibre orientation, and subsequently different constitutive equation at each interface, two in-plane stress values might be obtained and both of them should be used. Next, the in-plane stresses are extrapolated to the nodal points where the average of them is computed. The smoothed values are inserted into the equation 5.3 to calculate the interlaminar stresses at integration points. Thus, the derivatives of in-plane stresses in x and y directions are evaluated in the non-dimensional coordinate system, using the shape functions. It is noted that the calculations are performed from the bottom of the lowest layer ($z_0=-h/2$) in that no boundary condition exists and hence $\psi(x, y)$ is preassumed zero. Continuing the same procedure for the subsequent interfaces through-the-thickness of the laminate might automatically satisfy the boundary condition at the top surface. In this specific example, the interlaminar shear stress value vanishes

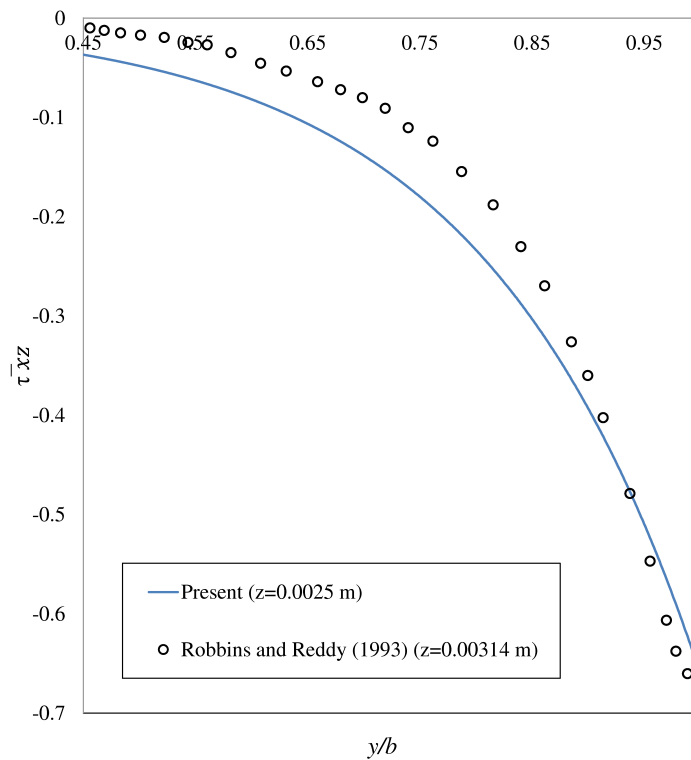


Figure 5.6: Non-dimensional linear stress distribution $\bar{\tau}_{xz}(-0.0115, y, 0.0025)$ of Plate 3.

at the top surface. The transverse shear stress distribution at $y= 0.05$ m is depicted in figure 5.7.

As it is shown in figure 5.7, the results correlate very well with the analytical ones of Hartman et al. (2011).

The interlaminar normal stresses are calculated in the next step, using the equilibrium equation in z direction. The computed normal stress distribution is shown in figure 5.8.

As it was mentioned earlier, the calculated normal stresses are not necessarily precise, but they can be applied in the delamination onset criterion as the predictor of the location of delamination.

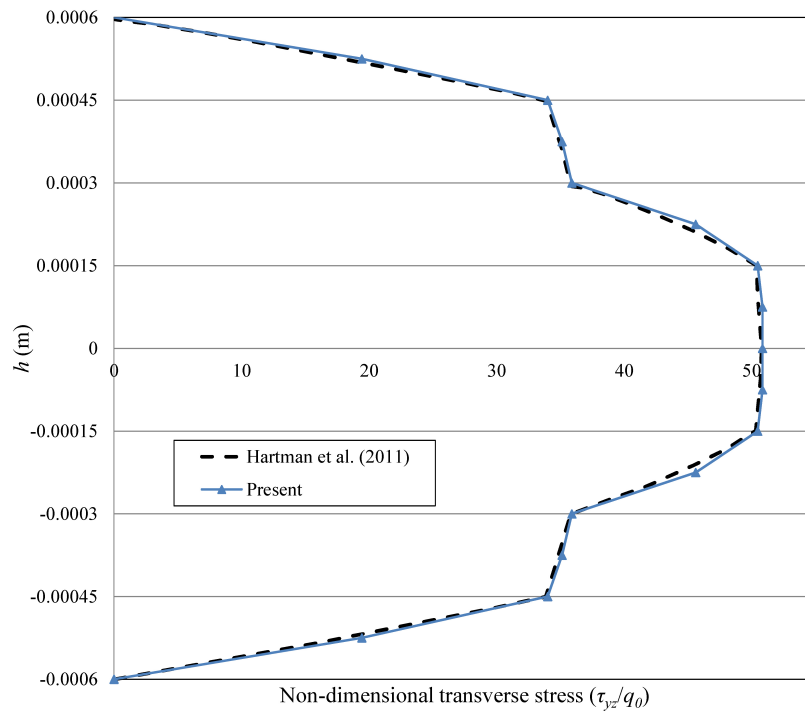


Figure 5.7: Non-dimensional non-linear transverse stresses of Plate 2 at $y=0.05$ m.

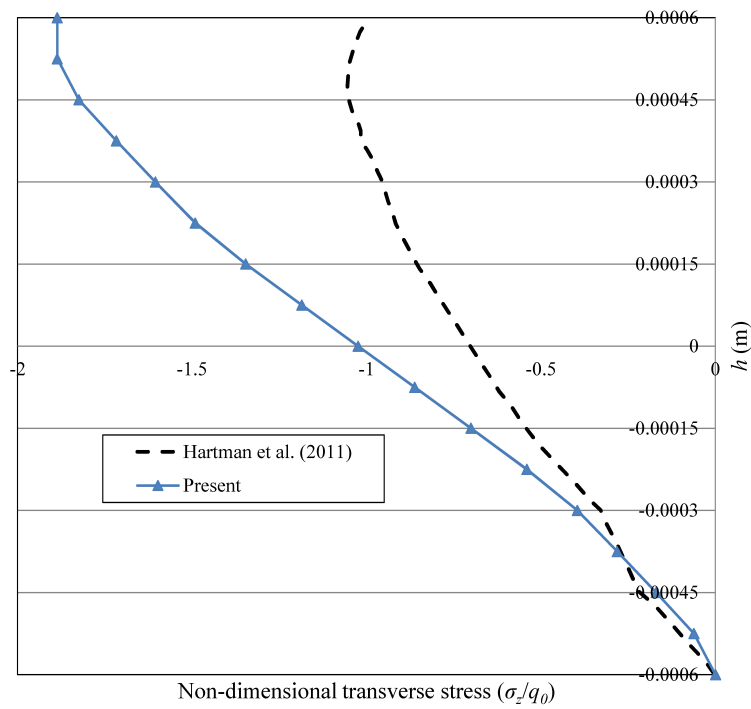


Figure 5.8: Non-dimensional non-linear normal stresses of Plate 2 at $y=0.05$ m.

5.7 Closing remarks

The aim of this chapter was to propose a new algorithm to reduce the computation cost of the delamination analysis. This algorithm is based on evaluating the delamination onset criterion during the loading to activate the cohesive zone model for the critical locations, particularly. Two methods were proposed for calculating the interlaminar stress distribution in laminates. The first method takes advantage of interface formulation to calculate the interlaminar stresses whereas in the second one the equilibrium of elasticity is used to recover the interlaminar stresses. The former is computationally expensive because the same example should be accomplished several times to obtain a sufficient information through the thickness of laminate. However, in the latter, the distribution of stresses in the out-of-plane direction is obtained in only one step. In the next chapter, the buckling and the delamination buckling analysis of composite shells are described.

Chapter 6

Buckling analysis

6.1 Linear buckling analysis

The geometric non-linearity contributes to the response of beam, plate, and shell structures. Hence, during the loading process any small change in a certain loading amplitude may lead to a large response of the structure. In the mentioned structures, once the additional loading amplitude is not sustained by the membrane component, it is partially converted to the bending format to establish a new equilibrium configuration. This sudden change may lead to the release of energy; and subsequently, the reduction of stiffness that is followed by the collapse of the structure. The point in that these changes occur is called the instability point (Wriggers, 2008). From the mathematical point of view the tangent matrix becomes singular at this point. In other words, the determinant of the tangent matrix is zero. Thus, the following eigenvalue problem can be established

$$(\mathbf{K}_T - \lambda_i \mathbf{I}) \phi_i = \mathbf{0} \quad (6.1)$$

where λ_i is the eigenvalue and ϕ_i is the corresponding eigenvector of each particular eigenmode.

The linear buckling analysis is based on a linear perturbation analysis that is performed to find the onset of instability. The first critical buckling load determines the first loading amplitude in that the structure becomes unstable. This analysis is usually practical for slender structures which experience small deformations. In these structures the load is carried in the axial direction through the membrane component, particularly. For the linear buckling analysis the tangent stiffness matrix can be split into the linear and non-linear part. Therefore, the tangent stiffness can be written as

$$\mathbf{K}_T = \mathbf{K}_L + \mathbf{K}_U + \mathbf{K}_\sigma \quad (6.2)$$

where \mathbf{K}_L is the linear stiffness matrix, \mathbf{K}_U is the non-linear part of stiffness matrix that is related to the initial deformation, and \mathbf{K}_σ is the other non-linear part that is so-called the geometric stiffness matrix. Hence, the linear eigenvalue analysis can be formulated as follows

$$(\mathbf{K}_L + \lambda_i (\mathbf{K}_\sigma)) \phi_i = \mathbf{0} \quad (6.3)$$

where λ_i is the critical load factor whereas ϕ_i is the corresponding mode shape. In the linear buckling analysis it is optional to include the part of stiffness matrix that is related to the initial deformation in the eigenvalue analysis. However, here, in order to lessen the dependency of results to the initial deformation of structure, only the geometric stiffness matrix is taken into account. By doing so, the predicted results for the critical buckling load might not noticeably be changed. It is noted that depending on the type of analysis, normal and extra DOFs may be combined into the eigenvalue analysis. To compute the ideal critical buckling load and the corresponding mode shape, the magnitude of the initially applied load \mathbf{P} is multiplied by the critical load factor

$$\mathbf{P}_c = \lambda_c \mathbf{P} \quad \text{and} \quad \phi_c = \lambda_c \phi \quad (6.4)$$

In order to perform an eigenvalue analysis two algorithms are available in ANSYS software: Block Lanczos and Subspace algorithm.

In the next section, the developed formulation is applied to the linear buckling analysis of intact and delaminated plates and shells.

6.1.1 Numerical tests of linear buckling analysis

In this section, convergence and verification studies are accomplished to examine the capability of model in predicting the linear buckling loads and mode shapes of plates and shells. Therefore, first, the buckling analysis of multi-layered laminated plates is investigated. Then, the composite multi-layered shells are analysed.

Linear buckling analysis of composite plates with delamination

The geometrical and material properties of the studied laminate are provided in table 6.1.

Table 6.1: Material and geometrical properties of studied laminated plate.

a (m)	b (m)	h (m)	E_{11} (GPa)	E_{22} (GPa)	ν_{12}	G_{12} (GPa)	G_{13} (GPa)	G_{23} (GPa)
0.1	0.025	0.001	142	10.8	0.3	5.49	5.49	3.72

The laminated plate is composed of eight layers with lay-up $[45^\circ / -45^\circ / 0^\circ / 90^\circ]_s$. It is fully clamped on one of the small edges whereas subjected to an axial compressive load on the other small edge. The schematic view of the studied laminate is shown in figure 6.1.

First, the laminate is supposed to be intact. Thus, only the standard DOFs from the finite element method contribute into the buckling analysis. In order to investigate the precision of the results, different element sizes are considered and the obtained buckling loads are compared with the ones of Nagashima and Suemasu (2010) in table 6.2.

As it is shown in table 6.2, very good convergence property for the presented model is achieved. Moreover, a fair agreement is demonstrated for the buckling loads that are predicted by the presented model with the results of Nagashima and Suemasu

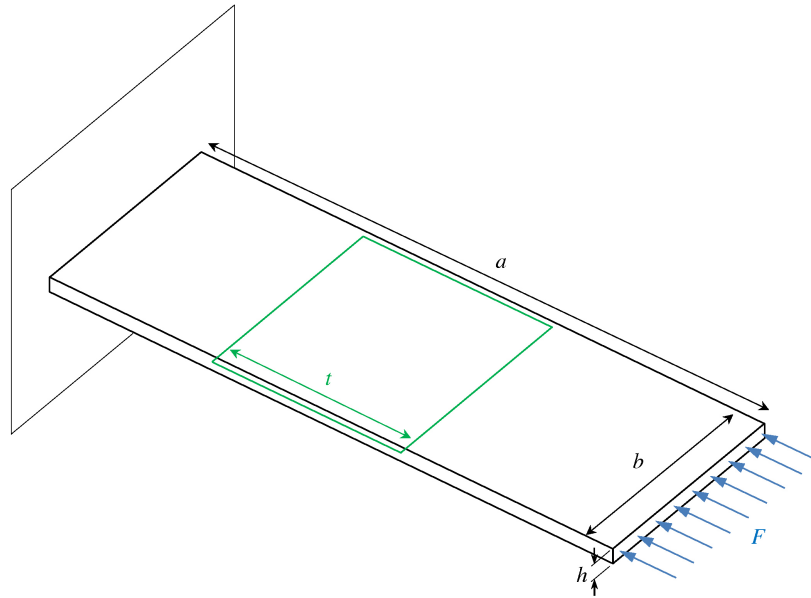


Figure 6.1: Schematic view of the composite laminate with delamination under axial compressive load.

Table 6.2: Convergence study on the buckling loads of intact laminate.

Element size (m)	Buckling load (N)								
	1	2	3	4	5	6	7	8	9
0.01	19.861	192.63	612.11	1412.7	2824.7	4747.5	5035.2	5294.4	5612.9
0.005	19.650	184.91	553.88	1167.0	2055.3	3249.9	4457.4	4821.1	4951.5
0.0025	19.534	182.23	537.11	1106.8	1895.5	2898.4	4065.0	4304.3	4830.9
0.00125	19.479	181.20	531.40	1088.3	1850.3	2805.6	3907.3	4177.0	4770.8
ABAQUS S4 (number of elements = 200)	19.444	182.415	541.825	1129.725	1962.85	-	-	-	-
XSHELL (number of elements = 200)	19.67475	185.1525	554.8	1169.3	2059.975	-	-	-	-

(2010), and especially with the ones of ABAQUS software. The XSHELL model is an isoparametric shell element that was enriched by XFEM. The first nine buckling mode shapes of the finest mesh scheme are depicted in figure 6.2.

In the next case study, the buckling analysis of composite laminates with delamination is investigated. Thus, the discontinuous region depicted in figure 6.1 is now taken into account with longitudinal length t equal to 40 mm, 45 mm, and 50 mm. The delamination is located exactly at the middle of thickness, between the fourth and the fifth layers. In the simulation process the standard DOFs are considered in the continuous part. However, extra DOFs are included as well in the discontinuous region. The delamination front is formed by constraining the extra DOFs, exclusively. First, a convergence study for the composite laminate with the delamination length equal to 40 mm is carried out to demonstrate the precision of the XFEM model developed. The first nine buckling loads are reported in table 6.3.

A fair convergence property is achieved for the model with extra DOFs. Again, the obtained results are closer to the results of ABAQUS S4 element reported in Nagashima

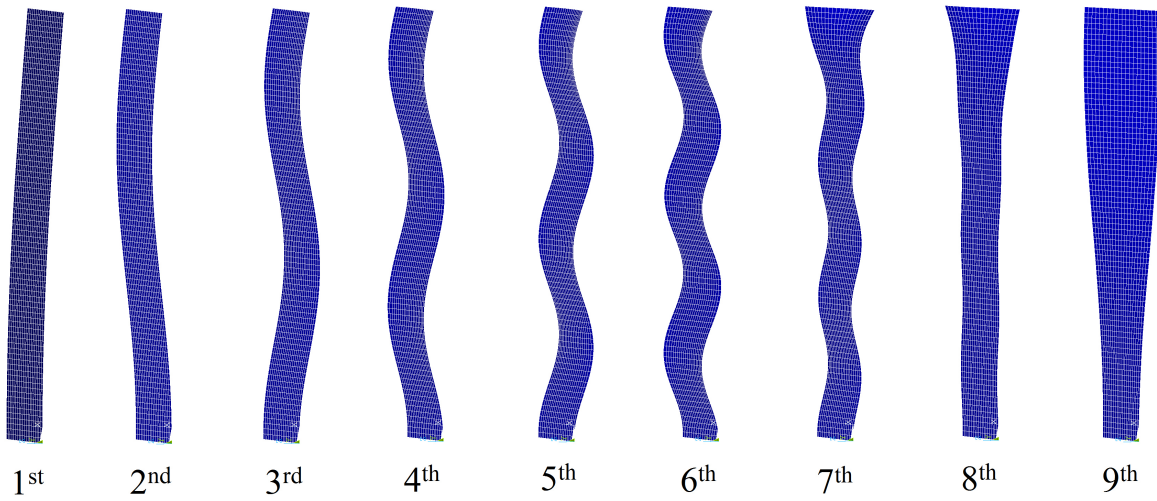


Figure 6.2: Buckling mode shapes of intact multi-layered composite laminate.

Table 6.3: Convergence study on buckling loads of delaminated laminates ($t=40$ mm)

Element size (m)	Buckling load (N)								
	1	2	3	4	5	6	7	8	9
0.005	18.122	93.933	271.33	418.66	455.50	764.19	791.48	917.11	994.67
0.0025	17.984	91.723	255.49	375.17	422.26	710.01	710.88	825.61	892.06
0.00125	17.923	91.057	251.12	364.37	413.41	685.82	694.39	801.73	856.76
ABAQUS S4 (number of elements = 200)	17.9435	93.7975	269.975	418.40	452.825	-	-	-	-
XSHELL (number of elements = 200)	18.148	94.0725	272.200	420.725	456.975	-	-	-	-

and Suemasu (2010), in that the delaminated region was simulated through double nodes. The corresponding first and fourth mode shapes of the finest mesh scheme are depicted in figure 6.3.

It is mentioned that the visualisation of the delaminated region is carried out in post-processing by generating artificial elements that contain values of standard and enhanced unknowns. In the final example, the length of the delamination is altered to 45 mm and 50 mm and the first nine buckling loads are presented in table 6.4. The element size is supposed to be 0.00125 m.

Table 6.4: Buckling loads of composite laminates with delamination ($t_1=45$ mm and $t_2=50$ mm).

t (mm)	Method	Buckling load (N)								
		1	2	3	4	5	6	7	8	9
45	Present	17.331	80.522	214.04	282.01	392.91	562.48	635.95	714.14	725.66
	XSHELL	17.937	90.702	256.900	390.730	446.800	-	-	-	-
50	Present	16.634	72.425	182.85	224.15	372.36	458.72	595.60	640.83	649.24
	XSHELL	16.850	74.378	196.450	242.790	410.500	-	-	-	-

As it was expected, by increasing the delaminated area the predicted buckling load is reduced. The fundamental buckling loads are in particular in a good agreement with

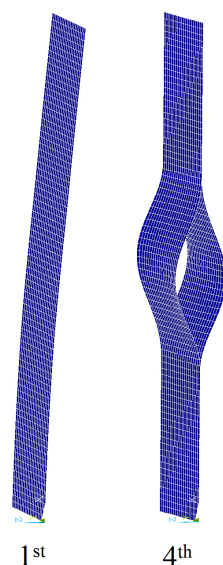


Figure 6.3: Linear buckling mode shapes of delaminated composite plate.

the ones of Nagashima and Suemasu (2010).

Linear buckling analysis of composite shells

The buckling analysis of a simply supported cross-ply cylindrical shell panel is investigated. The schematic view of the studied model is shown in figure 6.4.

The composite cylindrical shell panel composed of five layers with $[0^\circ/90^\circ/0^\circ/90^\circ/0^\circ]$ lay-up and aspect ratio $a/b=1$ and $R/a=20$. The material properties of plies are considered as: $E_L/E_T=40$; $G_{LT}=0.5E_T$; $G_{TT}=0.6E_T$; $\nu_{LT}=0.25$. Different thickness to length ratios are taken into account and their critical buckling loads are compared with Di Sciuva and Carrera (1990), ANSYS, and ABAQUS software in table 6.5. The reported results are adimensionalized by the following equation

$$\bar{P}_c = \frac{P_c a^2}{E_T h^3} \quad (6.5)$$

Table 6.5: Non-dimensionalized critical buckling load \bar{P}_c of the cylindrical shell panels.

Method	Element size	a/h				
		10	20	30	50	100
Present	7×7	25.517	34.122	36.358	37.796	39.281
	10×10	24.774	33.695	35.872	37.27	38.719
	20×20	24.247	33.36	35.497	36.87	38.294
	30×30	24.146	33.288	35.421	36.791	38.212
Di Sciuva and Carrera (1990)		24.19	31.91	34.04	35.42	36.86
ANSYS (Shell 181)	30×30	20.199	31.828	35.359	36.769	38.204
ABAQUS (S4R)		20.189	31.821	35.354	36.764	38.199

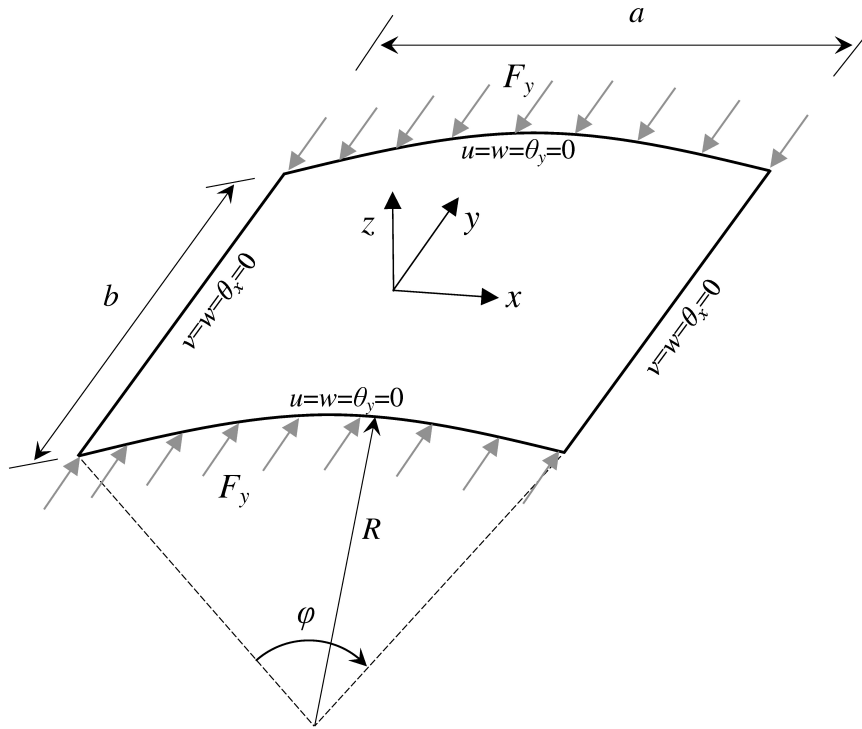


Figure 6.4: Schematic view of the cylindrical shell panel.

The obtained results agree very well with the ones of commercial pieces of software, especially when the moderately thick laminates were analysed. In addition, a fair convergence property for the presented formulation was demonstrated.

In the next example, the linear buckling analysis of composite cylindrical shell is performed. The cylindrical shell has 520 mm length with a radius of 350 mm. It is composed of four distinct layers with $[0^\circ/45^\circ/-45^\circ/0^\circ]$ and $[45^\circ/-45^\circ/-45^\circ/45^\circ]$ lay-ups. It is noted that the fibre orientations are defined with respect to the axial direction of the cylinder. The material properties of the laminate are listed in table 6.6.

Table 6.6: Material properties of the composite cylindrical shell.

E_{11} (GPa)	E_{22} (GPa)	ν_{12}	G_{12} (GPa)	G_{13} (GPa)	G_{23} (GPa)
52	52	0.302	2.35	2.35	2.35

The bottom edge of the cylinder is considered to be fully clamped while the upper edge is constrained except the translational DOF in the axial direction. The studied shells are subjected to the axial compressive load on the upper edge. In the finite element analysis, different mesh sizes are taken into account and the critical buckling loads are calculated, accordingly. The calculated results from the present formulations are compared with the analytical solution of Bisagni (2000), ANSYS, and ABAQUS software in table 6.7.

The obtained buckling loads of the finest mesh scheme were in a fair agreement with

Table 6.7: Critical linear buckling loads (kN) of composite cylindrical shells.

Lay-up	Method				
	Mesh	Present	Analytical (Bisagni, 2000)	ANSYS (Shell181)	ABAQUS (S4R)
[0°/45°/ - 45°/0°]	56×13	365.70	240.0	-	-
	68×16	329.39			
	92×21	288.05			
	112×26	271.59			
	168×40	254.74			
	220×52	246.23			
			248.42	248.41	
[45°/ - 45°/ - 45°/45°]	56×13	288.61	118.58	-	-
	68×16	249.86			
	92×21	193.06			
	112×26	168.20			
	168×40	140.31			
	168×40	131.83			
			120.58	120.55	

the ones of the analytical solution as well as the standard elements available in finite element software. As it is observed, in the eigenvalue analysis the critical buckling load values are very sensitive to the element size. This fact was already reported by Bisagni (2000) that clarifies the importance of performing the non-linear buckling analysis.

The first buckling mode shapes are depicted in figure 6.5.

Based on the buckling loads and mode shapes obtained in the current analysis, one can conclude that the fibre orientation has a significant influence on the structural response of the cylindrical shells.

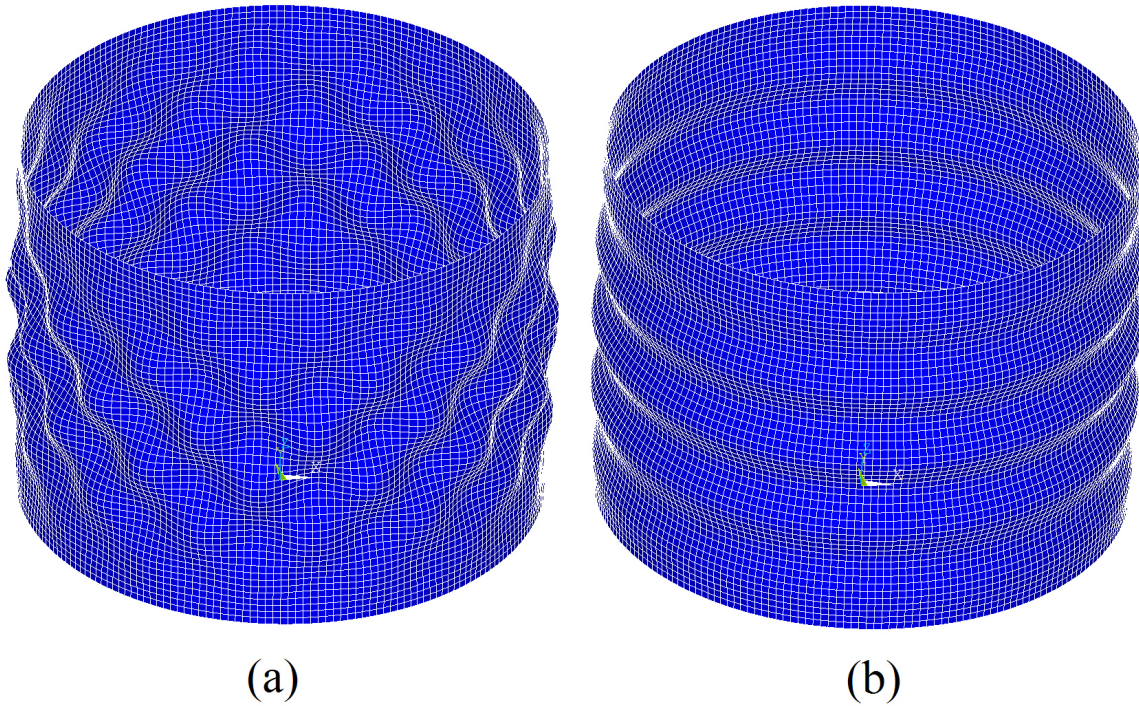


Figure 6.5: Buckling shape of the composite cylindrical shells: (a) $[0^\circ/45^\circ/ - 45^\circ/0^\circ]$; (b) $[45^\circ/ - 45^\circ/ - 45^\circ/45^\circ]$.

6.2 Non-linear buckling analysis

The linear buckling analysis is not sufficient to analyse plate and shell structures. Therefore, the non-linear buckling analysis for such structures is proposed. The importance of performing a non-linear buckling analysis for plates and shells is described as

- In the linear buckling analysis, axisymmetric and non-axisymmetric mode shapes can occur. The axisymmetric modes associate to each unique eigenvalue whereas the non-axisymmetric ones are related to the repeated eigenvalues. It is noticed that most of the buckling modes in shell structures are related to the non-axisymmetric shapes (Wohlever, 1999).
- The geometrically non-linear behaviour contributes to the response of plates and shells. In the linear buckling analysis this behaviour is neglected. However, the geometrically non-linear behaviour actually leads to a reduction of buckling load.
- The buckling-driven delamination analysis cannot be studied by a linear buckling analysis because the contact constraints or the interface formulation like the cohesive zone model can only be implemented within a non-linear analysis.
- The inclusion of manufacturing imperfections within the analysis is only possible when a non-linear buckling problem is analysed.

In this section the non-linear buckling analysis of composite structures is discussed. First, the common responses of composite laminates under the buckling load are described. Then, a general overview of the available techniques for simulating the buckling phenomenon with the finite element method is presented. An algorithm that is consistent with the XFEM topology is proposed for incorporating imperfections in the non-linear buckling analysis. Finally, the reliability of the developed formulation is examined in verification studies.

The response of thin-walled structures to the applied load varies from plates to shells. In fact, the curvature has a significant effect on the load-carrying capacity of the structure. For instance, once the curvature is moderate like in panels, the snap-through response is observed. The bifurcation behaviour of buckling is reproducible for the response of cylindrical shells under axial compressive loads or spherical shells under external loads. The reason for occurrence of buckling in plate and shell structures is due to the high membrane stiffness in comparison to the bending or shear stiffness. Therefore, when the structure is subjected to a compressive load, the majority of the strain energy is conserved in the membrane format. Once it cannot sustain further load, part of the membrane strain energy is converted into the bending strain energy and the structure collapses. Thus, some kinetic energy is dissipated by the structure to remain in the equilibrium state, and consequently, a sudden drop in the load-displacement diagram is observed (see point A in case of the structure deforms non-axisymmetrically and point B when it deforms axisymmetrically in figure 6.6). As soon as the equilibrium state establishes again, the post-buckling behaviour of the structure is traced. The sample of load-displacement diagrams of a structure under compressive loading is drawn in figure 6.6.

In the non-linear buckling analysis, some key points are noticeable in the load-displacement diagram of the structure. In figure 6.6, the curve OBC represents a snap-through problem. Point B is the limit point of the structure that is of importance in engineering applications. Point A corresponds to the bifurcation point and the curve AD represents the post-buckling response of the structure. If the curve OBC corresponds to axisymmetric deformation of the structure and AD to non-axisymmetric deformation, the initial failure of the structure is characterized by non-axisymmetric deformation. Hence, the bifurcation point can be of more importance than the limit point.

In cylindrical shells the circumference buckling shapes correspond to the weakness in the bending part of structure. In contrary, skew shapes of buckling are related to the sensitivity of structure to the anisotropic coupling between bending and twisting (Hilburger and Starnes, 2002). It is noted that in very thin structures, the difference between the maximum load-carrying capacity of structure in axisymmetric and non-axisymmetric responses can be significant. Therefore, finding the bifurcation points is of importance in the non-linear structural analysis.

Plate and shell structures are very sensitive to the initial imperfections that are caused in the manufacturing procedure; and this sensitivity is induced by increasing the curvature in the construction process. In figure 6.6 the response of the cylindrical shell with initial imperfection is depicted in the dotted line. A drop in the maximum

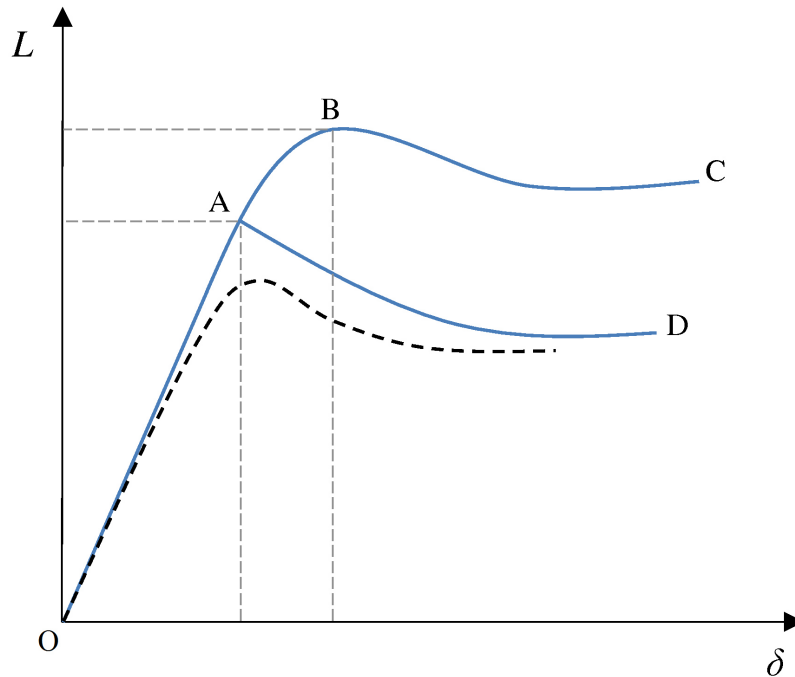


Figure 6.6: Load-displacement diagram of a cylindrical shell under axial compression.

load compared with the initially imperfect structure is observed. This reduction in the strength of structure is increased by intensifying the imperfection amplitudes.

In the simulation process using the finite element method, typically the initial imperfection is applied to the perfect structure to avoid facing the bifurcation points, and consequently, to facilitate tracking the non-linear response of the structure during the post-buckling analysis (Bushnell, 1981). In addition to the mentioned problem, it is required to apply the arc-length method or Riks method to track the solution path in the post-buckling analysis of structure. In order to apply the imperfections, the geometry of the structure is updated whether randomly through Pseudo numbers or based on the information of eigenmodes obtained from the linear buckling analysis. In the latter case, the buckling modes are scaled and added to the perfect geometry as the initial imperfections. In general, a linear combination of several buckling modes is needed to update the geometry (Elishakoff et al., 1987). By doing so, possible bifurcation points during the non-linear analysis can be tracked. Since both symmetric and anti-symmetric modes are required in the buckling analysis, the full-length model should be simulated.

In composite laminates, due to the existence of a strong coupling between the membrane and bending components especially in the ones with unsymmetric stacking sequence, the occurrence of the buckling phenomenon is unavoidable (Sundaresan et al., 1996). However, the bifurcation instability is rarely observed in laminates with unsymmetric lay-ups. In addition, the existence of possible imperfections has more influence on the sophisticate response of composites during the loading process.

From the mathematical point of view, bifurcation points can be determined by

monitoring the global stiffness matrix of the structure during the solution process. The solution is unstable and a possible bifurcation point exists when one of the following condition is fulfilled (Rust, 2015; Wriggers, 2008; Wriggers et al., 1988):

- The negative determinant of tangent stiffness matrix,
- The existence of at least one negative eigenvalue in the tangent stiffness matrix and
- The existence of at least one negative value in the main diagonal of tangent stiffness matrix after Gaussian triangularization.

In ANSYS software the command PIVCHECK can be issued to automatically check the singularities during the non-linear analysis. As soon as a bifurcation point is passed during the solution process, a negative pivot value is reported in the output file. In the post-buckling response of structure, sometimes the interchanges between the buckling modes might lead to the secondary bifurcation point.

The measurement of imperfection in the experimental procedure is performed by finding the relative out-of-roundness of the geometry in comparison to the average thickness of structure. Apart from the possible manufacturing imperfections, the buckling analysis of cylindrical composite shells is very sensitive to the loading condition, boundary conditions, and changes in material properties (Hilburger and Starnes, 2002).

In the numerical simulation, imperfections can also be applied through one of the following approaches (Rust, 2015):

- By updating the geometry based on the linear buckling mode shapes,
- By forces type imperfections,
- By initial geometrical prescriptions and
- By different mesh patterns.

The first method was described enough in the previous sections. Forces type imperfections can be applied by subjecting the structure to non-axial forces. By doing so, a very small amount of bending moment is generated that can cause the interchanges between the membrane and bending loading conditions. Furthermore, Pseudo numbers can be utilized to apply the geometrically prescribed imperfection. In figure 6.7 (a) and (b) the imperfections by means of the prescribed geometry or force are shown, respectively.

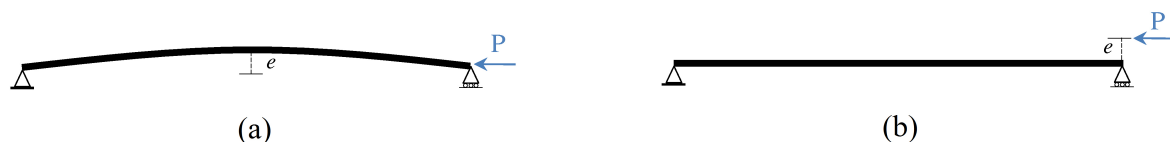


Figure 6.7: Imperfection types: (a) by geometry prescription; (b) by force.

In this chapter the focus would be on the buckling analysis of pre-delaminated composite structures under the axial compression. The initial delamination could be the result of instabilities in the manufacturing process, local loads, the type of loading, and the poor design.

In the linear buckling analysis of composite laminates with initial delamination that is located near the surface of laminate, inward or outward deformed shape of the discontinuous subdomains can be obtained. The inward modes of the linear buckling analysis correspond to the penetration of interfaces which is not physically interpreted (Chai et al., 1981; Qiu et al., 2001). Thus, performing a non-linear buckling analysis considering the contact at the interface regions is obligatory. In the non-linear buckling analysis of the mentioned problem, the so-called pocket-like delamination that leads to an elliptical shape of delamination surface is achieved (Bolotin, 1996).

Depending on the position of delamination in the laminated structures, various structural responses are expected. Once the initial delamination is located at the middle of thickness it might influence the global bulk of material. Henceforth, the second mode of the mentioned problem corresponds to the global buckling of both subdomains into one side. In contrary, the local buckling of the weaker subdomain is observed when the delamination is located near the surface of laminate. Therefore, the critical buckling mode is related to the delamination itself (Short et al., 2001). The latter type of delamination always leads to a reduction in the strength of laminate (Bolotin, 1996) that attributes to the coupling between the buckling and the delamination buckling phenomenon (Qiu et al., 2001).

In order to trigger the delamination buckling mode within the non-linear analysis, either a small outward load perturbation or a small perturbation due to a scaled linear buckling mode should be applied at the discontinuous region (Allix and Corigliano, 1999; de Borst et al., 2004). However, the lack of nodal points at the plane of discontinuity in the present formulation needs a special algorithm for applying forces leading a deformation proportional to the delamination buckling mode. A flowchart view of this new algorithm is depicted in figure 6.8.

The algorithm is started by conducting a linear buckling analysis. In case the critical buckling mode shape ϕ_1 corresponds to the local delamination, a small factor of dislocations (here in terms of enhanced displacements) is applied to the model to retrieve the nodal reaction forces within a linear static analysis. Next, the non-linear buckling analysis is initiated by applying the reaction forces of the enhanced DOFs. By doing so, a deformation proportional to the delamination buckling is introduced. Then, the same analysis is followed by applying the actual compressive load. If the critical buckling mode does not represent the delamination, the geometric imperfection from the critical buckling mode shape should be used as well. Here ϕ_1 and ϕ_d correspond the critical and delamination buckling eigenmodes, respectively. κ_1 and κ_2 are small factors that are multiplied by eigenmodes to represent the imperfection magnitude. By following the mentioned algorithm, the possibility of introducing multi bifurcation paths is provided. The algorithm prescribed in figure 6.8 is provided in ANSYS software version 14.5 using ANSYS command language APDL.

In the next section, several benchmark tests for the non-linear delamination buckling and growth in laminated composites are investigated. The results obtained by the proposed formulation are compared with the ones available in literature.

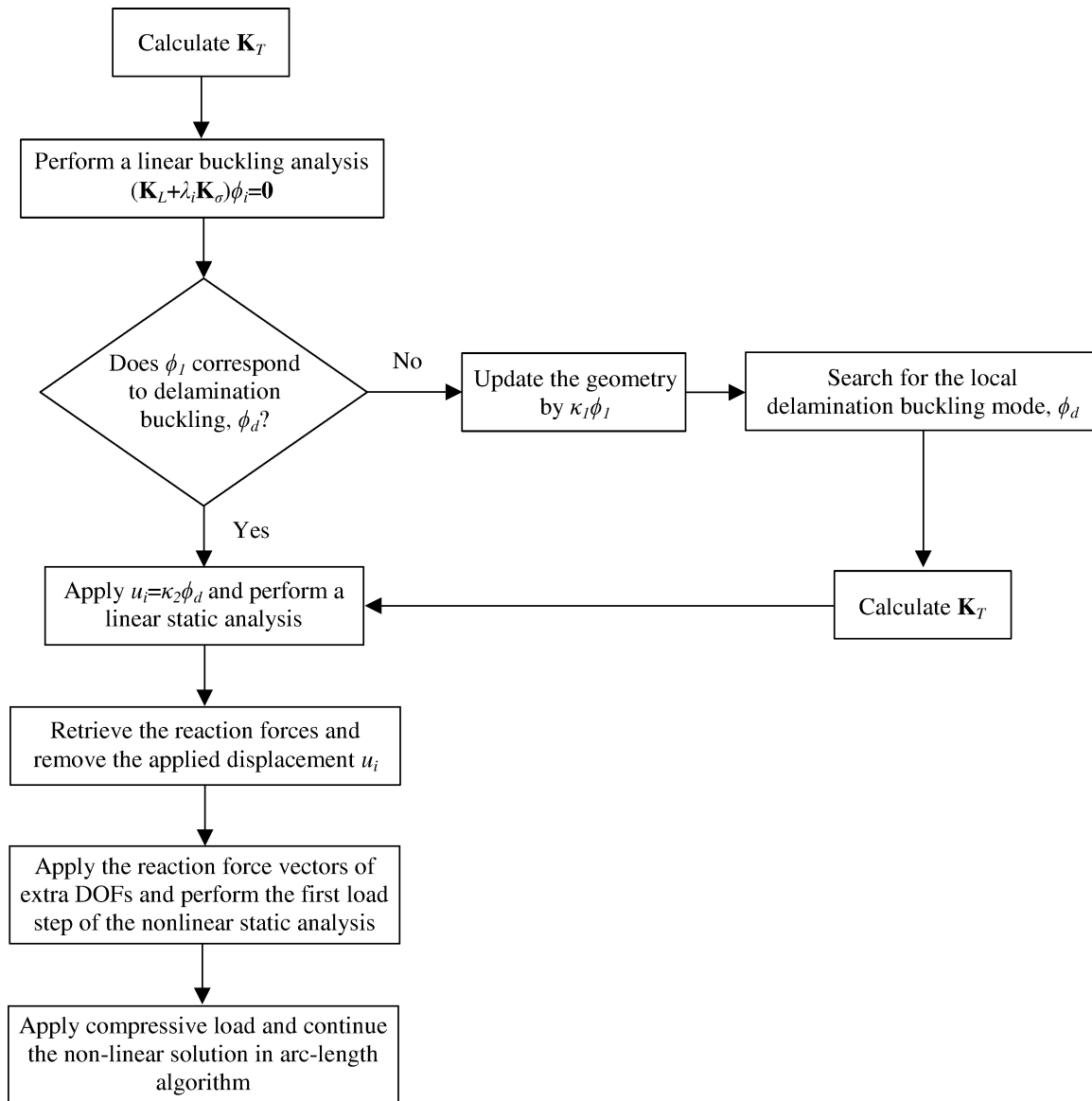


Figure 6.8: Flowchart view of non-linear delamination buckling analysis.

6.2.1 Numerical tests of non-linear buckling analysis

In this section, a few non-linear delamination buckling tests are carried out by the developed XFEM model. In the first example, the composite plate with delamination that was studied in section 6.1.1 is adopted again. The material properties and the geometrical dimensions of the plate are provided in table 6.8.

The length of delamination t is supposed to be 40, 45, and 50 mm. The goal of this study would be a comparison between the responses of the delaminated composite plates with the intact one while a compressive axial loading is applied. The algorithm presented in figure 6.8 is being followed to obtain the structural response of the laminate. In the linear buckling analysis the critical buckling mode associates to the

Table 6.8: Material properties and geometrical dimensions of the studied laminated plate.

a (m)	b (m)	h (m)	E_{11} (GPa)	E_{22} (GPa)	ν_{12}	G_{12} (GPa)	G_{13} (GPa)	G_{23} (GPa)
0.1	0.025	0.001	142	10.8	0.3	5.49	5.49	3.72

bending of the structure whereas the fourth one attributes to the outward separation of layers. Therefore, in order to carefully track the response of laminate, a combination effect of the buckling Mode I and IV is applied. The amplitudes of imperfections are assumed as $\kappa_1 = h$ and $\kappa_2 = 0.025h$. It should be mentioned that excluding the bending type imperfection will lead to negative pivot values in the vicinity of the critical buckling load. The element size is supposed to be 1.25 mm. The compressive load versus the transverse displacement of the edge at the point where the load is applied, is compared with the undamaged one in figure 6.9.

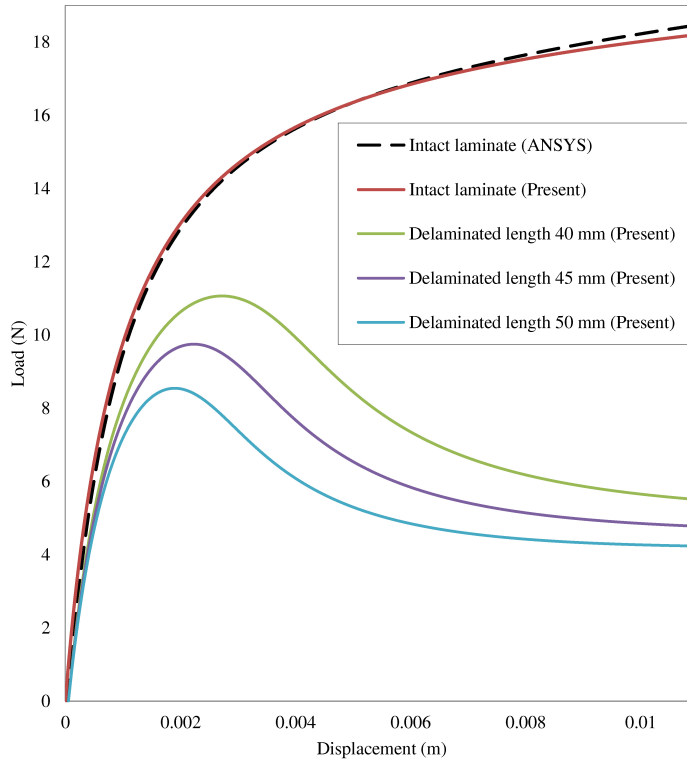


Figure 6.9: Load-displacement diagram of composite laminated plates under compressive loading.

A meaningful reduction of the maximum carried load is observed for the composite plates containing the greater delamination surface t . Moreover, the higher load magnitudes are supported by the undamaged plate than the delaminated ones. Taking the results of the linear buckling analysis as the reference, the maximum supported load of the undamaged laminate is closer to its critical one. However, less load amplitudes is supported by the delaminated ones. The deformed shape of the composite laminate

with delamination length $t=40$ mm in the last loading step is shown in figure 6.10.

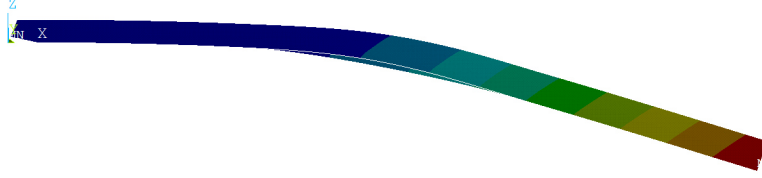


Figure 6.10: Deformed shape of the composite laminated plate with delamination under compressive loading.

Next example is related to the buckling induced delamination in a built-in plate with a central crack under axial compressive loading. This is a well-known benchmark problem for the delamination buckling and growth analysis that was proposed by Allix and Corigliano (1999). Both ends of the plate are fixed as depicted in figure 6.11.

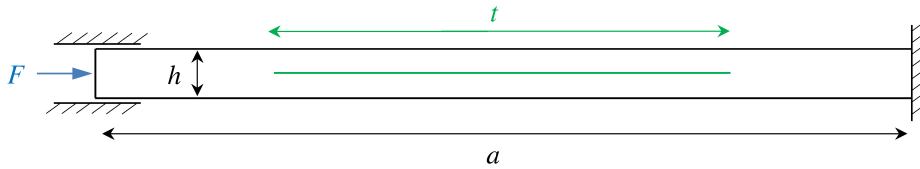


Figure 6.11: The schematic view of the buckling induced delamination test.

The material properties and geometrical dimensions of the studied test are provided in table 6.9.

Table 6.9: The material properties and geometrical dimensions of buckling induced delamination test.

a (m)	b (m)	h (m)	t (m)	E (GPa)	G (GPa)	G_I^{cr} (N/m)	N (MPa)	β
0.02	0.001	0.0004	0.01	135	57	200	50	2

In the simulation process, XFEM and contact formulation are applied to the discontinuous region whereas the XFEM and mixed-mode cohesive formulation are used in the remaining area. Unlike the previous example, here, since the translational displacements at the location of applying load are suppressed in y and z directions, bending mode is excluded from the response of the laminate. In this example, the third linear buckling mode is related to delamination buckling and it is utilized to impose the imperfection in the non-linear buckling algorithm. However, in Allix and Corigliano (1999) the symmetrical perturbation was aided to initiate the delamination buckling at the interface region. Thus, in this analysis κ_1 is neglected and only $\kappa_2=0.05h$ has been employed. The plate is discretised using an element size equal to 0.1 mm. The compressive load versus the transverse displacement of the delaminated area is compared with the results of Allix and Corigliano (1999) in figure 6.12.

In the load-displacement diagram, the delamination propagation is followed by a drop in the carrying load. The results of the present formulation correlate very well

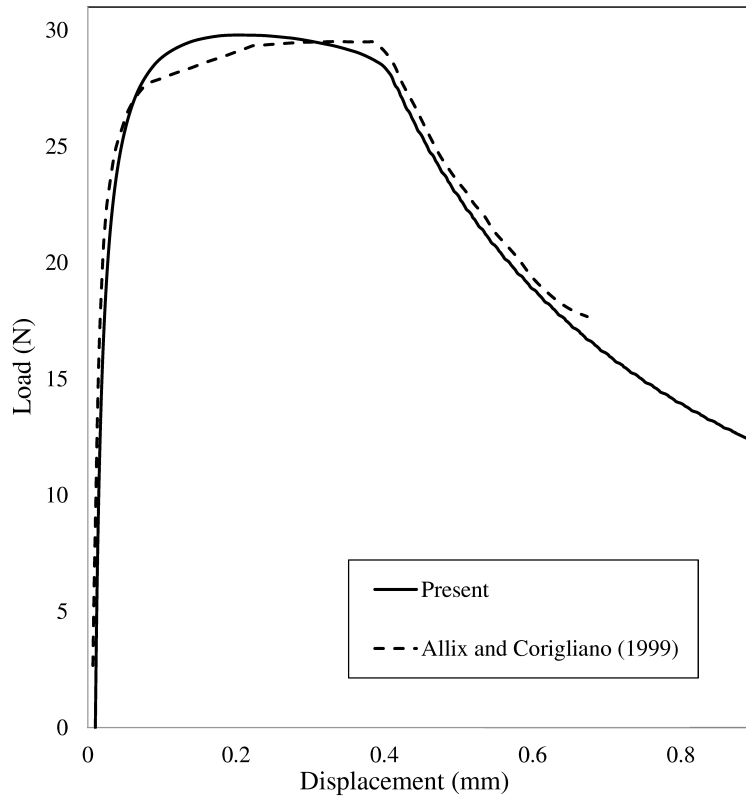


Figure 6.12: Load-displacement diagram of the buckling induced delamination test.

with the ones of Allix and Corigliano (1999). In order to sketch a better idea about how the delamination buckles and grows at the interface area, the deformed shape of the present test in the time domain is depicted in figure 6.13.

Next, a DCB model with the initial delamination length $t=10$ mm is investigated. The plate is subjected to the axial compressive loading $2F$ on the delaminated subdomains. Moreover, two small perturbation loads $F_p=0.001$ N are used to initiate the mode concerning the delamination buckling. The schematic view of the studied test is shown in figure 6.14.

The mid-plane of the present discontinuous shell formulation is unique and located at the middle of the total thickness. Therefore, care must be taken when two axial loads are applied to lower and upper subdomains. Although enhanced DOFs handle the simulation of upper subdomain, two extra bending moments with the amplitude of $Fh/4$ should be superimposed to compensate the bending moments that are produced due to the mid-plane offsets in the contrary direction. The material properties and the geometrical data of this example are reported in table 6.9. To better predict the delamination propagation, the element size in the axial direction is chosen sufficiently small. The applied loads F versus the maximum transverse displacements are compared with the ones of Allix and Corigliano (1999) in figure 6.15. The linear-exponential cohesive zone model is applied in the simulation process.

Once the load is increased, the plate tends to buckle outward on both subdomains

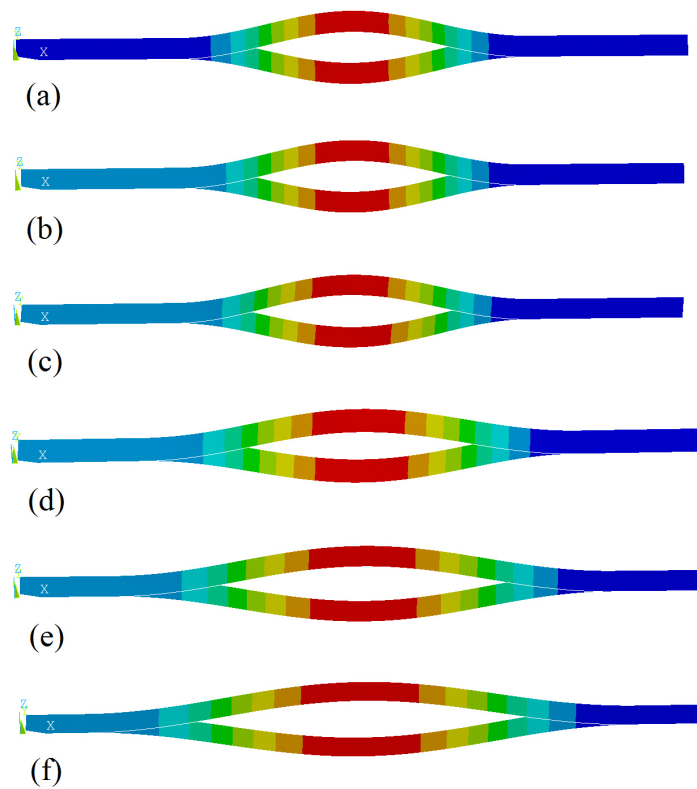


Figure 6.13: Deformed shape of buckling induced delamination in time domain: a) $F=19.2$ N, $\delta_{max}=0.0103$ mm, b) $F=29.79$ N, $\delta_{max}=0.1990$ mm, c) $F=28.73$ N, $\delta_{max}=0.3854$ mm, d) $F=20.51$ N, $\delta_{max}=0.5545$ mm, e) $F=15.44$ N, $\delta_{max}=0.7303$ mm, f) $F=11.92$ N, $\delta_{max}=0.9285$ mm.

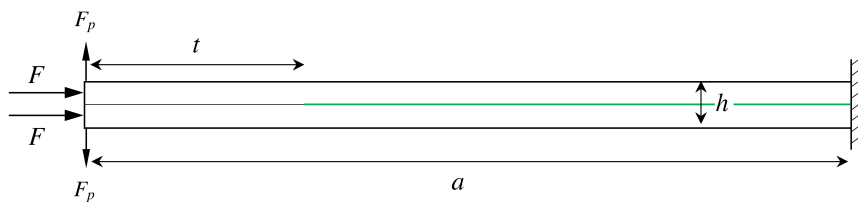


Figure 6.14: Schematic view of DCB test under axial compression.

and large displacements are achieved on the split region. Then, at a certain displacement, the delamination starts to grow on the same discontinued interface where a drop in the supported load is attained.

In the next example, the delamination behaviour of a composite laminate with a circular delamination is studied. The schematic view of the laminate is shown in figure 6.16.

All standard and enhanced DOFs of the plate are constrained in the shaded area except the standard translational displacement in x direction. The composite plate consists of 35 cross-ply lay-up while the delamination is located between the 28th and 29th ply, counting from the bottom surface. The stacking sequence is in

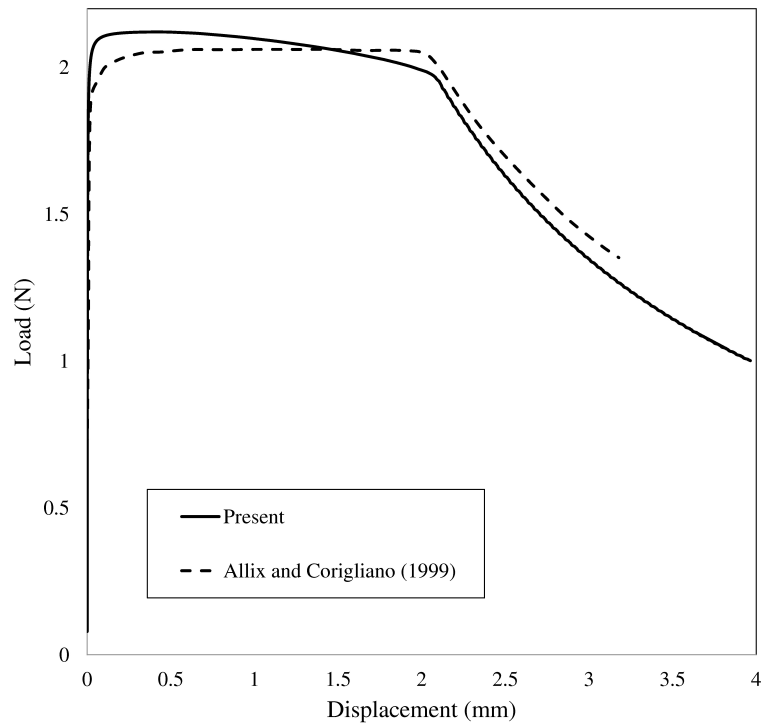


Figure 6.15: Load-displacement diagram of DCB test under axial compression.

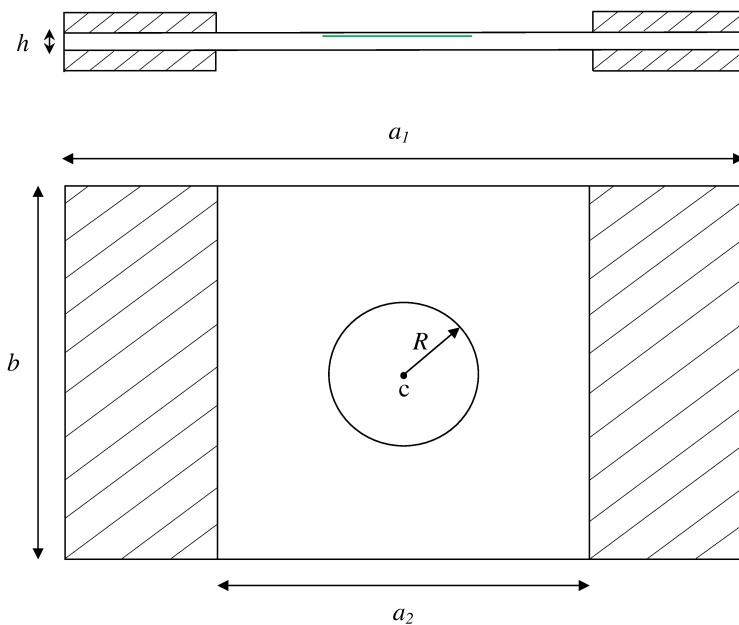


Figure 6.16: Schematic view of the composite plate with a circular delamination.

$[(90^\circ/0^\circ)_{14} // (90^\circ/0^\circ)_3/90^\circ]$ format where the $//$ sign describe the existence of a delamination. The geometrical dimensions of the plate are: $a_1=300$ mm, $a_2=150$ mm, $b=150$ mm, $R=30$ mm, $h=4.56$ mm. The material properties of the composite and the interface are presented in table 6.10.

Table 6.10: Material properties of the composite and interface for the plate with circular delamination.

E_{11} (GPa)	E_{22} (GPa)	ν_{12}	$G_{12} = G_{13}$ (GPa)	G_{23} (GPa)	N (MPa)	S (MPa)	G_I^{cr} (N/mm)	G_{II}^{cr} (N/mm)	α
131	11.7	0.3	5.2	3.9	66.54	133.763	200	570	2

The goal of the present study is to capture the nucleation of delamination buckling and delamination growth at the interface region of the laminate. Therefore, in the simulation procedure the XFEM and contact formulations are particularly utilized in the discontinuous region. The mixed-mode cohesive formulation is overlaid in the vicinity of the delamination at $R=30-60$ mm from the centre c . Due to symmetry in load and boundary conditions, only one quarter of the plate has been modelled. In the linear buckling analysis the first mode shape refers to the delamination buckling. Therefore, a small imperfection of order $\kappa_2=0.01h$ is selected, exclusively. The results of the present formulation are compared with the experimental ones reported in Nilsson et al. (2001) in figure 6.17.

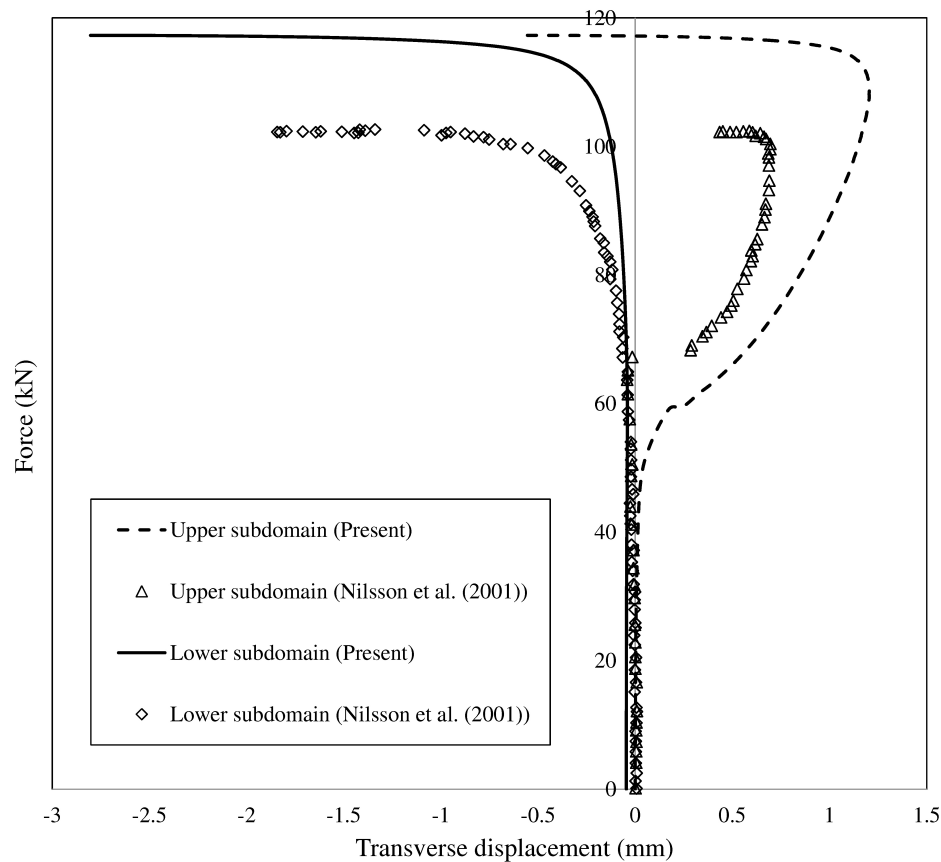


Figure 6.17: Axial compressive loads versus maximum outward transverse displacements of delaminated subdomains.

As it can be seen in figure 6.17, the response of the structure starts with an upward

buckling of the upper subdomain where positive displacements occur. After that the whole structure undergoes global buckling. The deformed shape of the plate at the last loading step is depicted in figure 6.18.

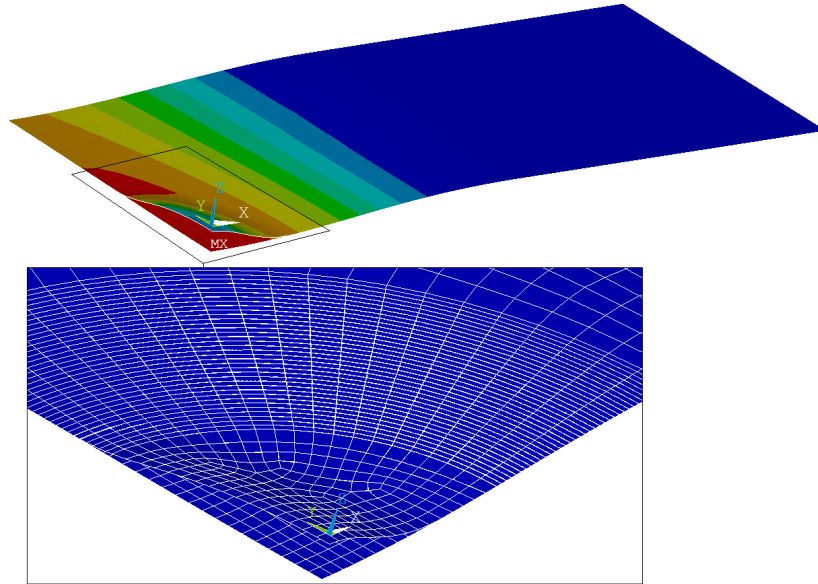


Figure 6.18: The deformed shape of the plate with circular delamination in the last loading step.

As it was reported by Bolotin (1996) the pocket-like delamination has the form of an elliptical delamination shape. This elliptical delamination configuration is depicted in figure 6.18.

6.3 Closing remarks

In this chapter the importance of linear and non-linear buckling analysis was discussed. The numerical techniques were described to perform and to handle the non-linear solution. For instance, a new algorithm was proposed to include the geometric and force type imperfections. The present formulation reveals very promising results when the simulation of delamination buckling and the growth are of interest.

Chapter 7

Delamination analysis in composites of variable stiffness

7.1 Introduction

The traditional Constant Stiffness Composite Laminates (CSCL) consist of fibres and matrix material in which the fibre angles are straight and constant within the surface of each ply. Henceforth, their characteristics are varied in the ply sequence by altering the material properties or fibre orientations at each particular ply level. However, the curvilinear fibre orientation format can be set up by a tow-placement machine to produce variable stiffness plies, leading to Variable Stiffness Composite Laminate (VSCL). Tatting et al. (2002) utilized a tow-placement machine to manufacture laminated panels with curved path fibres. The available numerical models which have been utilized to simulate the performance of VSCLs are mainly based on plate and shell theories. For instance, the early simple Classic Laminate Theories (CLT) were implemented to investigate the vibration of VSCL plates in Abdalla et al. (2007); Honda and Narita (2012). The equivalent single layer theories were applied to compute the response of VSCL plates in linear and geometrically non-linear regime in Akhavan et al. (2013). The free vibration and structural response of the VSCLs were analysed using layer-wise theories in Yazdani and Ribeiro (2015) and Yazdani et al. (2014), respectively. A comprehensive literature review of the mechanical behaviour of VSCL panels can be found in Ribeiro et al. (2014). Due to the increased buckling load capacity of VSCLs in comparison to the traditional CSCL panels, the major attention was devoted to buckling analysis (Gürdal et al., 2008; Lopes et al., 2008; Setoodeh et al., 2009). Recently, Diaz et al. (2012) investigated the interlaminar stress distributions in VSCL plates. These stresses are required in the delamination onset criterion. The impact behaviour of VSCL was carried out by Dang and Hallett (2013); Dang et al. (2014). They performed experimental tests and finite element simulations to investigate the impact damage on variable stiffness panels.

Due to the lack of references for the delamination analysis of VSCL laminates and the ability of present approach to investigate their structural behaviour, in this chapter the attention is devoted to these materials. Case studies are performed to investigate

the effect of the fibre angle parameters of VSCL plates on the delamination onset, and consequently, the propagation analysis.

Here, the VSCL plates with curvilinear fibre orientations are of interest. The reference curvilinear fibre path is defined as

$$\theta(x) = \frac{2(T_1 - T_0)}{a}|x| + T_0 \quad (7.1)$$

where $\theta(x)$ is the fibre angle that is a function of x , T_0 denotes the fibre angle at the origin of ply, and T_1 is the fibre orientation at the edge of each ply. The symbol $|\bullet|$ denotes the absolute value of x . The fibre orientation path within the plane of each ply is shown in figure 7.1.

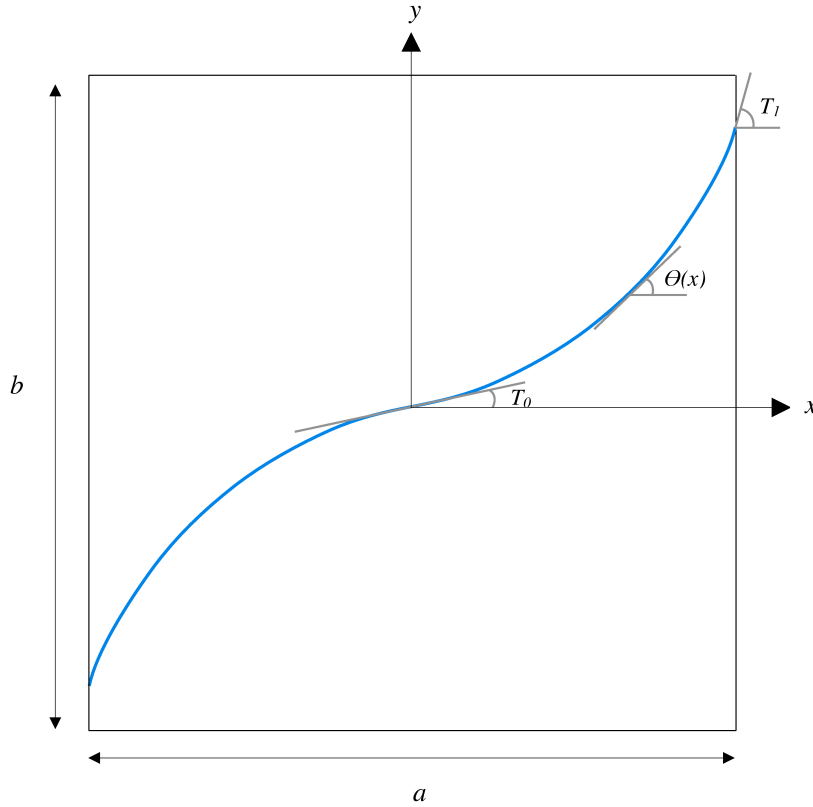


Figure 7.1: Curvilinear fibre orientation path.

The constitutive matrix of orthotropic laminate is related to the material properties and the fibre angle. This matrix remains constant at each ply level for CSCLs. However, based on the curvilinear fibre format used in VSCLs, it is expressed as a function of location with changing values along x axis for each specific ply. Furthermore, the constitutive equation of the multi-layered laminate can vary through the stacking sequences. Therefore, equation 2.17 is rewritten in the following format

$$\boldsymbol{\sigma} = \bar{\mathbf{Q}}(x)\boldsymbol{\varepsilon} \quad (7.2)$$

where the constitutive equation of each orthotropic ply $\bar{\mathbf{Q}}(x)$ is a function of location x , too.

7.2 Numerical tests

In order to examine the behaviour of VSCL plates, a few numerical tests are carried out. First, the present model is verified for multi-layered VSCL plates in linear and non-linear regime. Then, the delamination propagation of several VSCL plates is studied. The linear-exponential cohesive zone model is utilized for all the analysis in this chapter. The material properties and geometrical dimensions of the studied plates are provided in table 7.1.

Table 7.1: Geometrical dimensions and material properties of the studied plates.

	a (m)	b (m)	h (m)	E_{11} (GPa)	E_{22} (GPa)	$G_{12} = G_{13} = G_{23}$ (GPa)	ν_{12}	G_I^c (J/m ²)	G_{II}^c (J/m ²)	N (MPa)	S (MPa)	α
Plate 1	1	1	0.01	40	1	0.5	0.25	-	-	-	-	-
Plate 2	0.1	0.02	0.003	135.3	9	5.2	0.24	330	800	3.3	7	2

In table 7.1, a , b , and h indicate the length, the width, and the thickness of plates, respectively.

First, Plate 1 with the lay-ups [$\langle 10^\circ|20^\circ \rangle, \langle 10^\circ|20^\circ \rangle$] and [$\langle 20^\circ|10^\circ \rangle, \langle 20^\circ|10^\circ \rangle$] is chosen. Both plates are subjected to uniformly distributed load of 10 kN/m² while all the edges are considered to be fully clamped. The convergence of model is accomplished by adopting different element sizes. The maximum linear and large deflection response of VSCL plate are compared with the p -version layerwise theory of Yazdani and Ribeiro (2014) in table 7.2 and table 7.3, respectively. The digits presented between the parentheses are the relative differences between the results of the particular mesh scheme with the finest mesh patterns applied.

Very good convergence property is achieved by the present formulation. The discrepancies between the present model and the layerwise theory are revealed more for the non-linear regime (around 1% in maximum). However, for linear deflections 0.6% difference is observed in the maximum case, which is found to be fairly in good agreement. These discrepancies can attribute to the different definition of the displacement field through the thickness of the laminate. In the present approach, the equivalent single layer theory with a linear variation of displacement field through the entire thickness of the multi-layered laminate is assumed. However, in the layerwise theory each ply is modelled as a separate laminate. For that reason, the non-linear kinematic terms

Table 7.2: Maximum linear deflection (w/h) of the VSCL Plate 1 under uniformly distributed transverse load 10 kN/m².

Type	Linear deflection					Layerwise
	Element number					
	20×20	40×40	70×70	100×100	130×130	
[$\langle 10^\circ 20^\circ \rangle, \langle 10^\circ 20^\circ \rangle$]	0.979	0.984	0.9852	0.9855	0.9857	0.978
	(-0.68%)	(-0.17%)	(-0.05%)	(-0.02%)		
[$\langle 20^\circ 10^\circ \rangle, \langle 20^\circ 10^\circ \rangle$]	0.9563	0.9604	0.9614	0.9616	0.9617	0.956
	(-0.56%)	(-0.14%)	(-0.03%)	(-0.01%)		

Table 7.3: Maximum non-linear deflection (w/h) of the VSCL Plate 1 under uniformly distributed transverse load $10 \text{ kN}/m^2$.

Type	Non-linear deflection					Layerwise
	Element number					
	20×20	40×40	70×70	100×100	130×130	
[<10° 20°>, <10° 20°>]	0.7255	0.7264	0.7266	0.7267	0.7267	0.7191
	(-0.17%)	(0.04%)	(-0.01%)			
[<20° 10°>, <20° 10°>]	0.7122	0.7127	0.7128	0.7128	0.7128	0.7062
	(-0.08%)	(-0.01%)				

are incorporated at each particular ply level of a multi-layered laminate. Thus, this intensifies the error between these two theories in the non-linear regime more than the linear case.

Next, the effect of fibre angle on the location of the delamination initiation; and subsequently, the structural response of VSCL laminates is investigated. As it was presented in equation 7.1, two main parameters are involved for indicating the curvilinear fibre angle. Here, the effect of varying these parameters on the delamination growth of the VSCL plates is studied. Therefore, Plate 2 with lay-up [$\langle T_0|T_1 \rangle$, $\langle T_0|T_1 \rangle$] is assumed. The interface properties are taken from Alfano and Crisfield (2001) and a penalty parameter of $1 \times 10^2 \text{ N}/mm^3$ has been selected. The plate is considered to be fully intact and the pre-delaminated region is eliminated. Thus, the XFEM formulation with the mixed-mode linear-exponential cohesive zone model is used at the bonded interface. The plate is subjected to the Mode I loading condition at one of the small edges while it is clamped at the other one. The schematic view of the studied VSCL laminates in this section is the same as the DCB test which was shown in figure 4.9. The fibre angle parameter T_1 is varied from 0° to 60° . The plate is discretised with element size equal to value 1 mm and the load-deflection diagram for the interface of the VSCL plates where the maximum response is achieved, is depicted in figure 7.2.

A significant reduction in the maximum structural load supported by the VSCL plates is achieved by inducing the curvilinear fibre angle at the edge of the laminates T_1 . The maximum load is carried by the plate with [$\langle 10^\circ|0^\circ \rangle$, $\langle 10^\circ|0^\circ \rangle$] lay-up. Furthermore, additional delamination growth is predicted at the structural load level for VSCL plates with moderately curved fibres when compared to too much curved ones. In other words, a sort of brittle characteristics for VSCL plates with distorted fibres is observed. As much as the delamination propagates toward the middle of the laminate - where T_0 mostly affects the fibre curvature which is constant in this particular example - similar responses in the load-displacement diagrams is achieved. This fact can be attributed to the ability of the curvilinear fibres in locally redistributing the loads. Thus, it is concluded that for this particular case study the parameter T_1 in VSCL has the most significant role on delamination initiation and propagation of them.

Although the plate was subjected to equally balanced loads in the previous study, the delamination was initiated at one corner of the plate for all the simulated samples except the plate with $[0^\circ]_2$ lay-up. The deformed shape of the delaminated VSCL plate at the last loading step which is reported in figure 7.2, is depicted in figure 7.3.

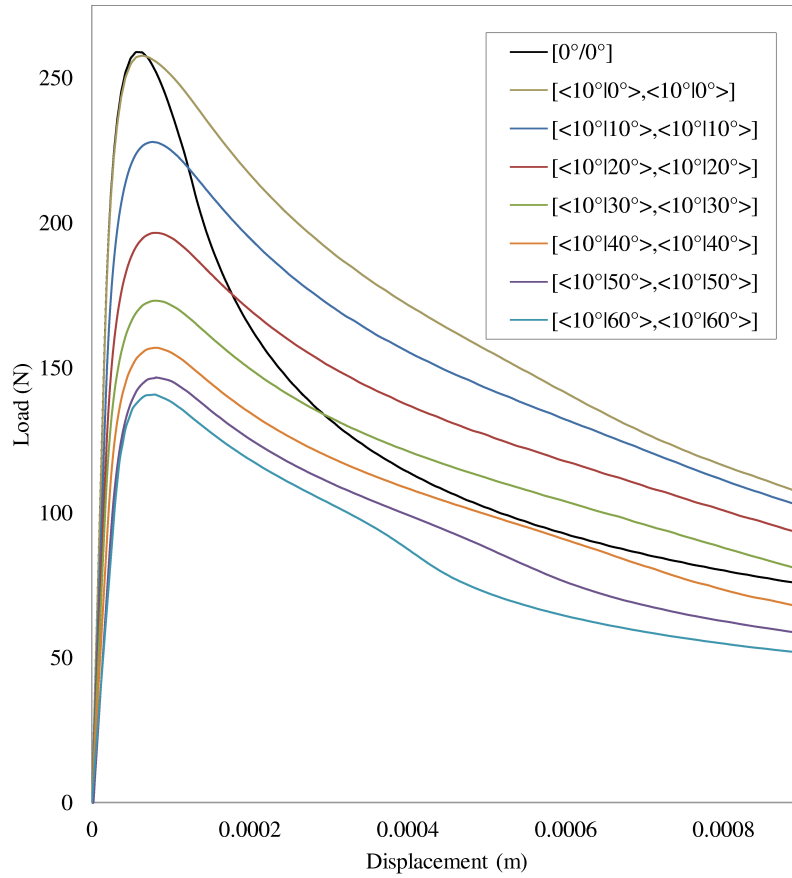


Figure 7.2: Load-displacement diagram of VSCL laminate $[\langle 10^\circ|T_1 \rangle, \langle 10^\circ|T_1 \rangle]$ subjected to transverse edge-loads.

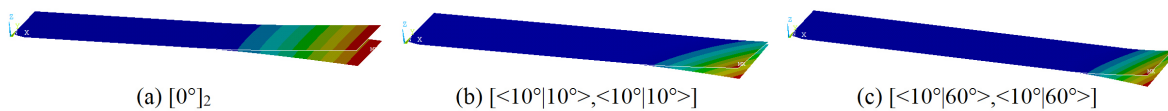


Figure 7.3: Deformed shape of plates $[\langle 10^\circ|T_1 \rangle, \langle 10^\circ|T_1 \rangle]$ under transverse edge loadings.

In the next study, the effect of the second curvilinear fibre angle parameter T_0 on the delamination onset and growth of VSCL plates is investigated. Therefore, the previous analysis for Mode I loading condition is performed by varying T_0 from 0° to 60° while keeping T_1 as constant value 10° . The load against the maximum displacement achieved at the interface of VSCL plates is depicted in figure 7.4.

Composing VSCL plates with too much curved fibres leads to a gradual reduction in the maximum load carried by the structure; also, less debonding is achieved at the interface zone. By comparing figure 7.2 with figure 7.4, one can conclude that the responses of the VSCL plates in which the fibre angle parameter T_0 is altered are slightly sensitive than the case where T_1 is varied. The deformed shape of the delaminated VSCL plate in the current study and at the last loading step which is

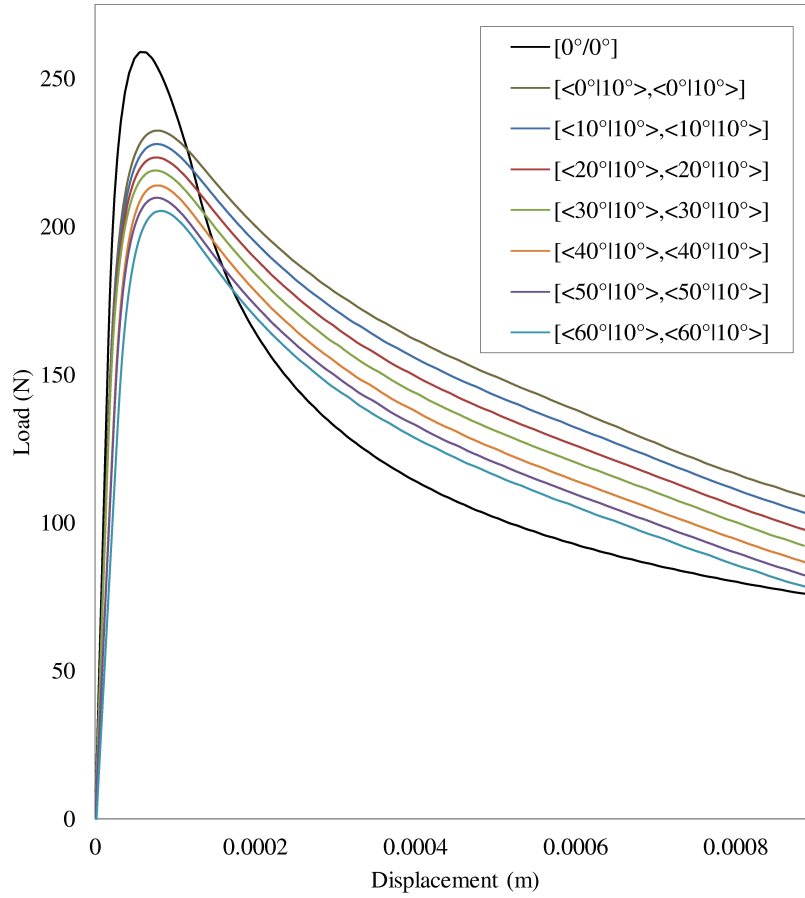


Figure 7.4: Load-displacement diagram for VSCL plate $[\langle T_0|10^\circ \rangle, \langle T_0|10^\circ \rangle]$ subjected to transverse edge loadings.

reported in figure 7.4, is depicted in figure 7.5.

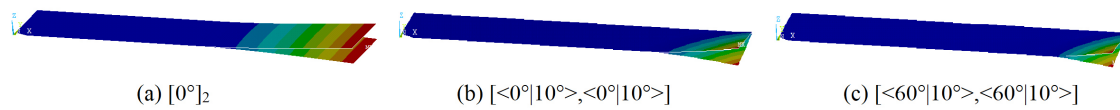


Figure 7.5: Deformed shape of the VSCL plates $[\langle T_0|10^\circ \rangle, \langle T_0|10^\circ \rangle]$ under transverse edge loadings.

The delamination is initiated at the same corner in this study as the previous one. It is noticed that the location of delamination onset is changed to the opposite corner when the negative fibre orientation for the parameter T_1 is considered.

7.3 Closing remarks

In this chapter, the composite laminates of variable stiffness were analysed. The response of the VSCL plates is less affected by the fibre angle at centre while they are

subjected to loading at the edges. This is an important conclusion that the fracture process of the delamination analysis is influenced by the neighbouring area. In other words, the fibre orientation has a significant influence of the structural behaviour of composite laminates when the delamination propagation is incorporated. In the next chapter, the delamination initiation and propagation is investigated in an intact shell structure.

Chapter 8

Final example

This final example deals with the delamination analysis of composite shells. Thus, all the developed theories in the previous chapters - that were already verified independently - are applied in this general example. In addition, the solution procedure that was introduced in section 5.5 will be used. Thus, unlike the examples of previous chapters, the location of delamination onset is unknown and will be identified within the analysis.

An intact pinched cylindrical shell of radius $R=0.06$ m with length $L=0.03$ m and total thickness $h=0.004$ m is analysed. The shell is loaded by two point forces F with same magnitude but opposite directions. A schematic view of the pinched cylindrical shell is shown in figure 8.1.

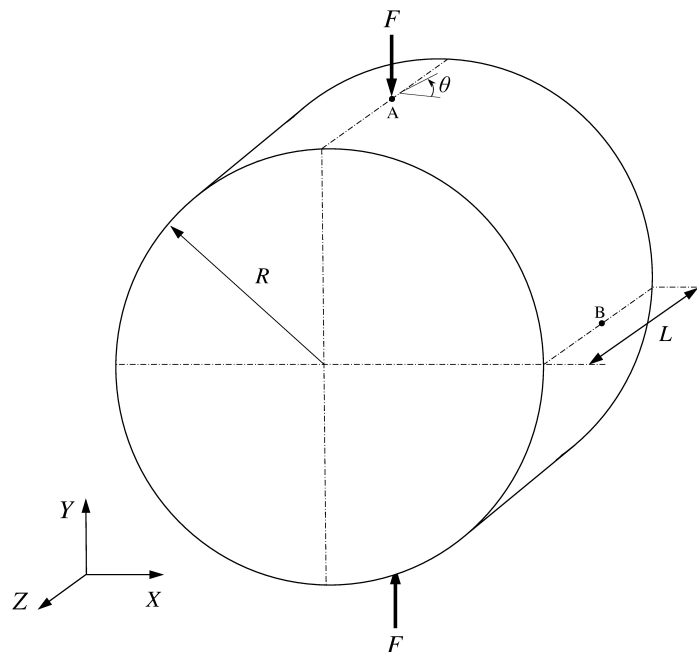


Figure 8.1: Schematic view of pinched cylindrical shell.

The shell is composed of six plies $[\theta_1/\theta_2/\theta_3]_s$ with equal thicknesses. The material properties of an AS/3501 graphite epoxy composite are assumed. They are taken from

Wagner et al. (2001) where the orthotropic material properties of composite are defined by $E_{11}=135$ GPa, $E_{22}=8.5$ GPa, $\nu_{12}=0.317$, $G_{12}=G_{13}=G_{23}=5.15$ GPa. The interface properties are $N=51.7$ MPa, $S=91$ MPa, $G_I^{cr}=130$ N/m, and $G_{II}^{cr}=230$ N/m. Due to the symmetry, only one-eighth of the shell has been modelled. The fibre angle is defined with respect to the circumference direction of the shell. The shell is discretised by 20×200 elements. In order to avoid the singularity from the point load in the finite element mesh, a distributed load is applied within a 9×9 elements in the vicinity of the loading point, being the centre of the shell. The aim of this study is to capture possible delamination nucleation and delamination propagation during the non-linear analysis. The analysis is started by the intact shell and after each converged load step, the delamination onset criterion is evaluated in a post-processing step to find a possible nucleation of delamination. The acquired information of delamination onset will be included in the next loading steps. Thus, the XFEM, the cohesive, and the contact formulations are introduced based on the necessity of the analysis.

Three lay-ups as $[0^\circ/0^\circ/0^\circ]_s$, $[0^\circ/45^\circ/90^\circ]_s$, and $[30^\circ/0^\circ/-30^\circ]_s$ are selected to study the effect of stacking sequence on the location of delamination initiation and the general response of the shell. The results of the present theory for shell with considering damage and without this consideration are compared with the ones of standard element Shell181 of ANSYS software. The load-displacement diagram at the point A is depicted in figure 8.2.

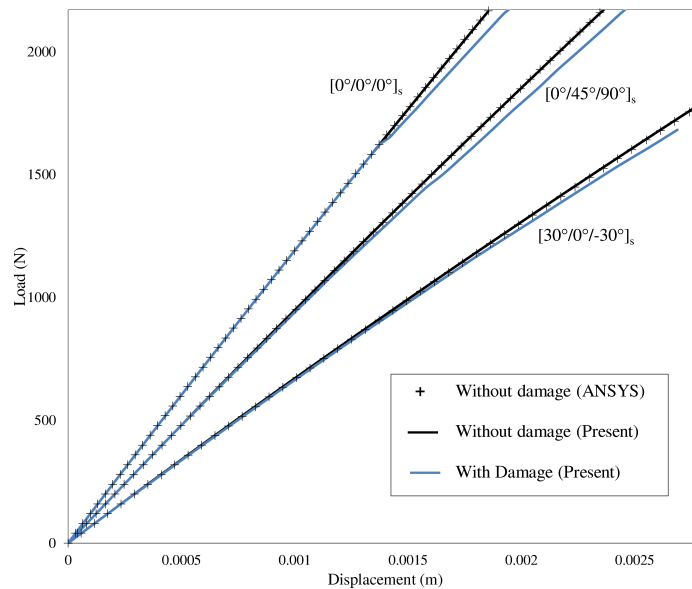


Figure 8.2: Load-displacement diagram of pinched cylindrical shell at point A.

The delamination initiation criterion is satisfied at the higher load amplitude for the shell with lay-up $[0^\circ/0^\circ/0^\circ]_s$ while the delamination is nucleated earlier for the ones with tilted fibres. This fact can be attributed to the different in-plane properties at each particular ply level of the latter cases that consequently lead to the growing interlaminar stresses. In all the studied problems, the delamination is initiated mainly at the third and the fifth interface. The deformed shape of the shells at the last loading

step is depicted in figure 8.3. In order to better clarify the results, the locations of delamination have been zoomed out.

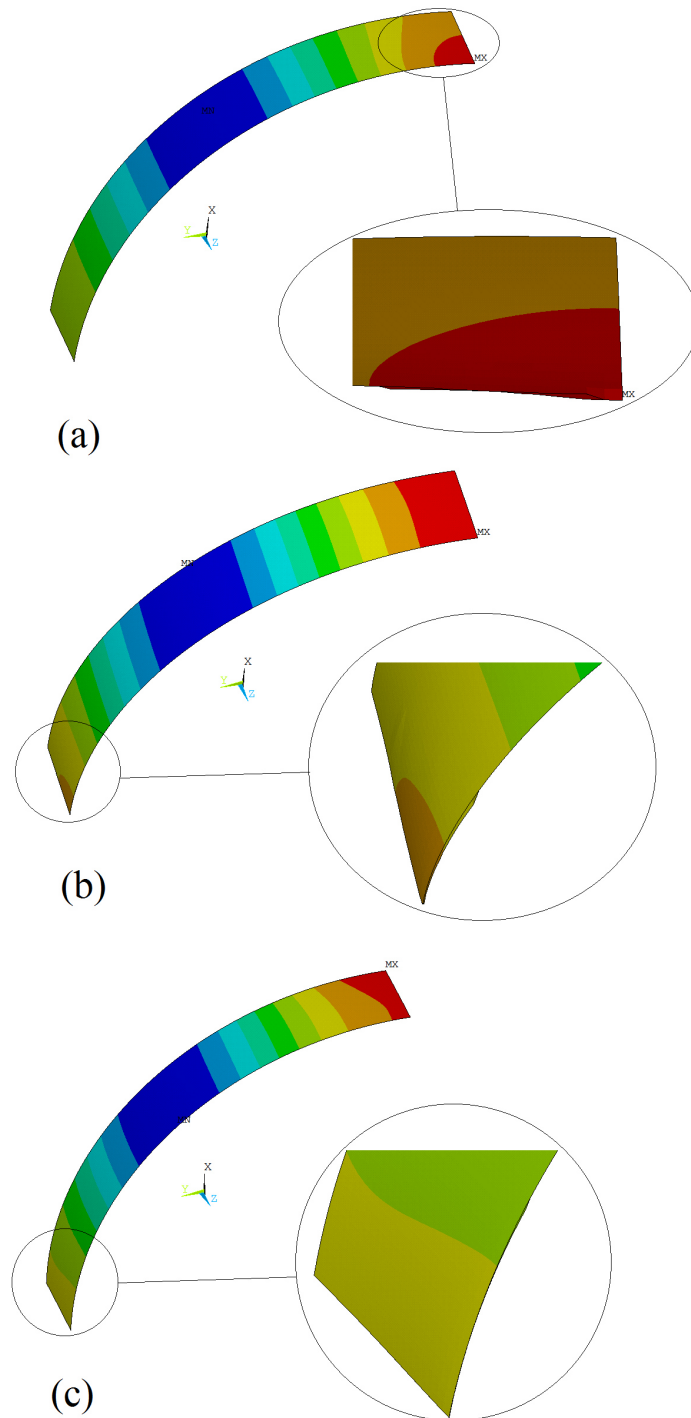


Figure 8.3: Deformed shape of shells at the last loading steps: (a) $[0^\circ/0^\circ/0^\circ]_s$; (b) $[0^\circ/45^\circ/90^\circ]_s$; and (c) $[30^\circ/0^\circ/-30^\circ]_s$.

As it is observed, in the shell with $[0^\circ/0^\circ/0^\circ]_s$ lay-up delamination initiates at the

location where the load has been applied. However, in the other two cases delamination nucleates at point B, see figure 8.1. This study clarifies the influence of fibre angle on the location of delamination initiation.

The new algorithm that was introduced in section 5.5 has been successfully applied in this problem to predict the location of delamination onset. Furthermore, the possibility to track the delamination propagation is provided, locally, through the application of cohesive zone model. The computational cost is reduced and the pre-defined algorithm can automatically follow the delamination failure at the potential interfaces.

Chapter 9

Conclusions and future work

A theoretical and numerical tool is established to simulate the response of multi-layered composite shells in the linear and geometrically non-linear regime. The formulation is capable to investigate the delamination type failure in intact shells by detecting the delamination onset and predicting the growth under increasing load. It is based on the flat-shell formulation and the equivalent single layer theory that has been enriched by XFEM to include arbitrary discontinuities, through the thickness of composite shells. Therefore, the behaviour of delaminated interface is predicted using the regular and enhanced DOFs. Hence, the standard simulation that contains modelling of subdomains and aligning the mesh schemes of the discontinuous subdomains is eliminated. In addition, the present formulation can be applied to simulate the shell that is partially delaminated without modelling the discontinuity and applying constraints in the remaining area.

The availability of enhanced DOFs in XFEM facilitates the implementation of any interface formulation. In this thesis two particular cohesive zone models are developed in order to track the delamination initiation and propagation in particular areas. Furthermore, a simple contact formulation is embedded to avoid the inward penetration of subdomains. All the aforementioned theories are implemented in the context of the XFEM theory. An important aspect of the present formulation concerns the application of the XFEM and the cohesive zone model, locally, within the domain of the finite element mesh. Since several tangent operators are developed in the framework of the same element, this numerical toolkit is flexible for predicting the response of intact or delaminated shells in linear or geometrically non-linear regime. The decision to switch between the formulations is being made through a damage model. The damage model contains a quadratic delamination onset criterion in that the interlaminar stresses are employed. Since most of laminate theories are developed in two-dimensional state (similar to the present formulation), the interlaminar stresses are not determined precisely. In this thesis, at first, the interface formulation is applied to retrieve the interlaminar stresses. This method is very precise but it is numerically expensive and it requires several simulations of the same problem to obtain interlaminar stress distributions through the thickness of the laminate. Second, the equilibrium equation of elasticity is utilized to retrieve these stresses in post-processing in only one attempt. This approach can predict the interlaminar shear stresses more accurate than the transverse normal stress.

However, the predicted outcomes can be exploited into the damage model to clarify the critical locations. Through the damage model and an innovative algorithm introduced, the analysis can be executed by an intact shell rather than a completely discontinuous one in which the cohesive formulation is included at all subdomains. In other words, the XFEM and cohesive formulations are inserted in the potential locations exclusively. The aforementioned calculations are accomplished after each loading step to assign the consequent analysis. By aiding the post-processing analysis described, the enhanced DOFs are activated spontaneously within the non-linear analysis and the delamination front is formed without remeshing process. The proposed algorithm leads to the reduction of numerical cost and simulation effort during the delamination analysis.

Apart from the theory developed, in this thesis several improvements are referred to the instability of cohesive zone model. For instance, the integration scheme of the cohesive tangent operator is changed where a superior performance is obtained for the Lobatto quadrature rule. The most oscillatory results are obtained by the Newton-Cotes 2×2 integration. In addition, the length of the softening zone is elongated by using an exponential damage evolution law. This helps to maintain the softening behaviour at the delamination front whilst the fracture process is conveyed to the remaining non-cracked elements. The accuracy of the exponential softening behaviour in prediction of delamination growth is proven. Moreover, the arc-length method is utilized to precisely follow any complexity that might be encountered in the solution path.

In order to examine the accuracy and the precision of the present formulations, several verification studies are investigated for each part. The results correlate very well with the experimental and numerical ones in literature. It is concluded that the geometrical non-linearity has less contribution to the DCB standard fracture test and the non-linear response associates to the fracture process exclusively. Although the nodal points are not defined at the plane of discontinuity, a new algorithm is suggested, using the enhanced DOFs, to apply a force type imperfection in the non-linear delamination buckling analysis.

This thesis also deals with the influence of composite material and the fibre orientations on the delamination phenomenon. Two sorts of fibre orientation are studied: the laminates in those fibres are straight and the laminates with curved fibres. The former is referred to Constant Stiffness Composite Laminate (CSCL) while the latter is called Variable Stiffness Composite Laminate (VSCL). In general, the initiation of delamination attributes to the local stiffness of the structures where interlaminar stresses grow, abruptly. For example, in the pure Mode I loading condition in both the CSCL and VSCL plates, the location of the delamination onset strongly depends on the fibre orientation at the edge of the laminate. However, the maximum load carrying capacity corresponds to the composite plates with moderate fibre orientations. In VSCL, the simulation of composite plates with sharp curved fibres led to a drop in the maximum load carried by the structure, and consequently, less displacement jump is obtained in the vicinity of the delaminated interface. This fact is highlighted when the curvature is increased by the fibre angle parameter T_1 that associates to the fibre angle at the edges. The influence of fibre angle and lay-up on the location of delamination onset

in composite cylindrical shells is more prominent. In composite shells with 0° fibre angle, the high interlaminar stress gradient is reported in the vicinity of loading point. However, when fibres are tilted, these stresses may grow elsewhere. It is more likely to have delamination starting at various interfaces of shell but at different locations.

As a basis, the simulation of delamination failure is very complex and a comprehensive study should comprise different scales. Here, a macroscale formulation is developed and the attention is drawn to the behaviour of intact shell or with interfacial debonding. Though, the delamination can be referred to the matrix-fibre debonding as well. Furthermore, the matrix cracking itself plays a critical role on increasing the interlaminar stresses that consequently results in the delamination failure. The aforementioned deficiencies can be improved. The lack of the simulation of multiple delaminations is the greatest limitation with the present formulation that can be improved. In addition, modelling of delamination coalescence is not provided when planar cracks present at different interfaces. Thus, the crack front is artificially formed once the approach of delamination fronts at dissimilar interfaces is detected. Apart from the numerical solutions that are suggested to enhance the cohesive formulation, more stable fracture methodologies can be incorporated to simulate the crack growth. The numerical problems of fracture analysis are still a challenge in the computational mechanics. Even the innovative theories like the XFEM, the thick level set, or the phase-field demonstrate some deficiencies (Cazes and Moës, 2015). The developed flat-shell formulation is based on the assumption of laminate theories. Therefore, the developed formulation is applicable to small strain and moderate rotations that is sufficient for composite materials in practice. However, the large rotations can be followed either by using the corotational approach (see (Crisfield, 1991; Rust, 2015) for more details) or modifying the present formulation by the updated Lagrangian approach (see (Fafard et al., 1989; Mohan, 1997) for more details).

Bibliography

- Abaqus Documentation. Version 6.8. *Simulia Corporation*, 2008.
- M. M. Abdalla, S. Setoodeh, and Z. Gürdal. Design of variable stiffness composite panels for maximum fundamental frequency using lamination parameters. *Composite Structures*, 81:283–291, 2007.
- H. Akhavan, P. Ribeiro, and M. F. de Moura. Large deflection and stresses in variable stiffness composite laminates with curvilinear fibres. *International Journal of Mechanical Sciences*, 73:14–26, 2013.
- G. Alfano and M. A. Crisfield. Finite element interface models for the delamination analysis of laminated composites: mechanical and computational issues. *International Journal for Numerical Methods in Engineering*, 50:1701–1736, 2001.
- O. Allix and A. Corigliano. Geometrical and interfacial non-linearities in the analysis of delamination in composites. *International Journal of Solids and Structures*, 36: 2189–2216, 1999.
- D. J. Allman. A compatible triangular element including vertex rotations for plane elasticity analysis. *Computers and Structures*, 19:1–8, 1984.
- ANSYS Documentation. Version 14.5. *ANSYS Inc*, 2013.
- P. Areias and T. Belytschko. Non-linear analysis of shells with arbitrary evolving cracks using xfem. *International Journal for Numerical Methods in Engineering*, 62: 384–415, 2005.
- C. Balzani and W. Wagner. An interface element for the simulation of delamination in unidirectional fiber-reinforced composite laminates. *Engineering Fracture Mechanics*, 75:2597–2615, 2008.
- C. Balzani and W. Wagner. Numerical treatment of damage propagation in axially compressed composite airframe panels. *International Journal of Structural Stability and Dynamics*, 10:683–703, 2010.
- E. J. Barbero. *Finite Element Analysis of Composite Materials using Abaqus*. CRC Press, 2013.

- E. Barbieri and M. Meo. A meshfree penalty-based approach to delamination in composites. *Composites Science and Technology*, 69:2169–2177, 2009.
- G. I. Barenblatt. The formation of equilibrium cracks during brittle fracture. general ideas and hypotheses. axially-symmetric cracks. *Journal of Applied Mathematics and Mechanics*, 23:622–636, 1959.
- T. Belytschko and T. Black. Elastic crack growth in finite elements with minimal remeshing. *International Journal for Numerical Methods in Engineering*, 45:601–620, 1999.
- V. Birman and C. W. Bert. On the choice of shear correction factor in sandwich structures. *Journal of Sandwich Structures and Materials*, 4:83–95, 2002.
- C. Bisagni. Numerical analysis and experimental correlation of composite shell buckling and post-buckling. *Composites Part B: Engineering*, 31:655–667, 2000.
- C. Bisagni. Progressive delamination analysis of stiffened composite panels in post-buckling. In *Proceedings of the AIAA/ASME/ASCE/AHS/ASC 47th Structures, Structural Dynamics & Materials Conference, AIAA paper*, number 2006-2178, 2006.
- V. V. Bolotin. Delaminations in composite structures: its origin, buckling, growth and stability. *Composites Part B: Engineering*, 27:129–145, 1996.
- J. C. Brewer and P. A. Lagace. Quadratic stress criterion for initiation of delamination. *Journal of Composite Materials*, 22:1141–1155, 1988.
- J. Brouzoulis and M. Fagerström. An enriched shell element formulation for efficient modeling of multiple delamination propagation in laminates. *Composite Structures*, 126:196–206, 2015.
- D. Bushnell. Buckling of shells-pitfall for designers. *AIAA Journal*, 19:1183–1226, 1981.
- P. P. Camanho and C. G. Dávila. Mixed-mode decohesion finite elements for the simulation of delamination in composite materials. *NASA-Technical paper*, 211737: 33, 2002.
- R. D. S. G. Campilho, M. F. de Moura, and J. J. M. S. Domingues. Using a cohesive damage model to predict the tensile behaviour of cfrp single-strap repairs. *International Journal of Solids and Structures*, 45:1497–1512, 2008.
- F. Cazes and N. Moës. Comparison of a phase-field model and of a thick level set model for brittle and quasi-brittle fracture. *International Journal for Numerical Methods in Engineering*, 103:114–143, 2015.
- H. Chai, C. D. Babcock, and W. G. Knauss. One dimensional modelling of failure in laminated plates by delamination buckling. *International Journal of Solids and Structures*, 17:1069–1083, 1981.

- R. D. Cook. Four-node flat shell element: drilling degrees of freedom, membrane-bending coupling, warped geometry, and behavior. *Computers and Structures*, 50: 549–555, 1994.
- M. A. Crisfield. Non linear finite element analysis of solids and structures, vol. 1, 1991.
- T. D. Dang and S. R. Hallett. A numerical study on impact and compression after impact behaviour of variable angle tow laminates. *Composite Structures*, 96:194–206, 2013.
- T. D. Dang, S. R. Hallett, B. C. Kim, Y. L. Cahain, R. Butler, and W. Liu. Modelling of as manufactured geometry for prediction of impact and compression after impact behaviour of variable angle tow laminates. *Journal of Composite Materials*, pages 1423–1438, 2014.
- C. G. Dávila, P. P. Camanho, and A. Turon. Cohesive elements for shells. *NASA TP Technical Reports*, 214869, 2007.
- C. G. Dávila, P. P. Camanho, and A. Turon. Effective simulation of delamination in aeronautical structures using shells and cohesive elements. *Journal of Aircraft*, 45: 663–672, 2008.
- R. de Borst, M. A. Gutiérrez, G. N. Wells, J. J. C. Remmers, and H. Askes. Cohesive-zone models, higher-order continuum theories and reliability methods for computational failure analysis. *International Journal for Numerical Methods in Engineering*, 60:289–315, 2004.
- M. Di Sciuva and E. Carrera. Static buckling of moderately thick, anisotropic, laminated and sandwich cylindrical shell panels. *AIAA Journal*, 28:1782–1793, 1990.
- J. Diaz, C. Fagiano, M. M. Abdalla, Z. Gürdal, and S. Hernandez. A study of interlaminar stresses in variable stiffness plates. *Composite Structures*, 94:1192–1199, 2012.
- J. Dolbow and T. Belytschko. A finite element method for crack growth without remeshing. *International Journal for Numerical Methods in Engineering*, 46:131–150, 1999.
- I. Elishakoff, S. van Manen, and J. Arbocz. First-order second-moment analysis of the buckling of shells with random imperfections. *AIAA Journal*, 25:1113–1117, 1987.
- A. M. Elmarakbi, N. Hu, and H. Fukunaga. Finite element simulation of delamination growth in composite materials using LS-DYNA. *Composites Science and Technology*, 69:2383–2391, 2009.
- M. Fafard, G. Dhatt, and J. L. Batoz. A new discrete kirchhoff plate/shell element with updated procedures. *Computers and Structures*, 31:591–606, 1989.

- C. Fagiano, M. M. Abdalla, C. Kassapoglou, and Z. Gürdal. Interlaminar stress recovery for three-dimensional finite elements. *Composites Science and Technology*, 70: 530–538, 2010.
- M. T. Fenske and A. J. Vizzini. The inclusion of in-plane stresses in delamination criteria. *Journal of Composite Materials*, 35:1325–1342, 2001.
- A. J. M. Ferreira. A formulation of the multiquadric radial basis function method for the analysis of laminated composite plates. *Composite Structures*, 59:385–392, 2003.
- A. C. Garg. Delamination - a damage mode in composite structures. *Engineering Fracture Mechanics*, 29:557–584, 1988.
- D. Gay, S. V. Hoa, and S. W. Tsai. *Composite Materials: Design and Applications*. CRC Press, 2002.
- V. K. Goyal, N. R. Jaunky, E. R. Johnson, and D. R. Ambur. Intralaminar and interlaminar progressive failure analyses of composite panels with circular cutouts. *Composite Structures*, 64:91–105, 2004.
- R. M. J. Groh, P. M. Weaver, and A. Tessler. Application of the refined zigzag theory to the modeling of delaminations in laminated composites. *NASA TP Technical Reports*, 218808, 2015.
- F. Gruttmann and W. Wagner. Delamination analysis of thin composite structures using a multi-director formulation. *Advances in Analysis and Design. Civil-Comp. Press, Edinburgh*, pages 51–59, 1996.
- L. N. B. Gummadi and A. N. Palazotto. Progressive failure analysis of composite cylindrical shells considering large rotations. *Composites Part B: Engineering*, 29: 547–563, 1998.
- Z. Gürdal, B. F. Tatting, and C. K. Wu. Variable stiffness composite panels: effects of stiffness variation on the in-plane and buckling response. *Composites Part A: Applied Science and Manufacturing*, 39:911–922, 2008.
- P. A. Gustafson and A. M. Waas. Efficient and robust traction laws for the modeling of adhesively bonded joints. In *Proceedings of the AIAA/ASME/ASCE/AHS/ASC 49th structures, structural dynamics, and materials conference*, pages 2008–1847, 2008.
- L. Hamitouche, M. Tarfaoui, and A. Vautrin. An interface debonding law subject to viscous regularization for avoiding instability: application to the delamination problems. *Engineering Fracture Mechanics*, 75:3084–3100, 2008.
- T. B. Hartman, M. W. Hyer, and S. W. Case. Stress recovery in composite laminates. In *52nd AIAA/ASME/ASCE/AHS/ASC Structures, Structural Dynamics and Materials Conference 19th AIAA/ASME/AHS Adaptive Structures Conference 13t*, pages 1856–1880, 2011.

- C. T. Herakovich. Mechanics of composites: a historical review. *Mechanics Research Communications*, 41:1–20, 2012.
- M. W. Hilburger and J. H. Starnes. Effects of imperfections on the buckling response of compression-loaded composite shells. *International Journal of Non-Linear Mechanics*, 37:623–643, 2002.
- S. Honda and Y. Narita. Natural frequencies and vibration modes of laminated composite plates reinforced with arbitrary curvilinear fiber shape paths. *Journal of Sound and Vibration*, 331:180–191, 2012.
- N. Hu, Y. Zemba, H. Fukunaga, H. H. Wang, and A. M. Elmarakbi. Stable numerical simulations of propagations of complex damages in composite structures under transverse loads. *Composites Science and Technology*, 67:752–765, 2007.
- N. Hu, Y. Zemba, T. Okabe, C. Yan, H. Fukunaga, and A. M. Elmarakbi. A new cohesive model for simulating delamination propagation in composite laminates under transverse loads. *Mechanics of Materials*, 40:920–935, 2008.
- T. J. R. Hughes and F. Brezzi. On drilling degrees of freedom. *Computer Methods in Applied Mechanics and Engineering*, 72:105–121, 1989.
- A. Ibrahimbegovic, R. L. Taylor, and E. L. Wilson. A robust quadrilateral membrane finite element with drilling degrees of freedom. *International Journal for Numerical Methods in Engineering*, 30:445–457, 1990.
- R. M. Jones. *Mechanics of composite materials*. CRC Press, 1998.
- G. Kuhlmann and R. Rolfes. A hierarchic 3d finite element for laminated composites. *International Journal for Numerical Methods in Engineering*, 61:96–116, 2004.
- I. Lapczyk and J. A. Hurtado. Progressive damage modeling in fiber-reinforced materials. *Composites Part A: Applied Science and Manufacturing*, 38:2333–2341, 2007.
- C. S. Lopes, Z. Gürdal, and P. P. Camanho. Variable-stiffness composite panels: Buckling and first-ply failure improvements over straight-fibre laminates. *Computers and Structures*, 86:897–907, 2008.
- P. Mohan. Development and applications of a flat triangular element for thin laminated shells. 1997.
- C. M. D. Moorthy and J. N. Reddy. Recovery of interlaminar stresses and strain energy release rates in composite laminates. *Finite Elements in Analysis and Design*, 33:1–27, 1999.
- T. Nagashima and H. Suemasu. X-fem analyses of a thin-walled composite shell structure with a delamination. *Computers and Structures*, 88:549–557, 2010.

- K. F. Nilsson, L. E. Asp, J. E. Alpman, and L. Nystedt. Delamination buckling and growth for delaminations at different depths in a slender composite panel. *International Journal of Solids and Structures*, 38:3039–3071, 2001.
- E. Oñate. *Structural Analysis with the Finite Element Method. Linear Statics: Vol. 2: Beams, Plates and Shells*, volume 3. Springer Science and Business Media, 2013.
- E. Oñate, O. C. Zienkiewicz, B. Suarez, and R. L. Taylor. A general methodology for deriving shear constrained reissner-mindlin plate elements. *International Journal for Numerical Methods in Engineering*, 33:345–367, 1992.
- M. Ortiz and A. Pandolfi. Finite-deformation irreversible cohesive elements for three-dimensional crack-propagation analysis. *International Journal for Numerical Methods in Engineering*, 44:1267–1282, 1999.
- Y. Qiu, M. A. Crisfield, and G. Alfano. An interface element formulation for the simulation of delamination with buckling. *Engineering Fracture Mechanics*, 68:1755–1776, 2001.
- J. N. Reddy. *Mechanics of laminated composite plates and shells: theory and analysis*. CRC Press, 2004.
- J. N. Reddy. *An Introduction to Nonlinear Finite Element Analysis: with applications to heat transfer, fluid mechanics, and solid mechanics*. OUP Oxford, 2014.
- J. N. Reddy and A. K. Pandey. A first-ply failure analysis of composite laminates. *Computers and Structures*, 25:371–393, 1987.
- Y. S. N. Reddy, C. M. D. Moorthy, and J. N. Reddy. Non-linear progressive failure analysis of laminated composite plates. *International Journal of Non-linear Mechanics*, 30:629–649, 1995.
- E. D. Reedy, F. J. Mello, and T. R. Guess. Modeling the initiation and growth of delaminations in composite structures. *Journal of Composite Materials*, 31:812–831, 1997.
- J. Remmers and R. de Borst. Application of the discontinuous solid-like shell element to delamination. In *45th AIAA/ASME Structures, Structural Dynamics and Materials Conference, Palm Spring, California*, 2004.
- J. J. C. Remmers, G. N. Wells, and R. de Borst. A solid-like shell element allowing for arbitrary delaminations. *International Journal for Numerical Methods in Engineering*, 58:2013–2040, 2003.
- P. Ribeiro, H. Akhavan, A. Teter, and J. Warmiński. A review on the mechanical behaviour of curvilinear fibre composite laminated panels. *Journal of Composite Materials*, 48:2761–2777, 2014.

- D. H. Robbins and J. N. Reddy. Modelling of thick composites using a layerwise laminate theory. *International Journal for Numerical Methods in Engineering*, 36: 655–677, 1993.
- W. Rust. *Non-linear Finite Element Analysis in Structural Mechanics*. Springer, 2015.
- J. C. J. Schellekens and R. de Borst. On the numerical integration of interface elements. *International Journal for Numerical Methods in Engineering*, 36:43–66, 1992.
- M. Schürg, W. Wagner, and F. Gruttmann. An enhanced fsdt model for the calculation of interlaminar shear stresses in composite plate structures. *Computational Mechanics*, 44:765–776, 2009.
- S. Setoodeh, M. M. Abdalla, S. T. IJsselmuiden, and Z. Gürdal. Design of variable-stiffness composite panels for maximum buckling load. *Composite Structures*, 87: 109–117, 2009.
- G. J. Short, F. J. Guild, and M. J. Pavier. The effect of delamination geometry on the compressive failure of composite laminates. *Composites Science and Technology*, 61: 2075–2086, 2001.
- J. C. Simo. A framework for finite strain elastoplasticity based on maximum plastic dissipation and the multiplicative decomposition. part ii: computational aspects. *Computer Methods in Applied Mechanics and Engineering*, 68:1–31, 1988.
- J. L. C. Sosa and N. Karapurath. Delamination modelling of glare using the extended finite element method. *Composites Science and Technology*, 72:788–791, 2012.
- S. Sridharan. *Delamination behaviour of composites*. Elsevier, 2008.
- N. Sukumar, D. L. Chopp, N. Moës, and T. Belytschko. Modeling holes and inclusions by level sets in the extended finite-element method. *Computer Methods in Applied Mechanics and Engineering*, 190:6183–6200, 2001.
- P. Sundaresan, G. Singh, and G. V. Rao. Buckling and post-buckling analysis of moderately thick laminated rectangular plates. *Computers and Structures*, 61:79–86, 1996.
- K. Y. Sze, X. H. Liu, and S. H. Lo. Popular benchmark problems for geometric nonlinear analysis of shells. *Finite Elements in Analysis and Design*, 40:1551–1569, 2004.
- B. F. Tatting, Z. Gürdal, and D. Jegley. Design and manufacture of elastically tailored tow placed plates. *NASA Technical paper*, 211919:34, 2002.
- R. L. Taylor. Finite element analysis of linear shell problems. In *Whiteman, JR (ed.), Proceedings of the Mathematics in Finite Elements and Applications*, pages 191–203, 1987.

- A. Turon, C. G. Davila, P. P. Camanho, and J. Costa. An engineering solution for mesh size effects in the simulation of delamination using cohesive zone models. *Engineering Fracture Mechanics*, 74:1665–1682, 2007.
- G. J. Turvey and M. Y. Osman. Dr large deflection analysis of orthotropic mindlin plates with simply-supported and clamped-edge conditions. *Composites Engineering*, 1:235–248, 1991.
- F. P. Van der Meer, N. Moës, and L. J. Sluys. A level set model for delamination–modeling crack growth without cohesive zone or stress singularity. *Engineering Fracture Mechanics*, 79:191–212, 2012.
- W. Wagner, F. Gruttmann, and W. Sprenger. A finite element formulation for the simulation of propagating delaminations in layered composite structures. *International Journal for Numerical Methods in Engineering*, 51:1337–1359, 2001.
- K. Wisniewski. Finite rotation shells. *Basic equations and finite elements for Reissner kinematics*. CIMNE-Springer, 2010.
- J. C. Wohlever. Some computational aspects of a group theoretic finite element approach to the buckling and postbuckling analyses of plates and shells-of-revolution. *Computer Methods in Applied Mechanics and Engineering*, 170:373–406, 1999.
- P. Wriggers. *Nonlinear finite element methods*. Springer Science and Business Media, 2008.
- P. Wriggers, W. Wagner, and C. Miehe. A quadratically convergent procedure for the calculation of stability points in finite element analysis. *Computer Methods in Applied Mechanics and Engineering*, 70:329–347, 1988.
- X. P. Xu and A. Needleman. Numerical simulations of fast crack growth in brittle solids. *Journal of the Mechanics and Physics of Solids*, 42:1397–1434, 1994.
- S. Yazdani and P. Ribeiro. Geometrically non-linear static analysis of unsymmetric composite plates with curvilinear fibres: p-version layerwise approach. *Composite Structures*, 118:74–85, 2014.
- S. Yazdani and P. Ribeiro. A layerwise p-version finite element formulation for free vibration analysis of thick composite laminates with curvilinear fibres. *Composite Structures*, 120:531–542, 2015.
- S. Yazdani, P. Ribeiro, and J. D. Rodrigues. A p-version layerwise model for large deflection of composite plates with curvilinear fibres. *Composite Structures*, 108:181–190, 2014.
- S. Yazdani, W. J. H. Rust, and P. Wriggers. Delamination growth in composite laminates of variable stiffness. *International Journal for Numerical Methods in Engineering*, 108:1406–1424, 2016a.

- S. Yazdani, W. J. H. Rust, and P. Wriggers. An xfem approach for modelling delamination in composite laminates. *Composite Structures*, 135:353–364, 2016b.
- O. C. Zienkiewicz and R. L. Taylor. *The finite element method: Solid mechanics*, volume 2. Butterworth-heinemann, 2000.
- O. C. Zienkiewicz and J. Z. Zhu. A simple error estimator and adaptive procedure for practical engineering analysis. *International Journal for Numerical Methods in Engineering*, 24:337–357, 1987.
- D. Zwillinger. *CRC standard mathematical tables and formulae*. CRC Press, 2012.

Curriculum Vitae

Saleh Yazdani

born March 21, 1987 in Bojnord, Iran

Professional Experience

06.2013 - 11.2016 Research assistant at the Institute of Continuum Mechanics,
Leibniz Universität Hannover, Hannover, Germany

06.2012 - 05.2013 Research assistant at Institute of Mechanical Engineering (IDMEC),
Universidade do Porto, Porto, Portugal

Education

2009 - 2011 Tarbiat Modares University, Tehran, Iran
Mechanical Engineering
Focus: Applied Design
Degree: M. Sc.

2005 - 2009 University of Sistan and Baluchestan, Zahedan, Iran
Mechanical Engineering
Focus: Solid Mechanics
Degree: B. Sc.

2001 - 2005 Iran National Organization for Development of Exceptional Talents,
Bojnord, Iran
Diploma Majoring Mathematics and Physics

